Springer Proceedings in Physics 242

Ri-Ichi Murakami · Pankaj M. Koinkar · Tomoyuki Fujii · Tae-Gyu Kim · Hairus Abdullah *Editors*

NAC 2019

Proceedings of the 2nd International Conference on Nanomaterials and Advanced Composites

Springer

Springer Proceedings in Physics

Volume 242

Indexed by Scopus

The series Springer Proceedings in Physics, founded in 1984, is devoted to timely reports of state-of-the-art developments in physics and related sciences. Typically based on material presented at conferences, workshops and similar scientific meetings, volumes published in this series will constitute a comprehensive up-to-date source of reference on a field or subfield of relevance in contemporary physics. Proposals must include the following:

- name, place and date of the scientific meeting
- a link to the committees (local organization, international advisors etc.)
- scientific description of the meeting
- list of invited/plenary speakers
- an estimate of the planned proceedings book parameters (number of pages/articles, requested number of bulk copies, submission deadline).

More information about this series at http://www.springer.com/series/361

Ri-Ichi Murakami · Pankaj M. Koinkar ·
Tomoyuki Fujii · Tae-Gyu Kim ·
Hairus Abdullah
Editors

NAC 2019

Proceedings of the 2nd International Conference on Nanomaterials and Advanced Composites

Springer

Editors
Ri-Ichi Murakami
Department of Materials Science
and Engineering
National Taiwan University
of Science and Technology
Taipei, Taiwan

Tomoyuki Fujii
Department of Mechanical Engineering
Shizuoka University
Shizuoka, Japan

Hairus Abdullah
Department of Industrial Engineering
Universitas Prima Indonesia
Medan, Indonesia

Pankaj M. Koinkar
Department of Optical Science
Center for International Cooperation
University of Tokushima
Tokushima, Japan

Tae-Gyu Kim
Department of Nanomechatronics
Engineering
Pusan National University
Busan, Korea (Republic of)

ISSN 0930-8989 ISSN 1867-4941 (electronic)
Springer Proceedings in Physics
ISBN 978-981-15-2293-2 ISBN 978-981-15-2294-9 (eBook)
https://doi.org/10.1007/978-981-15-2294-9

This Springer imprint is published by the registered company Springer Nature Singapore Pte Ltd.
The registered company address is: 152 Beach Road, #21-01/04 Gateway East, Singapore 189721, Singapore

Participating Countries and Organizations

Chairman

Yee-Wen Yen, National Taiwan University of Science and Technology, R.O.C.

Co-chairmen

Yun-Hae Kim, Korea Maritime and Ocean University, Korea
Yoshinobu Shimamura, Shizuoka University, Japan
Chang-Mou Wu, National Taiwan University of Science and Technology, R.O.C.

International Organizing Committee

Kuei Chi Lee, Taiwan Textile Research Institute, R.O.C.
Pankaj M. Koinkar, University of Tokushima, Japan
Antonio Norio Nakagaito, University of Tokushima, Japan
Tae-Gyu Kim, Pusan National University, Korea
Subhash Kondawar, Nagpur University, India
Imae Toyoko, National Taiwan University of Science and Technology, R.O.C.
Kuo-Bing Cheng, Feng Chia University, R.O.C.
Jieng-Chiang Chen, Vanung University, R.O.C.
Keh-Moh Lin, Southern Taiwan University of Science and Technology, R.O.C.
Chi-Jung Chang, Feng Chia University, R.O.C.
Dong-Hau Kuo, National Taiwan University of Science and Technology, R.O.C.
Ming-Yuan Shen, National Chin Yi University of Science and Technology, R.O.C.
Jin-Wen Tang, Industrial Technology Research Institute, R.O.C.
Zainal Arifin Bin Mohd. Ishak, Universiti Sains Malaysia, Malaysia

Wahyu Caesarendra, Diponegoro University, Indonesia
Ngoc-Bich Le, Eastern International University, Vietnam
Jun-Cai Sun, Dalian Maritime University, China

Local Organizing Committee

Ri-Ichi Murakami, National Taiwan University of Science and Technology, R.O.C.
Wen-Cheng Ke, National Taiwan University of Science and Technology, R.O.C.
Hairus Abdullah, National Taiwan University of Science and Technology, R.O.C.

Participating Countries

1. Taiwan (R.O.C.)
2. Japan
3. India
4. South Korea
5. Indonesia
6. Malaysia
7. Brunei Darussalam
8. Vietnam
9. China

Preface

It is with great pleasure that we introduce this special issue of Springer Book containing 13 papers selected from about 100 papers presented at the 2nd International Conference on Nanomaterials and Advanced Composites (NAC 2019). The conference was held at National Taiwan University of Science and Technology in Taipei, Taiwan, from 9 to 11 August 2019, and the second in this series attracted a broad range of international researchers from various fields. The Conference of NAC is now in its second series of existence. It has been held on each year cycle starting in 2018—Busan (South Korea). This conference was initiated by a network of researchers and engineers from both academia and industry in the areas of new nanomaterials, nanotechnology and advanced composites. The key aim of NAC 2019 is to provide an opportunity for the delegates to meet, interact and exchange new ideas on nanomaterials and advanced composite development, performance and their applications. This conference covered a wide range of topics related to materials science and engineering. About 100 papers from 9 countries were submitted in this conference, and only a few manuscripts have been selected for publication in Springer Book. The papers selected for this issue of Springer Book are those represent innovative and leading work in the development field. Other papers from NAC 2019 are published in Modern Physics Letters B which are indexed by SCI. As guest editors, it is our hope that this issue will stimulate further discussion and additional research in nanomaterials and advanced composites so that in future, such a topical issue might include a range of empirical studies. We are grateful to all of the authors who contributed to the issue and the NAC 2019 participants and staff for their contributions.

Taipei, Taiwan — Prof. Ri-Ichi Murakami
Medan, Indonesia — Dr. Hairus Abdullah
Tokushima, Japan — Dr. Pankaj M. Koinkar
Shizuoka, Japan — Dr. Tomoyuki Fujii
Busan, Korea (Republic of) — Prof. Tae-Gyu Kim

Contents

Contributors

Shyamkant W. Anwane Department of Physics, Shri Shivaji Science College, Nagpur, India

Armila Department of Mechanical Engineering, Muhammadiyah University of West Sumatera, Padang, Indonesia

Wahyu Caesarendra Department of Mechanical Engineering, Diponegoro University, Semarang, Indonesia;
Faculty of Integrated Technologies, Universiti Brunei Darussalam, Gadong, Brunei Darussalam

Manjusha P. Dandekar Department of Physics, Rashtrasant Tukadoji Maharaj Nagpur University, Nagpur, India

D. F. Fitriyana Department of Mechanical Engineering, Semarang State University, Semarang, Indonesia

Tomoyuki Fujii Department of Mechanical Engineering, Shizuoka University, Hamamatsu, Japan

Lester C. Geonzon Department of Food Science and Technology, Tokyo University of Marine Science and Technology, Tokyo, Japan

Rajesh H. Gupta Department of Chemistry, KZS Science College, Nagpur, India

Wasudeo B. Gurnule Department of Chemistry, Kamla Nehru Mahavidyalaya, Nagpur, India

G. D. Haryadi Department of Mechanical Engineering, Diponegoro University, Semarang, Indonesia

M. A. Herawan Department of Mechanical Engineering, Diponegoro University, Semarang, Indonesia

Hitoshi Ishii Shizuoka University, Hamamatsu, Japan

R. Ismail Department of Mechanical Engineering, Diponegoro University, Semarang, Indonesia

Sangeeta G. Itankar Department of Physics, Rashtrasant Tukadoji Maharaj Nagpur University, Nagpur, India

Pankaj M. Koinkar Department of Optical Science, Tokushima University, Tokushima, Japan

Subhash B. Kondawar Department of Physics, Rashtrasant Tukadoji Maharaj Nagpur University, Nagpur, India

Zhong-Zhe Lai Department of Applied Chemistry, Chaoyang University of Technology, Taichung, Taiwan

Rani V. Mankar Department of Chemistry, Kamla Nehru Mahavidyalaya, Nagpur, India

Shingo Matsukawa Department of Food Science and Technology, Tokyo University of Marine Science and Technology, Tokyo, Japan

Prerna R. Modak Department of Physics, Rashtrapita Mahatma Gandhi Arts, Commerce and Science College, Saoli, Chandrapur, India

Pravin S. More Department of Physics, Institute of Science, Mumbai, India

Deoram V. Nandanwar Department of Physics, Mohata College of Science, Nagpur, India

Neha V. Nerkar Department of Physics, Rashtrasant Tukadoji Maharaj Nagpur University, Nagpur, India

R. Noferi Department of Mechanical Engineering, Diponegoro University, Semarang, Indonesia

Kyosuke Nomura Graduate School of Integrated Science and Technology, Shizuoka University, Hamamatsu, Japan

S. Nugroho Department of Mechanical Engineering, Diponegoro University, Semarang, Indonesia

Chaitali N. Pangul Department of Physics, Rashtrasant Tukadoji Maharaj Nagpur University, Nagpur, India

Pallavi T. Patil Department of Physics, Rashtrasant Tukadoji Maharaj Nagpur University, Nagpur, India

Jitendra N. Ramteke Department of Physics, Mohata Science College, Nagpur, India

M. Rizal Department of Mechanical Engineering, Diponegoro University, Semarang, Indonesia

Yeng-Fong Shih Department of Applied Chemistry, Chaoyang University of Technology, Taichung, Taiwan

Yoshinobu Shimamura Department of Mechanical Engineering, Shizuoka University, Hamamatsu, Japan

Hazwani Suhaimi Faculty of Integrated Technologies, Universiti Brunei Darussalam, Gadong, Brunei Darussalam

Sulardjaka Department of Mechanical Engineering, Diponegoro University, Semarang, Indonesia

A. Suprihanto Department of Mechanical Engineering, Diponegoro University, Semarang, Indonesia

Keiichiro Tohgo Department of Mechanical Engineering, Shizuoka University, Hamamatsu, Japan

Naoki Tonooka Graduate School of Integrated Science and Technology, Shizuoka University, Hamamatsu, Japan

Part I
Nanomaterials and Nanotechnology

Chapter 1
LPG Sensing Properties of Electrospun In-Situ Polymerized Polyaniline/MWCNT Composite Nanofibers

Pallavi T. Patil, Pravin S. More and Subhash B. Kondawar

Abstract In this paper, we report the fabrication of poly(methyl methacrylate) (PMMA) nanofibers by electrospinning technique and used as substrate for coating pure polyaniline (PANI) and PANI/multiwalled carbon nanotubes (MWCNT) separately during chemical oxidative polymerization. The morphology and structure of PANI and PANI/MWCNT nanofibers were investigated by SEM, UV-VIS, FTIR and XRD. SEM shows that the fibrous structure of PMMA with an average fiber diameter 272 nm. UV-Vis, FTIR and XRD analyses confirmed the formation of PANI and its interaction with MWCNT. Electrical responses of the synthesized samples towards LPG were measured at room temperature for various ppm, which fulfill all the characteristics like sensitivity, response, recovery of the sensors. Sensitivity study shows that materials under investigation are found to be highly sensitive for LPG near to room temperature. PANI/MWCNT nanofibers showed rapid and reversible resistance change upon exposure to LPG as compared to that of PANI nanofibers, which may be due to MWCNT wrapped by conducting PANI results in the formation of a charge transfer complex which increases the protonation of the polyaniline and the transition in the electrical resistance was attributed to a change in the localization length of the composite nanofibers.

1.1 Introduction

In recent years, detection of gases and diagnose their compositions has constantly gaining much more interest and turned into a prime concern for human wellbeing. Liquefied Petroleum Gas (LPG) is highly inflammable gas and common fuel used for domestics, industrial and commercial appliances. Generally, LPG composed of volatile low boiling point gases—*iso*-butane, ethane, propane, *n*-butane, butylene, *iso*-butene, *trans*-2-butene, propene, *cis*-2-butene, *iso*-pentane and *n*-pentane due to

P. T. Patil · S. B. Kondawar (✉)
Department of Physics, Rashtrasant Tukadoji Maharaj Nagpur University, Nagpur, India
e-mail: sbkondawar@yahoo.co.in

P. S. More
Department of Physics, Institute of Science, Mumbai, India

R.-I. Murakami et al. (eds.), *NAC 2019*, Springer Proceedings in Physics 242,
https://doi.org/10.1007/978-981-15-2294-9_1

the availability of higher boiling point components [1–5]. The gas sensing devices based on inorganic materials such as metal oxide semiconductors, which works on principle of the change in conductivity with interaction of gas molecules. However, they generally have a low selectivity to specific target gases and high operation temperature and thus increase power consumption, reduce sensor life, limit the portability, etc. [6]. Therefore, several different approaches have been explored in order to overcome these issues. A new approach is needed to increase this selectivity and sensitivity at room temperature (300 K). The room temperature operation is also an important criterion to achieve intrinsically safe performance in potentially hazardous situations. It has been pointed out that such sensors exhibit a fast, reversible response at room temperature [5, 6]. Conducting polymers, in comparison are another important category of low cost sensing material proven to have high sensitivity, fast response and room temperature operation and the possibility of tuning both chemical and physical properties by using different substituents [7, 8]. Polyaniline, polypyrrole, and polythiophene are most widely studied conducting polymers. Polyaniline is appealing because it is environmentally stable, easily synthesized, and can react with chemical species to behave as protonating or deprotonating agents to change their conductivity at room temperature. The conductivity depends on both the ability to transport charge carriers along the polymer backbone and for the carriers to hop between polymer chains. Any interactions with polyaniline that alters either of these processes will affect the conductivity [8, 9]. Nanocomposites are the combinations of two or more such nanosized objects or nanoparticles synthesized by some suitable techniques shows unique physical properties and wide application potential in diverse areas [10]. Sensing properties are sensitive to materials structure and morphology. In terms of sensitivity, response time, etc., PANI nanofibers were reported to exhibit better sensing properties than thin films because of the high surface-to-volume ratio brought about by the nanostructure [11]. Electrospinning is currently the most promising, relatively easy and fast technique to produce continuous one-dimensional conducting nanofibers on a large scale and the fiber diameter can be adjusted from nanometers to microns [12–14]. Electrospun conducting fibers are stably produced from blend solutions formed by mixing a conducting polymer and a nonconducting polymer, these fibers can have a handicap in terms of their electrical properties compared to pure conducting nanofibers and nanowires fabricated using methods such as electropolymerization and electrodeposition. A good strategy for improving the electrical properties of electrospun conducting fibers is to coat conducting polymer nanocomposites incorporate with MWCNTs on the surface of nonconducting nanofibers, which have superior electrical conductivity, into the conducting polymer [12]. PMMA (polymethylmethacrylate) is a well-known optical wave guiding polymer. PMMA being a pure dielectric has suitable optical properties and PANI can be synthesized to have suitable electrical properties. A composite of PANI/PMMA and PANI/MWCNT/PMMA can be tailored to have the superior synergistic properties of the materials [15].

Carbon nanotubes (CNTs) are an important group of nanomaterials with unique electronic and chemical properties. Since CNTs were discovered in 1991 by Iijima et al., there has been a growing interest among researchers to explore their unique

electrical, physical, mechanical and chemical properties to develop high performance devices in nanotubes for several applications. Researchers have been exploring the potential of Multiwalled carbon nanotubes (MWCNTs) in a wide range of applications: nanoelectronics, sensors, field emission, displays, hydrogen storage, batteries, polymer matrix composites, nanoscale reactors and electrodes. Due to the distortion of the electron clouds of MWCNTs from a uniform distribution in graphite to asymmetric distribution around cylindrical nanotubes, a rich π-electron conjugation forms outside of the MWCNTs, making them electrochemically active. Nanocomposites of a conducting polymer and MWCNTs show synergistic effect and have been made for different applications. MWCNTs have considerable potential in the field of polymer composites. Functionalized nanotubes treated with a mixture of concentrated H_2SO_4:HNO_3 are also more easily dispersed in organic solvents, leading to an improved dispersion and homogeneity of the MWCNTs within the polymer nanocomposite [16, 17]. Studies have revealed that modification of MWCNTs with conducting polymers can significantly enhance their gas sensing properties. Sensing mechanism of MWCNTs based sensor upon exposure to gas molecules mainly depends on the changes in their electrical properties due to charge transfer between MWCNTs and the gas molecules. MWCNT-based sensors are highly advantageous over traditional semiconducting metal oxide based sensors as they offer high conductivities under room temperature and require smaller device architecture. Despite their appealing properties of MWCNTs, poor sensitivity, lack of selectivity, very high recovery time, weak interaction with gas molecules limit their commercial applications. Various attempts have been made to overcome these problems by incorporating functionalized MWCNTs with various conducting polymers to significantly improve their sensor performance [8].

In this paper, poly(methyl methacrylate) (PMMA) nanofibers were prepared by electrospinning technique. On the surface of PMMA nanofibers, PANI was grown by in-Situ polymerization to obtain a composite of coaxial PANI/PMMA (abbreviated as PAPM) and PANI/MWCNT/PMMA (abbreviated as PACPM) nanofibers. The nanostructured composite was successfully studied as gas sensor. Its electrical responses towards LPG were measured at room temperature for various ppm.

1.2 Experimental

1.2.1 Materials/Chemicals

Aniline (99.5%) was procured from E. Merck and distilled under reduced pressure prior to use. MWCNTs from NPL Delhi, Acetone [$(CH_3)_2 \bullet CO = 58.08$] were procured from Fisher Scientific. Poly(methyl methacrylate) (PMMA) [Mol. Wt 3, 50,000] from sigma aldrich, Sulfuric acid, Hydrochloric Acid, Chloroform, Ammonium Persulphate (98%) and *N*,*N*-Dimethylformamide (DMF) were procured from

Merck and used as received. All chemicals were of analytical grade and solutions were prepared with double distilled water.

1.2.2 Synthesis of Poly(Methyl Methacrylate) (PMMA) Nanofibers

Nanofibers of PMMA were prepared by using electrospinning technique [18]. Typically, a solution of PMMA in dimethylformamide (DMF) was filled in a syringe bearing a hyperdermic needle, which was connected with a high-voltage power supply and electrospun at a voltage of 20 kV. An aluminium foil was grounded and worked as the collector. The distance between the needle tip and the grounded collector was 18 cm. The flow rate of the solution was kept at 0.4 mL/h [11, 15]. The electrospun PMMA nanofibers were collected and dried at 80 °C for overnight in vacuum oven.

1.2.3 Fabrication of PAPM and PACPM Nanofibers

In the typical reaction, 0.2M aniline oxidized with aqueous medium of 0.25M ammonium persulfate with dopeant HCl. Dip some amount of as-synthesized PMMA nanofibers into the aniline solution then add ammonium persulfate dropwise in aniline solution, briefly stirred, and left to polymerize at room temperature (~18–24 °C). Next day, the PAPM nanofibers were collected on a filter, washed with three 100-mL portions of 0.2M HCl, and similarly several times with distilled water. PAPM nanofibers were kept in vacuum oven at 60 °C. PANI prepared under these reaction and processing conditions are further referred to as "standard" samples [18–20]. For the synthesis of PACPM nanofibers, same reaction was followed as synthesis of PAPM but this time addition of fixed amount of functionalized MWCNTs with respect to the amount of aniline into the aniline solution was done. Schematic representation of the synthesis of PAPM nanofibers is shown in Fig. 1.1.

1.2.4 Characterizations

Morphological studies of the PMMA, PAPM and PACPM nanofibers were examine by Scanning Electron Microscopy (SEM, Carl Ziess, SEM EVO18). For Spectral analysis FT-IR spectra were obtained on a Thermo Nicolet, Avatar 370 infrared spectrometer from 400 to 4000 cm^{-1}. Spectrophotometric measurements were carried out by PerkinElmer UV/Vis Spectrometer Lambda 35 (in the wavelength range of 200–800 nm). Evaluation of X-ray diffraction (XRD) patterns were done by powder

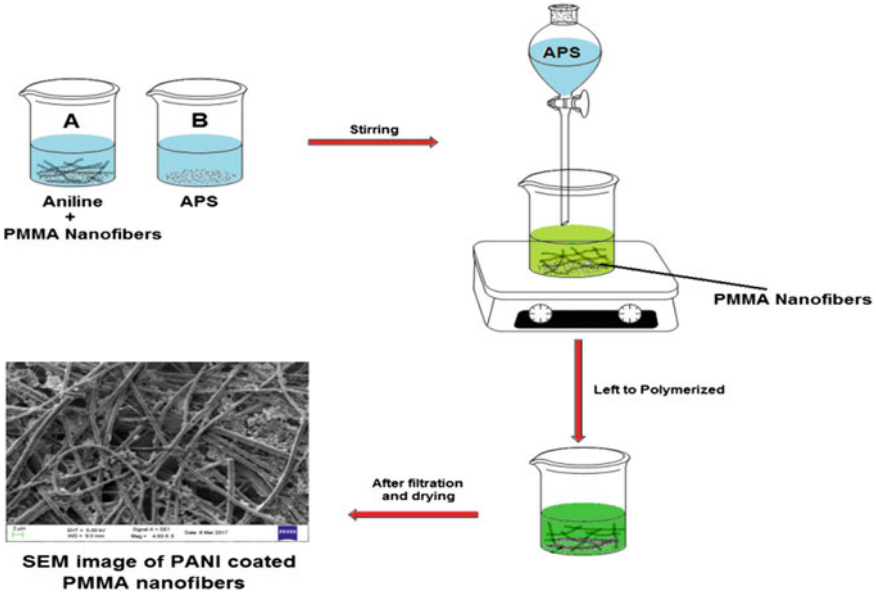

Fig. 1.1 Schematic representation of the synthesis of PAPM nanofibers

X-ray diffraction (Bruker AXS D8 Advance instrument (Cu-Kα, wavelength 1.540 Å and range of $2\theta = 10° - 90°$)).

1.3 Results and Discussions

1.3.1 Scanning Electron Microscopy (SEM)

SEM micrographs of PMMA, PAPM and PACPM nanofibers are presented in Fig. 1.2a–c with their respective histograms respectively. From Fig. 1.2a it can be seen that the nanofibers electrospun from PMMA in DMF solution with a concentration of 0.1 g/mL had a diameter 272 nm. Ji et al. reported that when the concentration of PMMA was increased 0.18–0.32 g/mL, the nanofibers obtained were much thicker, with a diameter up to 900 nm [11]. After the deposition of PANI on PMMA nanofibers by in-Situ polymerization, the diameters of fibers were increased to 502 nm in average. It is clearly seen that the composite nanofibers were quite smooth, with somewhat aggregations of PANI nanoparticles on the surface of PMMA nanofibers. The SEM observation indicates that smooth composite nanofibers have been successfully obtained. Furthermore, it is worth noting that the PAPM nanofibers showed good adherence to the underlying to electrodes, which may lead to a high sensitivity to the analyte. Figure 1.2c is the scanning electron micrograph of PACPM

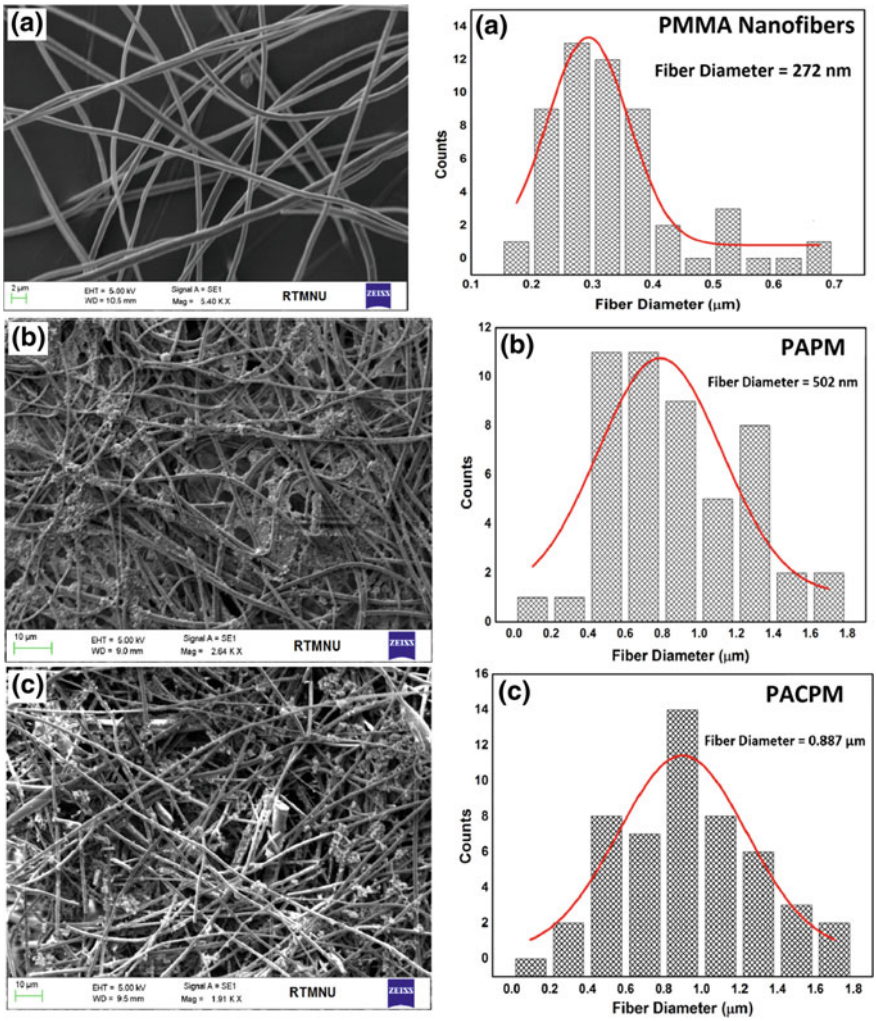

Fig. 1.2 Scanning electron micrographs of **a** PMMA nanofibers, **b** PAPM nanofibers, **c** PACPM composite nanofibers and their respective histograms

nanofibers and its histograms showing distribution of nanofibers diameters. The sample shows the same smooth nature of PMMA nanofibers having nanofiber diameter range of 272 nm, which was increased by the coating of PANI/MWCNTs nanocomposite during in situ polymerization. SEM shows that material coated properly and evenly. Histogram shows that the fiber diameter of PACPM nanofibers is increased to 0.887 μm after coating of PANI/MWCNTs nanocomposite.

1.3.2 FTIR Spectroscopy

FTIR spectra of PAPM and PACPM nanofibers are shown in Fig. 1.3. Yadav et al. reported that, the peaks for PMMA have been recorded at 1731 cm^{-1} for C=O stretching vibrations, 1260–1000 cm^{-1} for C–O (ester bond) stretching vibration, 950–650 cm^{-1} for C–H bending and 3000–2900 cm^{-1} for C–H stretching [15]. In FTIR spectra of PAPM nanofibers, the characteristic peak of PMMA at 1731.62 cm^{-1} (attributed to the –C=O stretching), 1244.64–983.65 cm^{-1} (attributed to ester bonding) and 754.32 cm^{-1}. The peak at 2950.69 cm^{-1} is due to the C–H stretching in PMMA. Peak at 1387.08 cm^{-1} is a characteristic peak of intrinsic PANI indicates C–N stretching. The main peak for PANI observed at 1149.90 and 836.82 cm^{-1} due to the vibration mode of B–NH=Q (benzene-NH-Quinone) or B–NH–B formed in doping reaction. This confirms the fact that PANI has been coated on the surface of PMMA nanofibers. In general, by the addition conducting polymer PANI to the thermoplastic polymer such as PMMA would enhance the optical and mechanical properties of composite nanofibers [15, 18, 21]. The dominant peak at 1149.90 cm^{-1} in the spectrum of both PAPM and PACPM nanofibers can be assigned to the characteristic conductivity peak of polyaniline correspond to "electronic like band" which is considered to be a measure of degree of delocalization of electrons. The introduction of MWCNTs in the polymer resulted in a difference in the intensity of the peaks compared to PAPM nanofibers. This is due to the presence of aniline monomers adsorbed on the surface of MWCNT, resulting in constrained polymerization of PANI on MWCNT confirming the formation of nanocomposite coated PMMA nanofibers. Such constrained motion and adhesion of the polymer chains during polymerization process may restrict the possible modes of vibration in the polymer leading to the difference in intensities in FT-IR spectra compared to PAPM. This interaction may significantly influence the charge transfer process within the polymer as well as

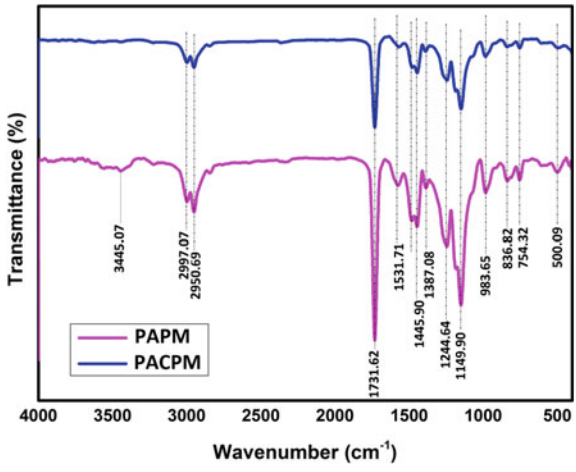

Fig. 1.3 FTIR spectra of PAPM and PACPM nanofibers

between PANI and MWCNT enhancing the conductivity of the composites. PANI has a tendency to strongly interact with the counter material, that is, MWCNTs, PMMA [8, 22, 23].

1.3.3 UV-Vis Spectroscopy

To investigate the interaction of MWCNTs nanomaterials with PANI and PMMA, the UV–visible absorption spectra of synthesized nanofibers were recorded and analyzed. Figure 1.4 shows the UV-Vis Spectrum of PAPM and PACPM nanofibers respectively. For taking UV-Vis spectra, materials were dissolved into the dimethylformamide (DMF) solution and the spectra taken in the range of 200–700 nm. In the spectrum of PAPM and PACPM nanofibers, 279 nm band is assigned to π-π* transition of benzenoid rings, the 328 nm one is assigned to polaron-π* transition, the large absorption band at 617 nm, in the form of a tail is assigned to polaronic bands (i.e. polaron-π* transition and π-polaron transitions) of lower and higher energy mobility and called the free carrier tail [8, 22]. This tail is important for conduction property and becomes more significant. They can be attributed to the polaron transition in the conjugated PANI chains [24]. A very broad tailing that appeared around 617 nm reveals that PANI is highly doped in the synthesized composite nanofibers [23, 25]. Increase in the intensity and red-shifting of the absorbance curve in PACPM nanofibers is due to the addition of MWCNTs into PANI matrix. Interactions between PANI chains and MWCNTs cause easy charge transfer [23].

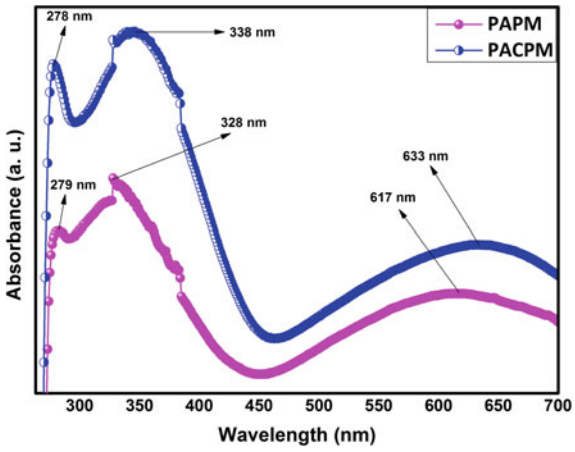

Fig. 1.4 UV-Vis spectra of PAPM and PACPM nanofibers

1.3.4 X-Ray Diffraction

Analysis of X-ray diffraction (XRD) patterns was used to investigate the structure of PAPM and PACPM nanofibers. XRD patterns were obtained in 2θ range between 0° and 90°. Figure 1.5 shows the XRD patterns of PAPM and PACPM nanofibers. XRD patterns of both the samples shows broad peaks at $2\theta = 13.48°$, 33.93° and 42.46°, which are attributed to presence of PMMA. PMMA is known to be an amorphous polymer [21, 26]. In the XRD pattern of PAPM nanofibers, slight sharpening of the main peaks of PANI at $2\theta = 16.89°$, 27.63° and 30.69°, assigned to the periodicity of the repeat unit of the PANI chain and the periodicity parallel to the polymer backbone chain with the broadening of the observed peaks in the PMMA pattern. This amorphous structure is obtained in PAPM nanofibers supporting that PAPM nanofibers formed by an interpenetrating network of PANI and PMMA in which the local ordering of somewhat destructed PANI chains [21, 27]. XRD pattern of PAPM and PACPM nanofibers showed similar peak patterns; therefore, it may be assumed that presence of PANI and MWCNTs did not cause any change in structure of PMMA. The amorphous structure of nanofibers is formed by an interpenetrating network of PANI, MWCNTs and PMMA in which the local ordering of PANI chains is destructed [21]. XRD pattern of PACPM nanofibers owing to the interactions of PANI chains with MWCNTs as indicated by little shifting in their corresponding peaks which mean there is definite chemical interaction between MWCNTs, PANI and PMMA [22].

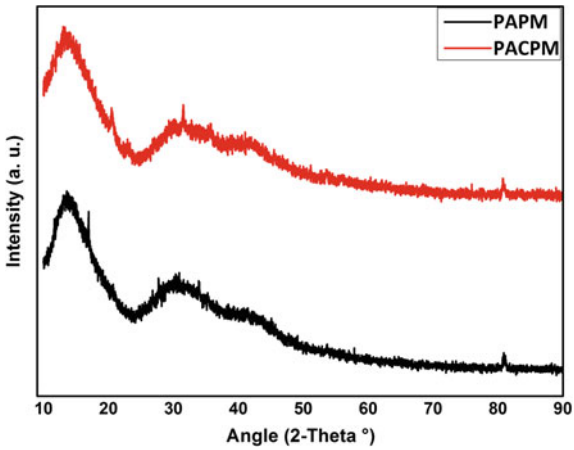

Fig. 1.5 XRD patterns of PAPM and PACPM nanofibers

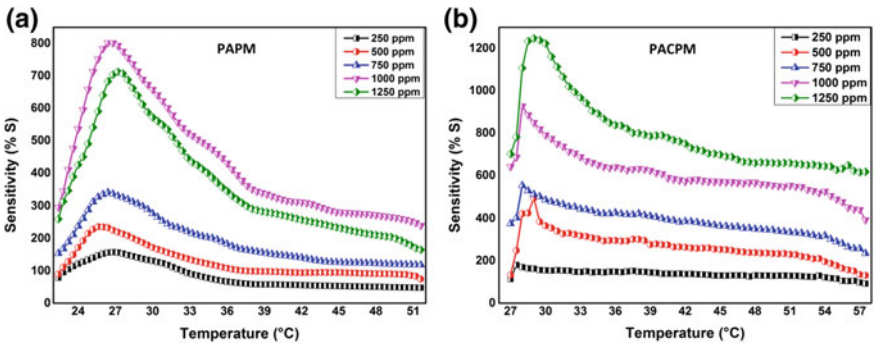

Fig. 1.6 Sensing behaviour of PAPM and PACPM nanofibers

1.3.5 LPG Sensing

The typical changes of the electrical resistance of the composite nanofibers upon interaction with LPG of different concentrations at room temperature are illustrated in Fig. 1.6. PAPM and PACPM nanofibers were tested at varying temperature range from room temperature to higher temperature in the absence and presence of LPG. From Fig. 1.6, it can be seen that the synthesized nanofibers showed a relatively high and fast response towards LPG ranging from 250 to 1250 ppm, which can be soon recovered upon flushing with air [12, 18, 28, 29]. The change in resistance was found in kilo-ohm range. The sensitivity was found to be increased with temperature and reached to the maximum sensitivity at particular temperature and then decreased for higher temperature [18]. LPG is reducing gas [30]. In case of PAPM nanofibers, sensitivity increased up to 26 °C but as the further temperature increased, it gets started to decrease the sensitivity. As the concentration of gas increases, sensitivity factor is also increased at room temperature. In case of PACPM nanofibers, same nature was followed but the sensitivity factor is higher than PAPM, for the range of ppms. It is generally proposed that nanostructured sensing materials exhibit a higher surface-to-volume ratio, thus provide more sites for adsorption of analyte molecules and achieve a higher sensitivity than their thin film counterparts [12, 18].

The electrical response of the PACPM nanofibers to LPG forms conducting paths inside the MWCNT/polymer composites due to quantum mechanical tunneling effects, where the distance between the conducting sticks is such that electron hopping can occur. The contact resistance between MWCNTs increases owing to an increase in distance between adjacent nanotubes. Swelling of the polymer matrix due to absorption of LPG may also increase the volume and thus increase the distance between nanotubes, thereby increasing the contact resistance. The extent of swelling, and hence the electrical response, depends on the solubility of the polymer in the solvent. Alternation of electronic properties of the semiconductor CNT surface occurs by charge transfer induced by adsorption of polar organic molecules. The adsorption of such molecules is due to the polar nature of surface as well as that of the solvent molecule [31].

Carbon nanotubes are a very sensitive material because they can easily interact with many gases and change their conductivity in the presence of several analytes at room temperature, even if these analytes have different chemical behaviour [32]. Because of the arrangement of the atoms on the surface of the MWCNTs and their high area/volume ratio, adsorption processes are highly favoured, which increases their sensitivity to the surrounding atmosphere. PANI can act as the sensing layer because it is more selective (although selectivity is not complete) than the raw MWCNTs, which then act as the transducer part. A change in the electrical conductivity of the MWCNTs caused by the effect of the analyte on their surface may have two consequences: they may promote a charge transfer from the analyte to the nanotubes, or the analyte may act as a scattering potential. The charge transfer increases the conductivity when the analyte adsorbed is an electron attractor (hole donation). If the analyte is an electron donor, the number of holes on the nanotubes will decrease, which leads to a decrease in the electrical conductivity [1]. LPG is electron donor, hence the resistance of PACPM nanofibers was increased when it exposed to LPG.

The sensing mechanism is complex and the possible cross interaction between the PANI and MWCNTs is not yet fully understood. It is known that during polymerization, emeraldine salt is formed onto the surface of MWCNTs, making the PANI a p-type semiconductor with N^+-H adsorption sites. The MWCNTs are also p-type semiconductors with holes as major charge carriers. A simplistic representation of the sensor calls for the PCPM nanofibers to be considered as two resistances in parallel. The current will essentially flow through the lowest resistance component. For PANI, the resistance change will be modulated by the protonation-deprotonation brought by LPG. As LPG molecule adsorbs onto or is absorbed into the polymer, LPG (Which is simply a mixture of butane, propane, butylene and propylene) molecules withdraw protons from N^+-H sites. This deprotonation process reduces PANI from the emeraldine salt state to the emeraldine base state, leading to reduced hole density in the PANI and thus an increased electrical resistance. When the sensor is purged with air, the process is reversed and the initial doping level and electrical resistance are restored. In addition to the two-resistance in parallel model, PACPM nanofibers can be considered as one p-type semiconductor network. The interaction between PANI and MWCNTs may increase the p-electron delocalization which leads to the higher charge transfer between PANI and MWCNT. Detailed investigations of the sensing mechanism are warranted [33].

The main advantage of nanostructured materials is considered to be related with the enlargement of active surface area for adsorption. According to adsorption law, the adsorption ability of an adsorbent is greatly determined by its surface area [34]. Addition of MWCNTs into the polymeric matrix of PACPM nanofibers increases the surface area to volume ratio, which provides more active sites for adsorption of gas molecules leads to a larger response because gas molecules can penetrate hybrids rapidly and allow more opportunities for reaction. Moreover, they enhance intrinsic charge transport due to high carrier mobility. MWCNT plays important roles in improving the charge transport because MWCNT has extremely high mobility compared to PANI. Thus, the addition of MWCNT in the polymer matrix created an easier path for charge transport between electrodes, even in small amount of

LPG [35]. From Fig. 1.6 it can be seen that, the sensitivity of PAPM and PACPM nanofibers is almost same i.e. 154.94 and 177.35 respectively for 250 ppm at room temperature. LPG is a mixture of hydrocarbons. The molecules of hydrocarbons are nonpolar because the atoms in the molecules have same electronegativity. Hence, alteration of electronic properties of semiconductor couldn't be occurring. This very less change in sensitivity observed may be due to the less amount of LPG get absorbed on the PACPM nanofibers. Very less amount of LPG couldn't generate more carriers and form sufficient conducting paths for the charge transport due to carrier mobility inside PACPM nanofibers by which the electron hopping occur. As the amount of gas increases, more conducting paths get created and hence PACPM nanofibers sense more LPG and shows good sensitivity at room temperature [31].

Figure 1.7 shows the Sensitivity versus concentration plot for PAPM and PACPM nanofibers. From the graph it can be seen that as the ppms of LPG increases, the sensitivity factor of PAPM and PACPM nanofiber increases. But the sensitivity of PACPM nanofibers is higher than PAPM nanofibers [36].

Figure 1.8a, b shows the dynamic variation of the response of the PAPM and PACPM nanofibers sensor with time upon exposure to 250–1250 ppm of LPG at room temperature. The figure revealed that the initially the response of sensor nanofibers increase with increasing the concentration of LPG. At 1250 ppm, PAPM and PACPM nanofibers sensor showed the maximum response of 6.83 and 11.85 respectively. Such a higher value of response is believed to be due to the sensitivity of the semiconductor sensors mainly determined by the interactions between the target gas and the surface of the sensor. So, it is obvious that for the materials of greater surface area, the interactions between the adsorbed gases and the sensor surface are significant [6, 37]. Depending on LPG concentration, the response time (defined as the time to reach 90% of the total resistance change) of PAPM and PACPM nanofibers sensors to LPG exposure was on the order of a few seconds, while recovery time ranged from several seconds to a few minutes for the sensor to recover to its original resistance [33].

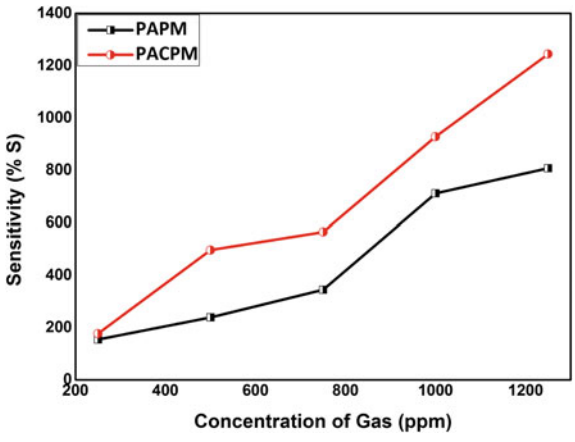

Fig. 1.7 Sensitivity versus concentration for PAPM and PACPM nanofibers

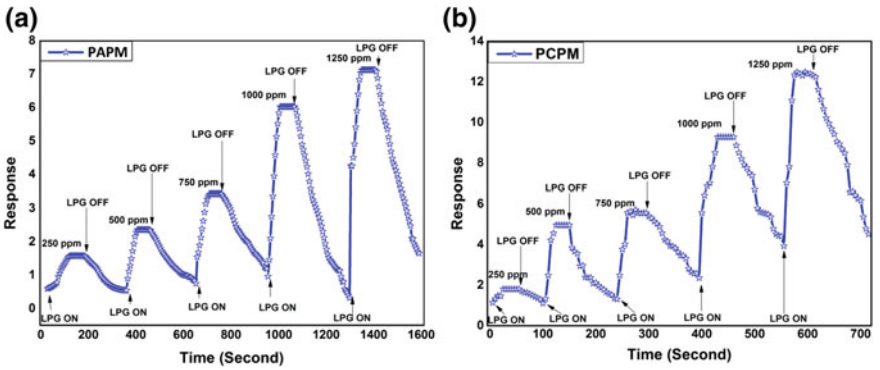

Fig. 1.8 Sensing response and reversibility for **a** PAPM and **b** PACPM Nanofibers

From graphs, it can be seen that the composite nanofibers showed a relatively high and fast response towards LPG ranging from 250 to 1250 ppm as the sample have porous fibrous structure in which the gas analytes accommodate easily. The response time of PAPM and PACPM was found to be 8 s and 13 s respectively for 1250 ppm with maximum response of 6.83 and 11.85 respectively. But the response time for PAPM and PACPM for the range 250–1000 ppm is almost same. Samples showed good reproducible resistance change for a number of cycles [38].

The average response and recovery times for PAPM and PACPM nanofibers are faster than the response time of the PAPM nanofiber [18]. From the same graph, it is found that for higher concentrations of LPG, the recovery time was long. This may probably be due to the heavier nature of LPG and the reaction products are not leaving from the interface immediately after the reaction [6, 18]. The responses with good recovery can be a great advantage for the potential application of the PAPM and PACPM nanofibers [8, 18].

Figure 1.9 shows the stability curve of PAPM and PACPM nanofibers. The sensitivity of these samples was studied for 10 days for 250 ppm of LPG at room temperature. It has been observed that the sensitivity value of the samples was found to be very little change when tested for 10 days indicating the good stability of these samples towards 250 ppm of LPG at room temperature (27 °C). Hence, the synthesized composite nanofibers of PAPM and PACPM nanofibers are the very stable sensing materials for LPG.

1.4 Conclusions

PAPM and PACPM nanofibers were prepared by using electrospinning technique and an in-Situ chemical oxidative polymerization method. SEM micrograph of PMMA, PAPM and PACPM nanofibers with their respective histogram shows that the average diameter of the fibers was increased by the coating of PANI and PANI/MWCNT

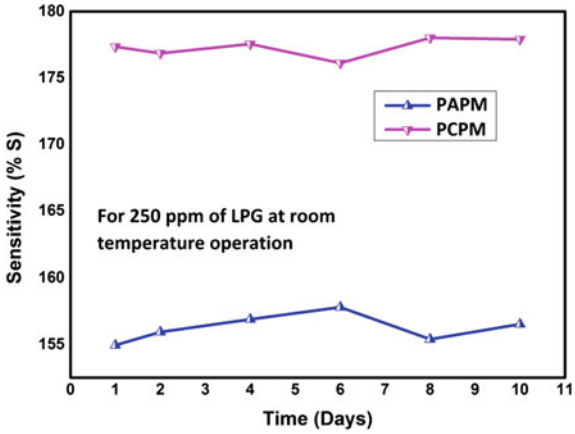

Fig. 1.9 Stability curve for PAPM and PACPM nanofibers

nanocomposites. UV-Vis, FT-IR and XRD analyses confirmed the formation of PANI and its interaction with MWCNTs. Sensitivity study shows that materials under investigation are found to be highly sensitive for LPG near to room temperature. The dynamic variation of the response of PAPM and PACPM nanofibers shows sensor upon exposure to 250–1250 ppm of LPG at room temperature revealed that initially the response of sensor nanofibers increase with increasing the concentration of LPG. From response curves of the nanofibers it was observed that for repeated exposure and removal of LPG (250–1250 ppm), PAPM and PACPM nanofibers showed good reproducible resistance change for a number of cycles. Stability plot explains that, the synthesized nanofibers of PAPM and PACPM are the very stable sensing materials for LPG.

Acknowledgements The authors are thankful to UGC (India) for providing financial assistance and BSR Fellowship to carry out this research work File No. F.39-540/2010(SR) and F.4-1/2006(BSR)/7-154/2007(BSR).

References

1. G. Jimenez-Cadena, J. Riu, F. Xavier Rius, Gas sensors based on nanostructured materials. RSC Analyst **132**, 1083–1099 (2007)
2. K. An, S. Jeong, H. Hwang, Y. Lee, Enhanced sensitivity of gas sensors incorporating single walled carbon nanotubes-polypyrol nanocomposites. Adv. Mat **16**, 1005–1009 (2004)
3. S. Pandey, Highly sensitive and selective chemiresistor gas/vapor sensors based on polyaniline nanocomposite: a comprehensive review. J. Sci. Adv. Mater. Devices **1**, 431–453 (2016)
4. R. Singh, N. Kohli, M. Singh, O. Singh, Ethanol and LPG sensing characteristics of SnO_2 activated Cr_2O_3 thick film sensor. Bull. Mater. Sci. **33**, 575–579 (2010)
5. D. Dhawale, D. Dubal, A. More, T. Gujar, C. Lokhande, Room temperature liquefied petroleum gas (LPG) sensor. Sens. Actuators B **147**, 488–494 (2010)

6. D. Dhawale, D. Dubal, V. Jamadade, R.R. Salunkhe, S. Joshi, C. Lokhande, Room temperature LPG sensor based on n-CdS/p-polyaniline heterojunction. Sens Actuators B **145**, 205–210 (2010)
7. I. Fratoddia, I. Vendittia, C. Camettib, M. Russo, Chemiresistive polyaniline-based gas sensors: a mini review. Sens Actuators B **220**, 534–548 (2015)
8. S. Abdulla, T. Mathew, B. Pullithadathil, Highly sensitive, room temperature gas sensor based on polyaniline-multiwalled carbon nanotubes (PANI/MWCNTs) nanocomposite for trace-level ammonia detection. Sens Actuators B **221**, 1523–1534 (2015)
9. S. Virji, J. Huang, R. Kaner, B. Weiller, Polyaniline nanofiber gas sensors: examination of response mechanisms. Nano Lett. **4**, 491–496 (2004)
10. R. Gangopadhyay, A. De, Conducting polymer nanocomposites: a brief overview. Chem. Mater. **12**, 608–622 (2000)
11. S. Ji, Y. Li, M. Yang, Gas sensing properties of a composite composed of electrospun poly(methyl methacrylate) nanofibers and in situ polymerized polyaniline. Sens. Actuators B **133**, 644–649 (2008)
12. M. Shin, Y. Kim, S. Kim, S. Kim, H. Lee, G. Spinks, S. Kim, Enhanced conductivity of aligned PANi/PEO/MWNT nanofibers by electrospinning. Sens. Actuators B **134**, 122–126 (2008)
13. F. Jian, N. Tao, L. Tong, W. Gai, Applications of electrospun nanofibers. Chin. Sci. Bull. **53**, 2265–2286 (2008)
14. B. Aronggaowa, M. Kawasaki, T. Shimomura, Thin, transparent conductive films fabricated from conducting polymer nanofibers. Polym. J. **5**, 819–823 (2013)
15. J.B. Yadav, B. Patil, R. Puri, V. Puri, Studies on spin coated PANI/PMMA composite thin film: effect of post-deposition heating. Appl. Surf. Sci. **255**, 2825–2829 (2008)
16. T. Zhang, S. Mubeen, N. Myung, M. Deshusses, Recent progress in carbon nanotube-based gas sensors. Nanotechnology **19**, 332001–332014 (2008)
17. R. Sabzi, K. Rezapour, N. Samadi, Polyaniline–multi-wall-carbon nanotube nanocomposites as a dopamine sensor. J. Serb. Chem. Soc. **75**, 537–549 (2010)
18. P. Patil, R. Anwane, S. Kondawar, Development of electrospun polyaniline/ZnO composite nanofibers for LPG sensing. Procedia Mater. Sci. **10**, 195–204 (2015)
19. J. Stejskal, R. Gilbert, Polyaniline preparation of a conducting polymer. Pure Appl. Chem. **74**, 857–867 (2002)
20. I. Sapurina, J. Stejskal, The mechanism of the oxidative polymerization of aniline and the formation of supramolecular polyaniline structures: polymer international. Polym. Int. **57**, 1295–1325 (2008)
21. A. Fattoum, F. Gmati, N. Bohli, A. Arous, A. Mohamed, Effects of the matrix molecular weight on conductivity and dielectric relaxation in plasticized polyaniline/polymethylmethacrylathe blends. J. Phys. D: Appl. Phys. **41**, 095407–095416 (2008)
22. V. Gautam, A. Srivastava, K. Singh, V. Yadav, The mechanism of the oxidative polymerization of aniline and the formation of supramolecular polyaniline structures. Polym. Compos. 1–11 (2015)
23. L. Shi, R. Liang, J. Qiu, Controllable deposition of platinum nanoparticles on polyaniline-functionalized carbon nanotubes. J. Mater. Chem. **22**, 17196–17203 (2012)
24. M. Chougule, S. Sen, V. Patil, Facile and efficient route for preparation of polypyrrole-ZnO nanocomposites: microstructural, optical, and charge transport properties. J. Appl. Polym. Sci. **125**, E541–E547 (2012)
25. A. Mostafaei, A. Zolriasatein, Synthesis and characterization of conducting polyaniline nanocomposites containing ZnO nanorods. Prog. Nat. Sci. Mater. Int. **22**, 273–280 (2012)
26. N. El-Zaher, M. Melegy, O. Guirguis, Thermal and structural analyses of PMMA/TiO2 nanoparticles composites. Nat. Sci. **6**, 859–870 (2014)
27. Q. Yao, J. Chang, L. Chen, Enhanced thermoelectric properties of CNT/PANI composite nanofibers by highly orienting the arrangement of polymer chains. J. Mater. Chem. **22**, 17612–17618 (2012)
28. S. Kondawar, P. Patil, S. Agrawal, Chemical vapour sensing properties of electrospun nanofibers of polyaniline/ ZnO nanocomposites. Adv. Mat. Lett. **5**, 389–395 (2014)

29. S. Kondawar, S. Agrawal, S. Nimkar, H. Sharma, P. Patil, Conductive polyaniline-tin oxide nanocomposites for ammonia sensor. Adv. Mat. Lett. **3**, 393–398 (2012)
30. F. Tudorache, N. Rezlescu, N. Tudorache, A. Catargiu, M. Grigoras, Polyaniline and polythiophene-based gas sensors. Optoelectron. Adv. Mater. Rapid Commun. **3**, 379–382 (2009)
31. B. Philip, J. Abraham, A. Chandrasekhar, V. Varadan, Carbon nanotube/PMMA composite thin films for gas-sensing applications. Smart Mater. Struct. **12**, 935–939, 2003
32. H. Guerin, H. Poche, R. Pohle, E. Buitrago, M. Badía, J. Dijon, A. Ionescu, Carbon nanotube gas sensor array for multiplex analyte discrimination. Sens. Actuators B **207**, 833–842 (2015)
33. T. Zhang, B. Megan, M. Nix, B. Yoo, M. Deshusses, N. Myung, Electrochemically functionalized single-walled carbon nanotube gas sensor. Electroanalysis **18**, 1153–1158 (2006)
34. K. Yan, Y. Toku, Y. Ju, Highly sensitive hydrogen sensor based on a new suspended structure of cross-stacked multiwall carbon nanotube sheet. Int. J. Hydrogen Energy **055**, 1–9 (2019)
35. S. Park, C. Park, H. Yoon, Chemo-Electrical Gas Sensors Based on Conducting Polymer Hybrids. Polymers **9**, 155 (2017)
36. H. Tai, Y. Jiang, G. Xie, J. Yu, X. Chen, Z. Ying, Influence of polymerization temperature on NH3 response of PANI/TiO2 thin film gas sensor. Sens. Actuators B **129**, 319–326 (2008)
37. S. Patil, M. Chougule, S. Sen, V. Patil, Measurements on room temperature gas sensing properties of CSA doped polyaniline–ZnO nanocomposites. Measurement **45**, 243–249 (2012)
38. N. Deshpande, Y. Gudage, R. Sharma, J. Vyas, J. Kim, Y. Lee, Studies on tin oxide-intercalated polyaniline nanocomposite for ammonia gas sensing applications. Sens. Actuators B **138**, 76–84 (2009)

Chapter 2
Colour Tunable Photoluminescence from Samarium and Dysprosium Co-doped ZnO Nanofibers

Chaitali N. Pangul, Shyamkant W. Anwane and Subhash B. Kondawar

Abstract Electrospinning technique was used for the fabrication of samarium (Sm) dysprosium (Dy) co-doped ZnO nanofibers for colour tunable photoluminescence. The prepared nanofibers were characterized by SEM, EDX, XRD, UV-Vis and FTIR. Nanofibers diameter and morphology was studied through SEM and the diameter was found to be in the range of 100–180 nm while presence of elemental Zn, O, Dy and Sm was assured by EDX spectrum. XRD study reveals the crystalline structure while the presence of metal stretching bond of ZnO was observed around 450 cm^{-1} in FTIR studies. A tremendous enhancement in band gap was observed by UV-Vis spectrum. Photoluminescence spectra clearly depicts the energy transfer mechanism within the host ZnO and dopants Sm and Dy wherein CIE parameter confirms the colour tunability of co-doped ZnO nanofibers. Such materials can be a very good optimum candidate for colour tunable luminescent light emitting fabrics.

2.1 Introduction

One Dimensional Nanofibers had been seeking the attention in multiple research areas due to their exceptional physical and morphological properties. High aspect ratio and huge surface area to volume ratio has empowered to fetch the optimum results for the variety of applications [1–3]. Among the various methods of synthesizing nanofibers, Electrospinning had marked an unreplaceable position [4, 5]. Electrospun nanofibrous membranes are considered the chief promising and versatile filter media for fine particle filtration, possess several fascinating features such as remarkable specific surface area, high open porosity, and interconnected porous structure. More significantly, electrospun nanofiber-based filter media are expected to have extremely high filtration efficiency for fine particle and relatively low pressure drop due to the unique structure of electrospun nanofibers [6]. Functional garments

C. N. Pangul · S. B. Kondawar (✉)
Department of Physics, Rashtrasant Tukadoji Maharaj Nagpur University, Nagpur, India
e-mail: sbkondawar@yahoo.co.in

S. W. Anwane
Department of Physics, Shri Shivaji Science College, Nagpur, India

R.-I. Murakami et al. (eds.), *NAC 2019*, Springer Proceedings in Physics 242,
https://doi.org/10.1007/978-981-15-2294-9_2

with both robust waterproofness and breathability fabricated by Electrospinning technology had overcome the negative relationship between protective properties and comfort [7]. However, electro spun fibres generally exhibit a lower optical extinction capacity than the commonly used fibres because of their much smaller diameters [8]. Nanoparticles with excellent capabilities of refraction and absorption are generally incorporated into the polymer to improve the optical extinction capacity [9]. Zinc Oxide is one of the most eligible aspirants for enhancing the further properties of any material. Due to novel properties like high refractive index, binding energy, high thermal conductivity, antibacterial and UV protection of ZnO, it could be used in many materials and products [10]. Wurtzite zinc oxide is a typical native n-type semiconductor with a wide and direct band gap (3.37 eV) and a high exciton binding energy (60 meV) at room temperature and excellent chemical stability [11]. Various applications depend on ZnO properties that are influenced by different factors like deposition conditions, chemical composition, ZnO structural, defects and preferential orientation [12]. Photoluminescence properties for light emitting fibers had been studied as a fact of need for Smart and Technical Fabrics and Devices [13]. Zinc oxide is proved to enhance the light emitting properties when doped with optimum materials like Rare earth ions [14]. Martínez et al., had studied the influence of rare earth ion substitution properties of ZnO nanoparticles and found that magnetic and optical properties of Er^{3+} and Yb^{3+} ions play a significant role in the modification of electronic structure of ZnO resulting in remarkable magnetodielectric and photo dielectric effects which could be conjugated for different multifunctional photo-capacitors for operating microelectronics devices with light and magnetic field [15]. Fang et al., studied the effect of doping of La into ZnO nanostructure for efficient photocatalytic properties [16]. Wu et al., found Strong up-conversion luminescence of rare-earth doped oxide films enhanced by gap modes on ZnO nanowires due to the combined effect of the local confinement of the electric field in the spaces between the ZnO and reflections at the Ag layer [17]. Abdellah et al., hexagonal single-crystal perovskite-like nanofibers were tested as novel substrate materials for surface-enhanced Raman spectroscopy, showing exceptional performance [18]. Yang Ding et al., fabricated $CaMoO4:Ln^{3+}$ nanofibers based LEDs which present high efficiency and stability. These single-doped CaMoO4 nanofibers showed stronger emission, and the photoluminescence quantum efficiency [19]. Photoluminescent nanofibers were studied on a very wide aspect but still RE doped ZnO nanofibers needs to be investigated with reference to improved luminescence properties of ZnO via energy transfer process within dopant and host.

In this work, we report the fabrication and characterization of Samarium and Dysprosium co-doped ZnO nanofibers via Electrospinning process. The fabricated electro spun nanofibers were characterized by SEM, EDX, UV-Vis spectroscopy and FTIR strategies. Photoluminescence properties were also investigated in order to study the effect of dopant on the luminescence properties of ZnO. Energy transfer mechanism and CIE parameter were also studied. Efficient energy transfer mechanism was observed within the co-dopants and host ZnO which enables the ZnO to emit in visible range overcoming its defect state visible emission.

2.2 Experimental

Zinc Acetate dihydrate ($Zn(CH_3COO)_2 \cdot 2H_2O$); LobaChemie with 99.5% purity, RE(III) nitrate hydrate ($RE(NO_3)_3$); Sigma Aldrich with 99.9% purity, Poly Vinyl Alcohol (PVA); Sigma Aldrich mol. wt 89,000 were used as the starting materials. All the materials were used without further purification. The very first solution was prepared by dissolving 0.5 gm of zinc acetate dihydrate and x% of $(Dy(NO)_3)_3$ and 2% of $(Sm(NO)_3)_3$ in 1 mL of deionised water under magnetic stirring. Another solution was made by dissolving 0.35 gm of PVA in 5 mL of deionised water at 60 °C under continuous magnetic stirring for 2 h. Additional 0.059 mL of glacial acetic acid was added after mixing the first two solutions by continuous magnetic stirring for another 2 h. The resultant solution was filled in the syringe and electrospinning experiment was carried out. A constant high voltage potential of 20 kV was applied to the tip of the syringe and the ground was connected to the surface collector. The distance between the tip of the syringe and ground collector was maintained at 15 cm. The so formed electro spun fibers were first dried overnight in oven and then calcinations were performed at 300 °C for 2 h.

2.3 Results and Discussions

2.3.1 Scanning Electron Microscopy

Figure 2.1 represents the SEM images along with frequency distributions of x% Dy 2% Sm doped ZnO nanofibers. Figure 2.1a is the SEM image of 1% Dy 2% Sm doped ZnO doped ZnO nanofibers, Fig. 2.1b is the SEM image of 2% Dy 2% Sm doped ZnO nanofibers and Fig. 2.1c is the SEM image of 3% Dy 2% Sm doped ZnO nanofibers. From all the figures it is very evident that ultralong and continuous nanofibers are formed by the process of Electrospinning. The average diameter is found to be in the range of 100–160 nm for all the samples.

2.3.2 Energy Dispersive X-Ray Spectroscopy (EDX)

Figure 2.2 is the EDX spectra for x% Dy 2% Sm doped ZnO nanofibers. Figure 2.2a is the EDX spectrum for 1% Dy 2% Sm doped ZnO nanofibers, Fig. 2.2b is the EDX spectrum for 2% Dy 2% Sm doped ZnO nanofibers and Fig. 2.2c is the EDX spectrum for 3% Dy 2% Sm doped ZnO nanofibers. Presence of peaks for Zn, O, Sm and Dy confirms the presence of elemental Zinc, Oxygen, Samarium and Dysprosium. Additional peak of Carbon represents the presence of carbonaceous material due to calcination process.

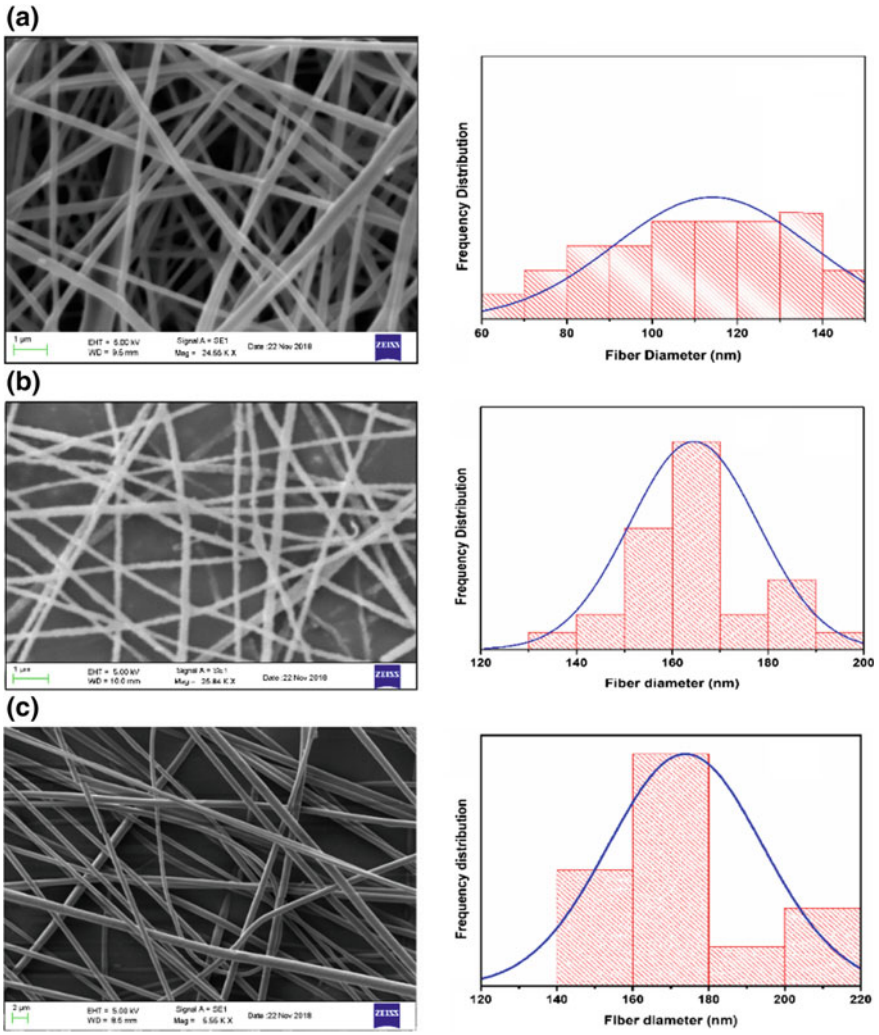

Fig. 2.1 **a** SEM image and frequency distribution of 1% Dy-2% Sm-doped ZnO nanofibers, **b** SEM image and frequency distribution of 2% Dy-2% Sm-doped ZnO nanofibers, **c** SEM image and frequency distribution of 3% Dy-2% Sm-doped ZnO nanofibers

2.3.3 X-Ray Diffraction

XRD patterns for x% Dy 2% Sm doped ZnO nanofibers are shown in Fig. 2.3. The samples clearly exhibit the diffraction peaks for wurtzite hexagonal structure of ZnO. Diffraction peaks at (100), (002) and (101) are the characteristic diffraction peak for crystalline ZnO. No other crystalline phase related to other impurity regarding Dy or Sm is observed indicating the successful incorporation of dopants into ZnO. A

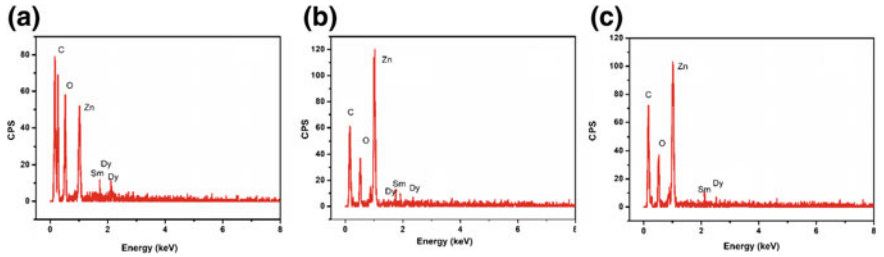

Fig. 2.2 EDX spectra of **a** 1% Dy 2% Sm doped ZnO, **b** 2% Dy 2% Sm doped ZnO, and **c** 3% Dy 2% Sm doped ZnO nanofibers

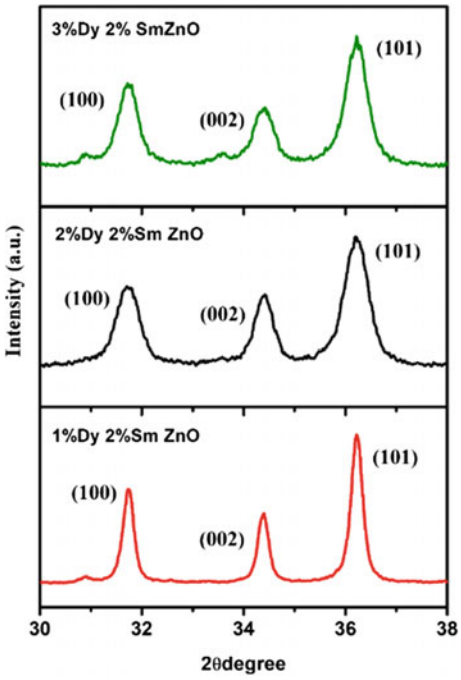

Fig. 2.3 XRD patterns of x% Dy-2% Sm-doped ZnO nanofibers

gradual shift has been observed in 2θ degree for all the diffraction peaks was observed which implies that the dopants had occupied Zn^{2+} sites [20].

2.3.4 UV-Vis Spectroscopy

Figure 2.4 is the absorbance spectra and Tauc's plot for Dy/Sm co-doped ZnO nanofibers. The absorption maxima is found to be blue shifted as compared to bulk ZnO. This could be explained with the help of Quantum confinement effect. Since the

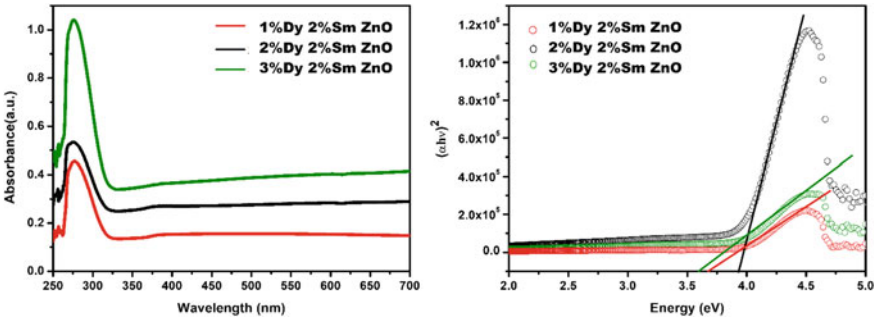

Fig. 2.4 UV-Vis absorbance spectra and Tauc's plot for Dy/Sm co-doped ZnO nanofibers

diameter of the nanofibers is in the range of 100 nm, the crystalline ZnO nanoparticles are assumed to be smaller than that and hence with the reduction of the diameter size the optical properties tends to enhance significantly [21]. Along with the blue shift in the absorbance maxima the band gap is enhanced tremendously with the reduction in the diameter size of nanofibers. With increasing dopant concentration, the band is found to be increased. For 2% Dy 2% Sm doped ZnO nanofibers the band gap is found to enhanced most and for further increasing dopant concentration the band gap starts reducing. This tailoring of band gap with dopant concentration could be explained by two terminologies, namely Burstein-Moss effect and other is Band gap narrowing. Due to increasing carrier concentration the Fermi level in the conduction band moves upwards, this is termed as Burstein-Moss effect whereas the latter occurs due to merger of the donor level and the conduction band above a critical carrier concentration termed as Mott density [22–24]. For optimal dopant concentration movement of Fermi level occurs, whereas when the concentration is increased further it results in concentration quenching.

2.3.5 Fourier Infrared Transform Spectroscopy (FTIR)

Figure 2.5 is the Fourier Transform Infrared Spectra for x% Dy 2% Sm doped ZnO nanofibers. All the samples confirms the presence of strong metal stretching bond Zn–O at around 450 cm^{-1} [25, 26]. This indicates the successful formation of ZnO in one dimensional nanofibers. Additional broad peak at 3500 cm^{-1} is observed. This resembles the presence of –OH which could be ascribed to the presence of ambient moisture retention [27].

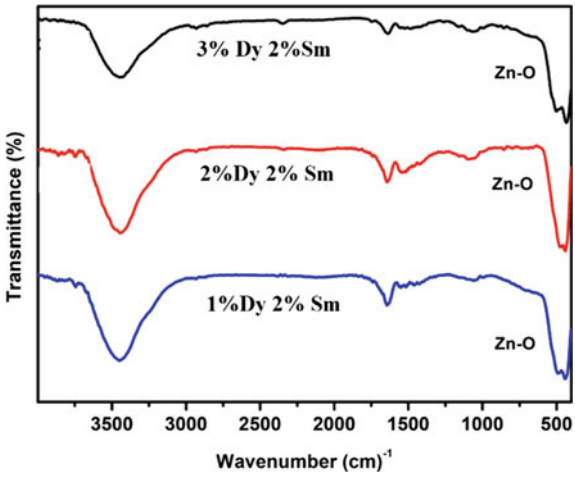

Fig. 2.5 FTIR spectra for x% Dy 2% Sm doped ZnO nanofibers

2.3.6 Photoluminescence

Figure 2.6 represents the photoluminescence spectra of dysprosium and samarium co-doped ZnO nanofibers. Figure 2.6a is the PL spectrum for 1% Dysproium and 2% Samarium doped ZnO nanofiber. It posses a NBE from host ZnO [28] and two characteristic emission from Samarium following $^4G_{5/2} \rightarrow {}^6H_{7/2}$ transition and $^4G_{5/2} \rightarrow {}^6H_{9/2}$ transition [29]. No peak related to Dysprosium emission is observed. Thus, the non-radiative energy transfer from Dy^{3+} ions to Sm^{3+} ion may had occurred. Figure 2.6b is the PL spectrum for 2% Dysprosium 2% Samarium doped ZnO nanofibers. It clearly possesses the NBE emission accompanied by the characteristic peaks for Dysprosium and Samarium [30]. Also, the intensity of the $^4G_{5/2} \rightarrow {}^6H_{9/2}$ transition is bit increased. Thus, dopant Dysprosium acts as the activator ion which sensitizes Samarium intensity. While Fig. 2.6c is the PL spectrum for 3% Dysprosium 2% Samarium doped ZnO nanofibers. Here no emission peak related to either of the dopant is observed. This led to the discussion that with the increase

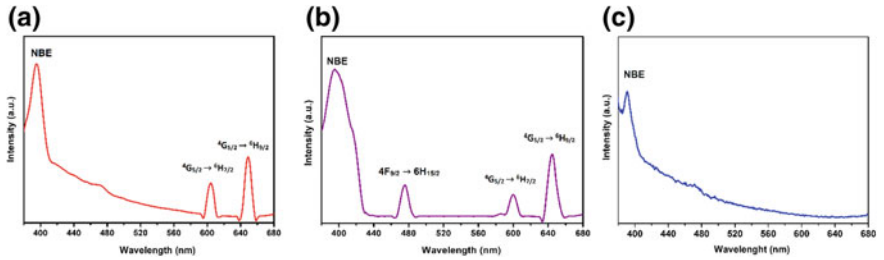

Fig. 2.6 Photoluminescence emission spectra of **a** 1% Dy 2% Sm doped ZnO, **b** 2% Dy 2% Sm doped ZnO, and **c** 3% Dy 2% Sm doped ZnO nanofibers

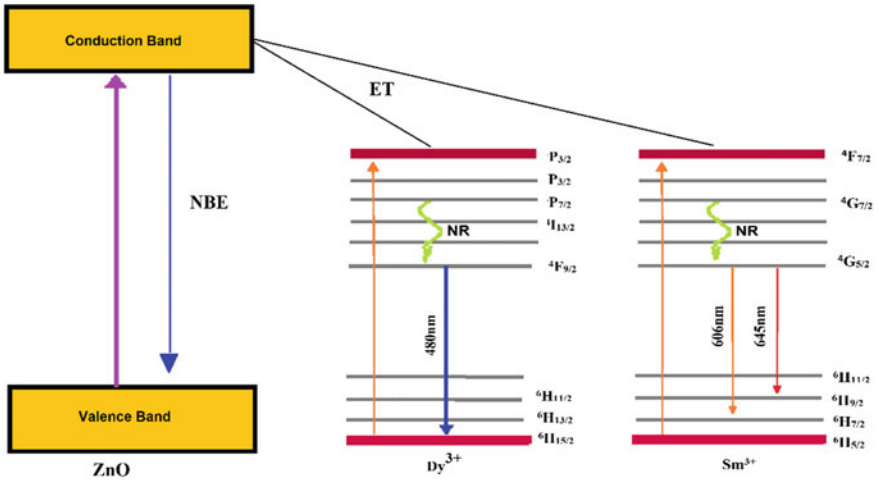

Fig. 2.7 Energy Transfer mechanism of host ZnO and dopant ions Dy^{3+} and Sm^{3+}

in doping concentration of Dysprosium characteristic peak for Dysprosium emerges but upon further increase the peak related to any of the dopants diminish. This could be explained as concentration quenching effect. Since a greater number of dopants when exists the energy is transferred from activator to activator and ultimately the energy is lost and does not result in effective emission from the dopant [31].

Figure 2.7 depicts the Energy transfer mechanism within the host ZnO and dopant ions Dy^{3+} and Sm^{3+}. Upon excitation the host ZnO gets excited to the conduction band. This excited ZnO then relaxes via two paths i.e. one is returning back to ground state and hence emitting into UV region and other is by transferring its energy to its dopants. This is referred and Energy transfer mechanism. The excited dopant ions then come back to ground state while emitting light in their characteristic region. Figure 2.8 illustrate the Commission Internationale de l'Elairage diagram (CIE) for x% Dy 2% Sm doped ZnO nanofibers. The CIE parameters such as colour coordinates, colour co-related temperature (CCT), luminescence efficacy of radiation (LER) and colour rendering Index (CRI) were calculated to know the photometric characteristics of the prepared nanofibers [32]. Colour coordinates (x, y) are one of the important parameter for evaluating luminescent materials performance. From chromaticity diagram, it is seen that the colour co-ordinates travel from warm orange white region to cool blue white region as the percentage of Dy increases from 1 to 3% while keeping 2% Sm fixed doping in ZnO. Thus, it could be clearly stated that the colour tunability can be achieved by varying the dopant concentrations and variety of dopants. It is evident from obtained values of CCT, CRI and LER as given in Table 2.1, ensures the use of these light emitting nanofibers in Light emitting devices, smart and technical textiles.

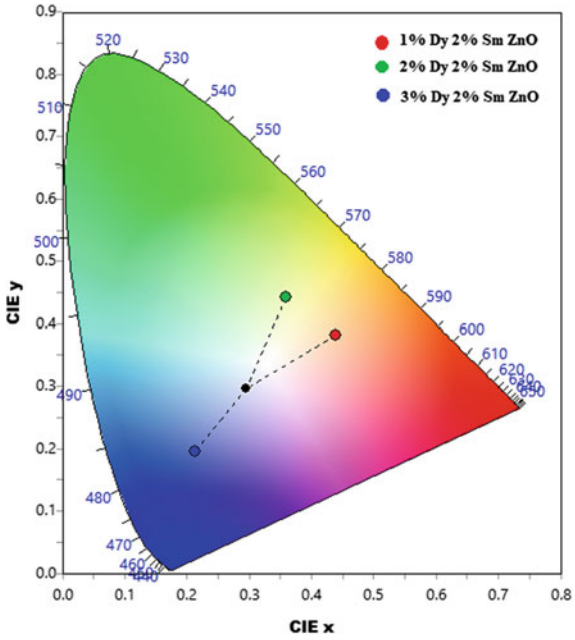

Fig. 2.8 CIE plot for Dy/Sm co-doped ZnO nanofibers

Table 2.1 CIE parameters for Samarium Dysprosium co-doped ZnO nanofibers

Samples	CIE x	CIE y	CRI	CCT	LER (lm/W)
1% Dy 2% Sm doped ZnO nanofibers	0.3592	0.4423	68	4857	289
2% Dy 2% Sm doped ZnO nanofibers	0.4389	0.3811	68	2771	241
3% Dy 2% Sm doped ZnO nanofibers	0.2135	0.1963	NA	NA	115

2.4 Conclusions

Dy–Sm co-doped ZnO nanofibers with diameters in the range 100–180 nm have been fabricated successfully by electrospinning. Photoluminescence spectra clearly depicts the energy transfer mechanism within the host ZnO and dopants Sm and Dy wherein CIE parameter confirms the colour tunabilty of co-doped ZnO nanofibers. Enhanced visible light luminescence transverse from warm orange white region to cool blue white region is observed in CIE diagram with increasing dopant Dy concentrations. Thus, it could be clearly stated that the colour tunability can be achieved by varying the dopant concentrations and variety of dopants. Such materials can be a very good optimum candidate for colour tunable luminescent light emitting fabrics.

Acknowledgements This work is supported by the Department of Science and Technology (DST, New Delhi, India) Support under DST-FIST Program, Grant No. SR/FST/PSI-178/2012(C).

References

1. W. Ge, J. Shi, M. Xu, X. Chen, J. Zhu, Red upconversion luminescence (UCL) properties in one-dimensional Yb2Ti2O7: Er nanofibers via an electrospinning route. J. Alloy Comp. **788**, 993–999 (2019)
2. Y. Zhang, C. Zhang, Y. Feng, T. Zhang, Q. Chen, Q. Chi, L. Liu, G. Li, Y. Cui, X. Wang, Z. Dang, Q. Lei, Excellent energy storage performance and thermal property of polymer-based composite induced by multifunctional one-dimensional nanofibers oriented in-plane direction. Nano Energy **56**, 138–150 (2018)
3. Q. Chen, Q. Wang, X. Wu, T. Wang, Y. Tang, Z. Duan, D. Sun, X. Zhao, F. Wang, W. Shi, Piezoelectric/photoluminescence effect in one-dimensional lead-free nanofibers. Scr. Mater **145**, 81–84 (2018)
4. Q. Liu, J. Zhu, L. Zhang, Y. Qiu, Recent advances in energy materials by electrospinning. Renew. Sustain. Energy Review. **81**, 1825–1858 (2018)
5. L. Zhang, S. Gbewonyo, A. Aboagye, A. Kelkar, Development of carbon nanofibers from electrospinning, in *Nanotube Superfiber Materials*, chap. 33 (2019), pp. 867–878, 2019
6. N. Wang, X. Mao, S. Zhang, J. Yu, B. Ding, Electrospun nanofibers for air filtration, in *Electrospun Nanofibers for Energy and Environmental Applications*, chap. 12 (Springer, Berlin, 2014), pp. 299–324
7. J. Sheng, J. Zhao, X. Yu, L. Liu, J. Yu, B. Ding, Electrospun nanofibers for waterproof and breathable clothing, in *Electrospinning: Nanofabrication and Application*, chap. 17 (Elsevier, 2019), pp. 543–570
8. G. Yang, X. Li, Y. He, J. Ma, G. Ni, S. Zhou, From nano to micro to macro: electrospun hierarchically structured polymeric fibers for biomedical applications. Prog. Polym. Sci. **81**, 80–113 (2018)
9. J. Yang, F. He, H. Wu, Y. Liang, Y. Wang, Z. Sun, Engineering surface and optical properties of TiO2-coated electrospun pvdf nanofibers via controllable self-assembly. Nanomaterials **8**, 741 (2018)
10. R. Alwan, Q. Kadhim, K. Sahan, R. Ali, R. Mahdi, N. Kassim, A. Jassim, Synthesis of zinc oxide nanoparticles via sol-gel route and their characterization. Nanosci. Nanotechnol. **5**(1), 1–6 (2015)
11. M. Kahouli, A. Barhoumi, A. Bouzid, A. Al-Hajry, S. Guermazi, Structural and optical properties of ZnO nanoparticles prepared by direct precipitation method. Superlattices Microstruct. **85**, 7–23 (2015)
12. L. Radjehi, A. Djelloul, S. Lamri, M. Slim, M. Rahim, Oxygen effect on structural and optical properties of zinc oxide. Surf. Eng. 1–7 (2018)
13. Z. Zhang, X. Shi, H. Lou, X. Cheng, Y. Xu, J. Zhang, Y. Li, L. Wang, H. Peng, A one-dimensional soft and color-programmable light-emitting device. J. Mater. Chem. C **6**(1328), 2018 (2018)
14. J. Sowik, M. Miodyńska, B. Bajorowicz, A. Mikołajczyk, W. Lisowski, T. Klimczuk, D. Kaczor, A. Medynska, A. Malankowska, Optical and photocatalytic properties of rare earth metal-modified ZnO quantum dots. Appl. Surf. Sci. (2018)
15. R. Martínez, C. Zuluaga, S. Dussan, H. Huhtinen, W. Wojciech, R. Palai, Influence of rare-earth substitution on the structural magnetic, optical and dielectric properties of ZnO nanoparticles. MRS Adv. (2019)
16. Y. Fang, J. Lang, J. Wang, Q. Han, Z. Zhang, Q. Zhang, J. Yang, S. Xing, Rare-earth doping engineering in nanostructured ZnO: a new type of eco-friendly photocatalyst with enhanced photocatalytic characteristics. Appl. Phys. A **124**, 605 (2018)
17. J. Wu, B. Cao, L. Rino, Y. Fang, L. Hu, Z. Zhang, Y. Huang, B. Dong, Strong up-conversion luminescence of rare-earth doped oxide films enhanced by gap modes on ZnO nanowires. Nanoscale **10**(2), 726–732 (2017)
18. A. Abdellah, A. Hafez, S. Panikkanvalappil, M. El-Sayed, N. Allam, Single-crystal electrospun plasmonic perovskite nanofibers. J. Phys. Chem. C **122**, 6846–6851 (2018)

19. Y. Ding, J. Liu, Y. Zhu, S. Nie, W. Wang, J. Shi, Y. Miu, Brightly luminescent and color-tunable CaMoO4:RE3+(RE 5 Eu, Sm, Dy, Tb) nanofibers synthesized through (RE 5 Eu, Sm, Dy, Tb) nanofibers synthesized through(RE 5 Eu, Sm, Dy, Tb) nanofibers synthesized through a facile route for efficient LED's. J. Mater. Sci. **53**, 4861–4873 (2018)
20. W.L. Zhang, Y. Feng, Blueshift of absorption edge and photoluminescence in Al doped ZnO thin films. Integr. Ferroelectr. **188**, 112–120 (2018)
21. U. Manzoor, M. Islam, L. Tabassam, S. Rahman, Quantum confinement effect in ZnO nanoparticles synthesized by co-precipitate method. Phys. E **41**, 1669–1672 (2009)
22. N. Kumar, A. Srivastava, Enhancement in NBE emission and optical band gap by Al doping in nanocrystalline ZnO thin films. Opto-Electron. Rev. **26**, 1–10 (2018)
23. A. Kumar Srivastava, J. Kumar, Band gap narrowing in zinc oxide-based semiconductor thin films. J. Appl. Phys. **115**, 134904 (2014)
24. K. Saw, N. Aznan, F. Yam, S. Pung, New insights on the Burstein-Moss shift and band gap narrowing in Indium-Doped zinc oxide thin films. PLoS ONE **10**(10), e0141180 (2015)
25. T. Ivanova, A. Harizanova, T. Koutzarova, B. Vertruyen, Study of ZnO sol-gel films: effect of annealing. Mater. Lett. **64**, 1147–1149 (2010)
26. M. Kamalasanan, S. Chandra, Sol-gel synthesis of ZnO thin films. Thin Solid Films **288**, 112–115 (1996)
27. H. Noei, H. Qiu, Y. Wang, E. Loffler, C. Woll, M. Muhler, The identification of hydroxyl groups on ZnO nanoparticles by infrared spectroscopy. Phys. Chem. Chem. Phys. **10**, 7092–9097 (2008)
28. R. Helbig, E. Tomzig, Band edge emission in ZnO. J. Lumin **14**, 403–415 (1976)
29. M. Seshadri, M. Radha, D. Rajesh, L. Barbosa, C. Cordeiro, Y. Ratnakarama, Effect of ZnO on spectroscopic properties of Sm3+ doped zinc phosphateglasses. Phys. B **59**, 79–87 (2015)
30. C. Manjunatha, D. Sunitha, H. Nagabhushan, B. Nagabhushana, S. Sharmad, Combustion synthesis, structural characterization, thermo and photoluminescence studies of CdSiO3:Dy3+ nanophosphor. Spectrochim. Acta Part A **93**, 140–148 (2012)
31. D. Wang, Q. Yin, Y. Li, M. Wang, Concentration quenching of Eu2+ in SrO:Al2O3:Eu2+ phosphor. J. Lumin. **97**, 1–6 (2002)
32. S. Itankar, M. Dandekar, S. Kondawar, B. Bahirwar, Eu3+-doped polystyrene and polyvinylidene fluoride nanofibers made by electrospinning for photoluminescent fabric designing. Luminescence **32**, 1535–1540 (2017)

Chapter 3
Electromagnetic Interference Shielding Effectiveness of Graphene Based Conducting Polymer Nanocomposites

Prerna R. Modak, Deoram V. Nandanwar and Subhash B. Kondawar

Abstract Carbon-based conducting polymer nanocomposites were found to be an excellent electromagnetic interference (EMI) shielding materials. In the present work, initially the graphene was functionalized by acid treatment to attach carboxylic functional groups on the surface of the graphene to facilitate the interaction with conducting polymer. Polyaniline (PANI)/Graphene (GNS) and polypyrrole (PPy)/Graphene (GNS) nanocomposites were synthesized by in situ chemical oxidative polymerization and characterized by SEM, FTIR and UV-VIS analyses. The electrical conductivity of nanocomposites was found to be drastically increased as compared to that of pure conducting polymer. Further, the conductivity of nanocomposites was also found to be increased with the increase in weight % of GNS. Nanocomposites showed semiconducting nature as that of pure conducting polymer with improved dielectric properties and EMI shielding effectiveness. The EMI shielding effectiveness (SE) of nanocomposites was found to be increased with increasing GNS content. The dominant mechanism of EMI shielding for both PANI/GNS and PPy/GNS nanocomposites is absorption and thus, the nanocomposites can be used as EMI shielding materials to protect electronic devices and components from electromagnetic radiation. The comparative study infers that the shielding effectiveness of PPy/GNS nanaocomposites is less than that of PANI/GNS nanocomposites.

P. R. Modak
Department of Physics, Rashtrapita Mahatma Gandhi Arts, Commerce and Science College, Saoli, Chandrapur, India

D. V. Nandanwar
Department of Physics, Mohata College of Science, Nagpur, India

S. B. Kondawar (✉)
Department of Physics, Rashtrasant Tukadoji Maharaj Nagpur University, Nagpur, India
e-mail: sbkondawar@yahoo.co.in

R.-I. Murakami et al. (eds.), *NAC 2019*, Springer Proceedings in Physics 242,
https://doi.org/10.1007/978-981-15-2294-9_3

3.1 Introduction

Electromagnetic Interference (EMI) is the form of pollution that exist due rapid development of the digital and communication technology which can cause problems from minor static noise, signal degradation to major health effects [1]. EMI shielding materials are used to protect sensitive workspaces, environments, human health and circuits from EM radiation from telecommunication devices. Metals are good for EMI shielding, they are expensive, heavy and prone to corrosion, poor to chemical resistance, oxidation, difficult in processing and high cost of manufacturing processes [2]. Various carbon-based materials with different structures, as well as their composites, including carbon black (CB), carbon nanofibers (CNFs), carbon nanotubes (CNTs) and graphene (GNS), have attracted attention as EMI shielding or absorbing materials because of their variable morphology, light weight, adjustable porosity, high conductivity, resistance to corrosion, and ease of processing. Among all the carbon based materials GNS is promising in handling terahertz frequency signals and thus can be used for electromagnetic interference shielding material [3]. Electrically conducting polymers (CPs) are the candidates suitable for several applications due to their extraordinary properties such as electrical characteristics, reversible doping and dedoping procedure, controllable chemical and electrochemical properties and simple processibility. Polyaniline (PANI) and Polypyrrole (PPy) are the most promising CPs among all [4]. Polyaniline not only reflects but also absorbs electromagnetic waves and can attain high level of shielding performance [5]. Similarly, polypyrrole (PPy), is one of the conducting polymers which has attracted a great deal of interest because of its good electrical conductivity, environmental stability, porous nature and easy synthesis. PPy has been used in various applications, such as batteries, supercapacitors, sensors, and microwave shielding and corrosion protection. These composites offer potentials in EMI shields, electronic packaging, display devices and electrodes [6, 7]. Polymer composites based on nanosized fillers have unique combination of electrical, thermal, dielectric and mechanical properties. They represent a class of materials for the suppression of this electromagnetic pollution [8]. To resolve the problem of EMI various composites were tried by the researchers. Yan et al. prepared porous graphene/polystyrene composites, the composite shows 64.4 dB specific shielding effectiveness, which is the highest value ever reported for polymer based EMI shielding materials at such a low thickness of 2.5 mm [9]. Tung et al. fabricated the hybrid materials of Fe_3O_4-decorated reduced graphene oxide (Fe_3O_4-RGO) and poly (3, 4-ethylenedioxythiophene) (PEDOT) by poly (ionic liquid)-mediated hybridization. These hybrid materials of Fe_3O_4-RGO with PEDOT showed the lowest surface resistivity of 80 Ωsq^{-1} at an RGO-Fe_3O_4 loading of 1 wt%, and exhibited super paramagnetic behavior with an electromagnetic interference shielding effectiveness of 22 dB [10]. Zhang et al. prepared the composite of graphene in microcellular polymer foam which shows the electromagnetic shielding effectiveness 15–19 dB at 10 GHz [11]. Chen et al. and his co-worker fabricated polyaniline composites filled with graphene, graphene decorated with silver nanoparticles (Ag/graphene), and graphene decorated with nickel nanoparticles

(Ni/graphene) and EMI shielding effectiveness (EMI SE) of the composites with different filler loadings (0.5, 1.0, 3.0, and 5.0 wt%) were investigated. The PANI composite containing 5.0 wt% graphene decorated with silver showed the best electrical conductivity of 20.32 S/cm and highest EMI SE of 29.33 dB [12]. Sabira et al., observed remarkably high electromagnetic interference (EMI) shielding effectiveness of about 47 dB, exhibited by highly conducting and ordered poly(vinylidene fluoride) (PVDF)/graphene nanocomposite films of thickness around 20 μm, in the microwave frequency range 8–12 GHz, obtained by solution casting method [13]. Sambyal et al. and his coworker synthesize conducting polymer based composite encapsulated with Barium strontium titanate (BST), reduced graphene oxide (RGO), and Fe_3O_4 nanoparticles via chemical oxidative polymerization method of pyrrole.

The presence of filler materials in conducting polymer matrix leads to absorption dominated shielding effectiveness value of 48 dB in the frequency range of 8.2–12.4 GHz in X-band [14]. Zhang et al. prepared in situ from thermosetting polybenzoxazine (PBZ) and trichlorophenylsilane modified graphene (GS) 20 wt% of GS, and the corresponding nanocomposites showed the highest shielding effectiveness (SE) of 40.9 dB for 20 wt% of GS over the range of X-band [15]. But very few works have been reported on microwave absorption in Ku-band. In the present work, the PANI/GNS and PPy/GNS were synthesized by in situ chemical polymerization to study the dielectric properties and EMI Shielding effectiveness in Ku-Band.

3.2 Experimental

3.2.1 Materials

Aniline, pyrrole, ammonium persulfate, sulphuric acid and nitric acid were procured from Merck Ltd., India. Graphite flakes were made available from National Physical Laboratory, New Delhi (India). All chemicals were of AR grade and used as received except aniline which was distilled under reduced pressure and kept below 4 °C before used for synthesis. Deionised water was used in all synthesis.

3.2.2 Synthesis of PANI/GNS and PPy/GNS Nanocomposites

Graphite oxide (GO) was synthesized from natural purified graphite flakes by the Hummers method, and graphene nanosheets (GNS) were prepared by exfoliation of GO [16, 17]. GNS was functionalized by acid treatment to obtain a surface suitable for making chemical interaction with polymers [18, 19]. The synthesis of PANI/GNS nanocomposites were synthesized by in situ chemical oxidative polymerization method by varying the concentration of functionalized Graphene (1, 3 and

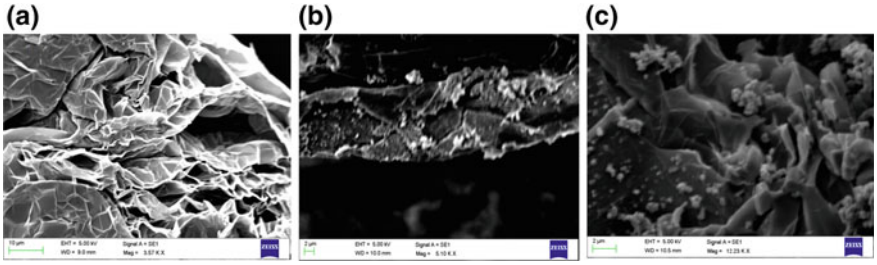

Fig. 3.1 SEM images of **a** functionalized graphene, **b** PANI/5%GNS and **c** PPy/5%GNS

5%) were conducted as per our previously reported work [20]. Similarly, by changing the weight percentage of functionalized graphene from 1, 3 and 5%, PPy/GNS were synthesized by in situ chemical oxidative polymerization method. The complete synthesis process is reported earlier [21].

3.3 Results and Discussion

3.3.1 Morphology

SEM images were recorded on Carl Zeiss EVO-18 scanning electron microscope. The functionalized graphene exhibits a shiny, black appearance with a metallic lustre confirms the successful exfoliation of graphene from GO (Fig. 3.1a). SEM image of PANI/5%GNS revealed that the surfaces of the GNS are coated with the layer of PANI (Fig. 3.1b). PPy/5%GNS shows highly porous with the layer of PPy on the surface of GNS are clearly seen in Fig. 3.1c.

3.3.2 UV-VIS Spectroscopy

In the present work UV 240 Shimadzu automatic double beam spectrophotometer was used to record the UV-Visible spectra. UV-Visible spectra indicates that both the composites absorbs the maximum radiation in the UV-Visible range and thus can be directly applied as the UV shielding materials. In PANI/GNS nanocomposite (Fig. 3.2a) the two clear peaks at 320 and 550 nm in UV-Vis spectrum is observed similar to that of PANI. The spectrum shows a weaker absorption peak at around 300 nm and a broad absorption at around 600 nm. The weak absorption band is due to π-π^* transition and broad absorption band is due to quinoid ring transition in the chain of polyaniline [22]. The broad peaks at 440 and 750 nm in PPy/GNS nanocomposites is due to the extended PPy chains indicating a well conjugation, hence high degree of doping and conductivity for the nanocomposites PPy/GNS confirm the

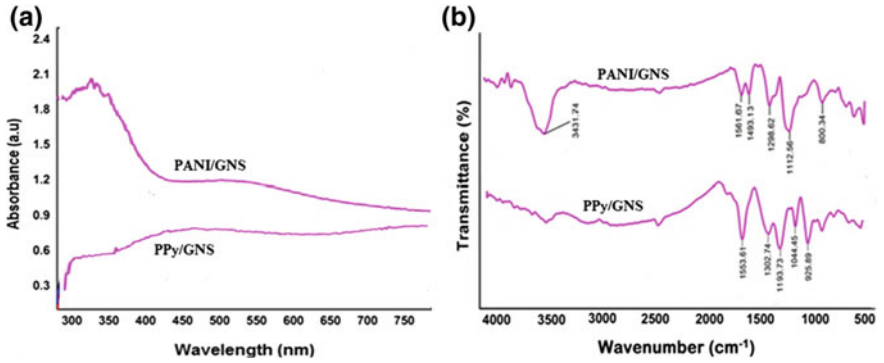

Fig. 3.2 **a** UV-Visible Spectra and **b** FTIR spectra of PANI/5%GNS and PPY/5%GNS

interaction between GNS sheets and PPy spheres. The optical absorption in conjugated polymers is mostly amorphous or semicrystalline may be due to transition of charge carriers, through a forbidden energy gap [23].

3.3.3 FTIR Spectroscopy

FTIR spectra were recorded by KBr pellet technique in the wavelength range 400–4000 cm^{-1} by Thermo Nicolet, Avatar 370. Fourier transforms infrared spectra for PANI/GNS and PPy/GNS nanocomposite is shown in Fig. 3.2b. A significant peak at 1107.41 cm^{-1} (C-N stretching) for PANI was found due to the charge delocalization over the polymeric backbone. In the FTIR of the PPy/GNS nanocomposites it is possible to recognize characteristic peaks of polypyrrole at 1544.22, 1297.56 cm^{-1} [24]. The GNS peaks are slightly specific in the nanocomposite materials because of its low concentration in PPy [24].

3.3.4 Electrical Conductivity

The electrical conductivity was measured by four probe method. The samples were prepared as round shaped pellets at room temperature. The conductivity of the PANI/GNS and PPy/GNS composites for three different weight fractions is depicted in Fig. 3.3. The percolation threshold is defined as the point where adding a small amount of conductive filler dramatically increases the composite electrical conductivity. For PANI/ GNS composite, percolation threshold occurred at 3 wt% of GNS. Since PPy is an insulating material, it is almost transparent to electromagnetic waves, far below the percolation threshold; for 1 wt% of GNS fillers, the conductivity is still

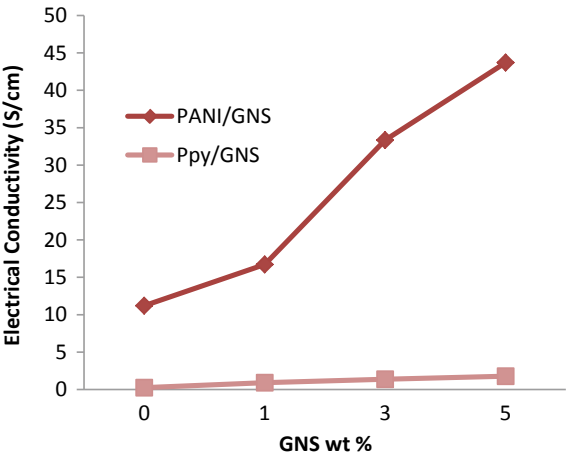

Fig. 3.3 Electrical conductivity with respect to GNS %

almost zero like conductivity of an insulating PPy matrix. The electrical conductivity of PANI/ GNS composites as well as the PPy/GNS composites increased with the increased in weight percent of GNS in PANI and PPy matrix. The remarkable enhancement of electrical conductivity potentially endows PANI/ GNS and PPy/GNS with good electromagnetic interference (EMI) shielding property.

3.3.5 Permittivity

Electromagnetic interference shielding and dielectric constant with dielectric loss measurements were carried out on vector network analyzer in the microwave range of 12.4–18 GHz (Ku band) using Agilent Technologies, E8362B. Figure 3.4a, b shows that dielectric constant (ε') and dielectric loss (ε'') values exhibit decreasing trend with frequency. Due to the decreasing ability of the dipoles to maintain the in-phase movement with rapidly pulsating electric vector of the incident EM wave. The results also revealed that the dielectric constant (ε') as well as dielectric loss (ε'') values of the composite exhibit noticeable enhancement after addition of filler (GNS) nanoparticles. As the concentration of graphene in conducting polymer increases, the permittivity of the composites also increases. This is due to the increase in the motion of free charge carriers and space charge builds up because of interfacial polarization. The real and imaginary permittivity in PANI/GNS nanocomposite increase explicitly as the concentration of graphene increases from 0 to 5 wt%. For higher concentration of graphene in the nanocomposite, the permittivity is almost independent of frequency whereas for 1 and 3% of GNS it decreases with frequency. But in case of PPy/GNS at lower concentration permittivity is independent of frequency. For higher concentration the permittivity decreases with increase in frequency. The resonance peak is observed in dielectric constant and dielectric loss at 15.76 GHz when the

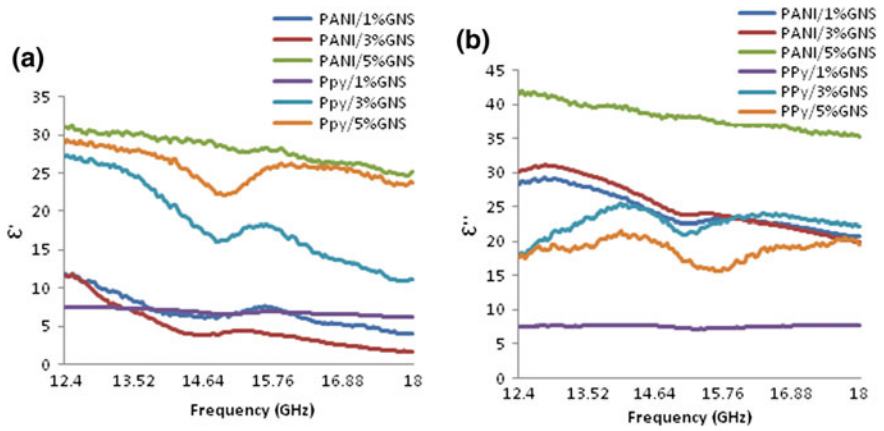

Fig. 3.4 **a** Dielectric constant and **b** dielectric loss of PANI/GNS and PPy/GNS

hopping frequency of electrons becomes equal to the applied field frequency, where a maximum electrical energy is transferred to the oscillating ions and power loss shoots up, thereby resulting resonance.

3.3.6 Electromagnetic Interference (EMI) Shielding

Electromagnetic Interference Shielding refers to the reflection and absorption of electromagnetic radiation by the shielding material. Other than reflection and absorption one more mechanism of shielding is multiple reflections, which is nothing but the number of reflection at different surfaces in shielding material [25]. The Electromagnetic interference shielding effectiveness is defined as the logarithmic ratio of incoming power input to outgoing power of radiation. The efficiency of any shielding material is expressed in decibels (dB). Higher the decibel level of electromagnetic interference shielding effectiveness, lesser will be the energy transmitted through shielding material [12]. The shielding effectiveness of a shielding material is equal to the sum of absorption factor, the reflection factor and the multiple reflection [26, 27]. Total SE depends on the propagation direction of the incident wave, composite thickness, frequency, and polarization type. Skin depth is an very important parameter for considering the material for microwave shielding application. At high frequencies, the EM radiations penetrate only near the surface area of a conductor. SE_R, SE_A and SE_T of the PANI/GNS and PPy/GNS nanocomposites as a function of frequency are shown in Fig. 3.5. PANI/GNS and PPy/GNS nanocomposites show excellent microwave absorption properties.

EMI SE_R was found to be nearly linear in the entire frequency range of measurement with negligible change with the increase in GNS loading. SE_A is increased from 20 to 30 dB with increase in GNS loading from 1 to 3 wt%. The experimental

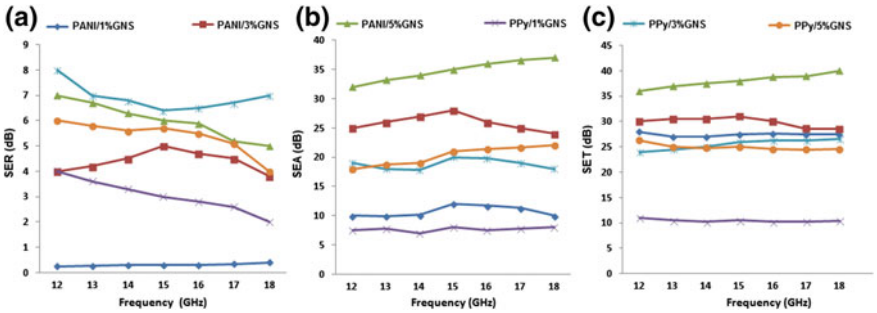

Fig. 3.5 EMI SE_R, SE_A, SE_T for PANI/GNS and PPy/GNS

results show that absorption is the primary shielding mechanism and reflection is the secondary shielding mechanism. SE_T of nanocomposites as a function of frequency shows that, the nature of SE_T for each composition is nearly linear with frequency, but the SE_T of composite is found to increase with the increase in GNS loading. EMI SE_T of PANI/GNS for 1, 3, and 5 wt% GNS loading was found to be 28, 30, and 40 dB, respectively. EMI SE_T of PPy/GNS was found to be 11, 24 and 26 dB for 1, 3, and 5 wt% GNS loading respectively. EMI SE_R, SE_A and SE_T of the PANI/GNS composite are higher than those of the PPy/GNS composite in the range 12–18 GHz, but the absorption share of the PANI/GNS composite is higher than that of the PPy/GNS composites. Both the composites PANI/GNS and PPy/GNS show high value of EMI SE.

3.4 Conclusion

PANI/GNS and PPy/GNS nanocomposites were successfully synthesized. Microscopic and spectroscopic characterizations confirm the addition of GNS filler into conducting polymers. The electrical conductivity, dielectric constant and dielectric loss measurements approves the consideration of composites for EMI shielding. In both the composites PANI/GNS and PPy/GNS high value of EMI SE is obtained for the synthesized composites which show higher SE than the required value of EMI shielding effectiveness (20 dB) for commercial applications. It was found to be absorption dominated indicating PANI/GNS and PPy/GNS nanocomposites can be used as lightweight EMI shielding materials. But among the PANI/GNS and PPy/GNS nanocomposites, PANI/GNS nanocomposites show better EMI Shielding Effectiveness in Ku band.

Acknowledgements This work is supported by the Department of Science and Technology (DST, New Delhi, India) Support under DST-FIST Program, Grant No. SR/FST/PSI-178/2012(C).

References

1. H. Zahari, H. Guan, M. Cheng, F. Mansor, H. Rahim, Electromagnetic interference (EMI) shielding performance of the ternary composite based on $BaFe_{12}O_{19}$, MWCNT and PANI at the Ku-Band. Prog Electromagnet. Res. **52**, 111–118 (2016)
2. V. Eswaraiah, V. Sankaranarayanan, S. Ramaprabhu, Functionalized graphene–PVDF foam composites for EMI shielding. Macromol. Mater. Eng. **296**, 894–899 (2011)
3. J. Wang, H. Zhou, J. Zhuang, Q. Liu, Influence of spatial configurations on electromagnetic interference shielding of ordered mesoporous carbon/ordered mesoporous silica/silica composites. Sci. Rep. **3**, 3252 (2013)
4. R. Kumar, S. Singh, B. Yadav, Conducting polymers: synthesis, properties and applications. Int. Adv. Res. J. Sci. Eng. Technol. **2**, 110–124 (2015)
5. T. Ting, K. Wu, Synthesis and electromagnetic wave-absorbing properties of batio3/polyaniline structured composites in 2–40 Ghz. J. Polym. Res. **20**, 127–132 (2013)
6. D. Ateh, H. Navsaria, P. Vadgama, Polypyrrole-based conducting polymers and interactions with biological tissues. J. Roy. Soc. Interface **3**(41), 741–752 (2006)
7. H. Abdulla, A. Abbo, Optical and electrical properties of thin films of polyaniline and polypyrrole. Int. J. Electrochem. Sci. **7**, 10666–10678 (2012)
8. N. Joseph, C. Janardhanan, M. Sebastian, Electromagnetic interference shielding properties of butyl rubber-single walled carbon nanotube composites. Compos. Sci. Technol. **101**, 139–144 (2014)
9. D. Yan, P. Ren, H. Pang, Q. Fu, M. Yang, Z. Li, Efficient electromagnetic interference shielding of lightweight graphene/polystyrene composite. J. Mater. Chem. **22**, 18772–18774 (2012)
10. T. Tung, J. Feller, T. Kim, H. Kim, W. Yang, K. Suh, Electromagnetic properties of Fe_3O_4-functionalized graphene and its composites with a conducting polymer. J. Polym. Sci. **50**, 927–935 (2012)
11. H. Zhang, Q. Yan, W. Zheng, Z. He, Z. Yu, Tough, graphene polymer microcellular foams for electromagnetic interference shielding. ACS Appl. Mater. Interfaces **3**, 918–924 (2011)
12. Y. Chen, Y. Li, M. Yip, Electromagnetic interference with metallic nanoparticles. Compos. Sci. Technol. **80**, 80–86 (2013)
13. K. Sabira, M. Jayakrishnan, P. Saheeda, S. Jayalekshmi, On the absorption dominated EMI shielding effects in free standing and flexible films of poly(vinylidene fluoride)/graphene nanocomposite. Eur. Polym. J. **99**, 437–444 (2018)
14. P. Sambyal, S. Dhawan, P. Gairola, S. Chauhan, S. Gairola, Synergistic effect of polypyrrole/BST/RGO/Fe_3O_4 composite for enhanced microwave absorption and EMI shielding in X-Band. Curr. Appl. Phys. **18**, 611–618 (2018)
15. S. Zhang, S. Yin, Q. Ran, Q. Fu, Y. Gu, Facile preparation of polybenzoxazine/graphene nanocomposites for electromagnetic interference shielding. Polymer **162**, 20–28 (2019)
16. T. Chen, J. Qui, K. Zhu, Y. Che, Y. Zhang, J. Zhang, H. Li, F. Wang, Z. Wang, Enhanced electromagnetic wave absorption properties of polyanilline-coated Fe3O4/reduced grapheme oxide nanocomposites. J. Mater. Sci. Mater. Electron. **25**, 3661–3673 (2014)
17. F. Hanifah, J. Jaarfar, M. Aziz, A. Ismail, H. Othman, M. Rahman, Effect of reduction time on the structural, electrical and thermal properties of synthesized reduced graphene oxide nanosheets. Bull. Mater. Sci. **38**, 1569–1576 (2015)
18. N. Cordero, J. Alonso, The interaction of sulphuric acid with graphene and formation of adsorbed crystals. Nanotechnology **18**, 485705 (2007)
19. C. Bautista-Flores, R. Sato-Berrú, D. Mendoza, Doping graphene by chemical treatments using acid and basic substances. J. Mater. Sci. Chem. Eng. **3**, 17–21 (2015)
20. P. Modak, S. Kondawar, D. Nandanwar, Synthesis and characterization of conducting polyaniline/graphene nanocomposites for electromagnetic interference shielding. Procedia Mater. Sci. **10**, 588–594 (2015)
21. P. Modak, D. Nandanwar, S. Kondawar, Conducting polypyrrole/graphene nanocomposites as potential electromagnetic interference shielding materials in the Ku-band. J. Phys. Sci. **27**, 137–157 (2016)

22. O. Ansari, M. Khan, S. Ansari, I. Amal, J. Lee, M. Cho, PTSA doped conducting graphene/polyaniline nanocomposite fibers: Thermoelectric behaviour and electrode analysis. Chem. Eng. J. **242**, 155–161 (2014)
23. J. Zheng, X. Ma, X. He, M. Gao, G. Li, C. Harish, Praparation, characterizations, and its potential applications of PANi/ graphene oxide nanocomposite. Procedia Eng. **27**, 1478–1487 (2012)
24. H. Oliveira, S. Sydlik, T. Swager, Supercapacitors from free-standing polypyrrole/graphene nanocomposites. J. Phys. Chem. **117**, 10270–10276 (2013)
25. T. Gupta, B. Singh, R. Mathur, S. Dhakate, Multi-walled carbon nanotube–graphene–polyaniline multiphase nanocomposite with superior electromagnetic shielding effectiveness. Nanoscale Royal Soc. Chem. **6**, 842–851 (2014)
26. H. Al-Saleh, U. Sundararaj, Electromagnetic interference shielding mechanisms of CNT/polymer composites. Carbon **47**, 1738–1746 (2009)
27. O. Nakhaei, N. Shahtahmassebi, R. Roknabadi, M. Behdani, Synthesis, UV-shielding and electromagnetic wave absorbing properties of polyvinylpyrrolidone-TiO_2/polyacrylonitrile-SiO_2 nanofibre nanocomposites. Bull. Mater. Sci. **42**, 1–8 (2019)

Chapter 4
Phase Separated Structures of Mixed Carrageenan Gels Elucidated Using Particle Tracking

Lester C. Geonzon and Shingo Matsukawa

Abstract The phase separated structure of mixed κ-(KC) and ι-(IC) carrageenan gels were elucidated using dynamic rheological measurements and particle tracking for probe particles with diameter of 100 nm. Particle tracking was utilized to investigate the gelation mechanism and network structure of the mixed gels during cooling at 1 and 0.005 °C/min and after 1 day storage at 5 °C. The mean square displacement (MSD) of particles in the mixed gels was used to characterize the changes in the microscopic physical property of the gels. The individual MSD of particles in the mixed gel after 1 day storage showed a large distribution indicating a microstructural heterogeneity which proposed the formation of phase separated structure with KC-rich and IC-rich network domains. Interestingly, a significant splitting in the individual MSD was observed using 0.005 /min cooling rate suggesting an enhanced phase separated structure.

4.1 Introduction

Carrageenans are sulfated galactans commonly extracted from different species of red seaweeds, made up of alternating disaccharide repeating units of 3-linked-β-D-galactopyranose (G units) and 4-linked-α-D-galactopyranose (D units) [1]. The most commonly utilized carrageenans are the κ-(KC), ι-(IC) and λ-(LC) carrageenan which differs in the amount of sulfate groups: one (G4S-DA) for KC, two (G4S-DA2S) for IC, and three (G2S-D2S,6S) for LC [1]. Between the three mentioned carrageenan, KC and IC displayed gelling behavior influenced by temperature and presence of cations e.g. K^+, Ca^{2+}, while LC is known to be a non-gelling carrageenan.

In industry, carrageenans are widely used in foods as thickening, gelling and stabilizing agents and in cosmetics and pharmaceutical formulations as pigment dispersion and drug encapsulation materials. In addition to pure carrageenans, carrageenans have been also used as mixtures for better controllability of the physical property

L. C. Geonzon · S. Matsukawa (✉)
Department of Food Science and Technology, Tokyo University of Marine Science and Technology, 4-5-7 Konan, Minato-Ku, Tokyo 108-8477, Japan
e-mail: matsukaw@kaiyodai.ac.jp

R.-I. Murakami et al. (eds.), *NAC 2019*, Springer Proceedings in Physics 242,
https://doi.org/10.1007/978-981-15-2294-9_4

and texture enhancement of the final product *i.e*. food product such as dairy dessert, processed meat, milk based drink, etc. Due to the usefulness in industry, mixtures of carrageenan have been studied over the past decades using different techniques from macro- to microscopic aspects, such as rheological measurements [2–4], thermal measurements using differential scanning calorimetry (DSC) [2, 3] and nuclear magnetic resonance (NMR) [5]. Rheological and thermal measurements revealed the independent aggregation of KC and IC chains in the mixed carrageenan gels which suggests the possible formation of a phase separated network structure. Diffusion measurements of probe polymers were carried out to clarify the structure, but could not conclude the phase separated structure due to the short diffusion time and size of probe polymer [5]. Consequently, the network structure in the mixed carrageenan gels remains unclear with no direct evidence of the phase separated structure.

In this article, studies on the phase separated network structure in the mixed carrageenan gels using a particle tracking technique are presented. The particle tracking measurements of probe particles in the mixed gels prepared at different cooling rates after 1 day storage at 5 °C were performed and the results were compared with rheological measurements to elucidate the network structure in the mixed gels.

4.2 Experimental Procedures

4.2.1 Sample Preparation

Sodium-type κ- and ι-carrageenan powder (Tokyo Chemical Industry Co., Ltd. Tokyo, Japan) were dialyzed against NaCl solution and subsequently against deionized water to obtain Na^+ type carrageenan solutions. Samples for the particle tracking experiments were prepared as described in references [6, 7] by adding fluorescent labeled particles with a size of 0.1 μm (Green, Thermo Scientific). The mixed solution of KC and IC was prepared by mixing pure KC and IC solutions at 50:50 mixing ratio (KC50IC50). Samples for the rheological measurements were prepared using the same procedure except for the addition of probe particles.

4.2.2 Rheological Measurement

Rheological properties were measured using HAAKE MARS II rheometer (Thermo Scientific, Waltham, MA, USA) equipped with blasted parallel-plates (diameter 35 mm) with 1 mm gap. Hot sample solutions were loaded on preheated plates at 80 °C and covered with oil to avoid water evaporation. The storage modulus (G') and loss modulus (G'') were monitored on cooling from 80 to 5 °C at a rate of 1 °C/min with a frequency of 1 Hz and at strain of 1%.

4.2.3 Particle Tracking Measurements

Particle tracking measurements of fluorescent particles embedded in the carrageenan solutions were carried out using an inverted microscope, BZ-9000 (Keyence Corp., Osaka, Japan), equipped with a PlanFluor 100 × NA 1.30 oil-immersion objective (Nikon Corp. Inc., Japan) and a temperature-controlled microscope stage (ALA Scientific Instruments Inc., New York). Samples were placed in a custom-made sample chamber equipped with temperature sensor for actual sample temperature monitoring as described in references [6, 7].

Particle movements were recorded using a built-in 2/3-in., 1.5 megapixels, 12-bit, monochrome cooled CCD camera (Keyence Corp., Osaka, Japan) at a rate of 7.5 frames per second for 110 s. The position of each fluorescent labeled particle was determined by a program employing an algorithm which improves the accuracy of particle position using the image-intensity weighted centroid for each particle [8]. The time-averaged MSD for each particle (*msd*) obtained from *N* images representing a total diffusion time τ was calculated with the following equation [9, 10]

$$msd(\tau) = \frac{1}{N - \tau/\Delta t} \sum_{i=1}^{N-\tau/\Delta t} [r(i\Delta t + \tau) - r(i\Delta t)]^2 \tag{4.1}$$

where Δt is the interval time for each frame, that is the inverse of the frame rate, and r(Δt) is the position of the centroids of each tracked particle. The exponent α in the relationship between *msd* and τ, $msd \sim \tau^{\alpha}$, was calculated for each particle at lag times in the range 1–20 s. Because the number of displacements for the averaging ($N - \tau/\Delta t$) decreases, the *msd* points at longer lag times tend to have larger statistical fluctuations [11]. The ensemble-averaged MSD $\langle msd \rangle$ was obtained by averaging the *msd* of all tracked particles. Particle tracking and MSD calculations were performed using a custom-made program written in Mathematica 10 (Wolfram Research, Inc., Champaign, IL) [8].

4.3 Results and Discussion

4.3.1 Dynamic Rheological Properties

The temperature dependence of viscoelastic property of 1.5% carrageenan solution with 10 mM KCl was measured on cooling. Figure 4.1 presents the evolution of G' against the temperature on cooling. The point with a sharp increase in G' for each solution was defined as the critical temperature (T_c) at which the polysaccharide chains transform into helices and form aggregates to yield a three-dimensional network. The mixed KC and IC solution showed a two-step increase in G' close to the T_c observed in pure IC ($T_{c,IC} \sim 35$ °C) and KC ($T_{c,KC} \sim 23$ °C), consistent with the

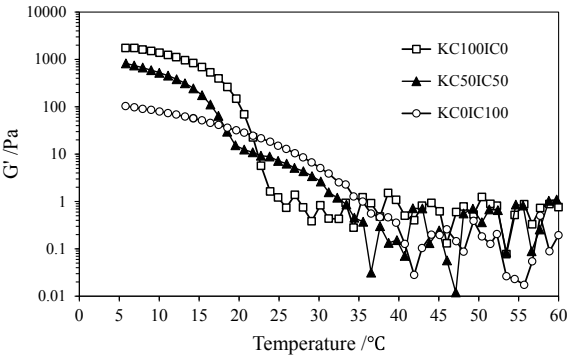

Fig. 4.1 Temperature dependence of G′ for 1.5% carrageenan in 10 mM KCl on cooling. Reproduced with permission from Geonzon et al. [6]. Copyright 2019, The Electrochemical Society

previous studies [2–4]. The two-step increase in G' observed in KC50IC50 suggests the independent aggregation of KC and IC chains in the mixed solutions on cooling [2–4]. This demonstrated the possibility that KC50IC50 formed a phase separated structure made of KC-rich and IC-rich network domains.

4.3.2 Particle Tracking on Cooling

The results in rheological measurements suggest the phase separated structure of the mixed carrageenan gels. However, the consideration was based on the macroscopic observation with no information on the microscopic structures. The particle tracking for sub-micron particles provides information on the microscopic physical property of the media to add with the macroscopic rheological property. Figure 4.2 presents the temperature dependence of $\langle msd \rangle$ at $\tau = 10$ s ($\langle msd(10\text{ s}) \rangle$) for the particles in 1.5% carrageenan solutions with 10 mM KCl. Particles in pure IC showed the highest $\langle msd(10\text{ s}) \rangle$ with a weak decrease around $T_{c,IC}$ suggesting the gradual formation of IC chain aggregates [5]. Meanwhile, the particles in pure KC showed

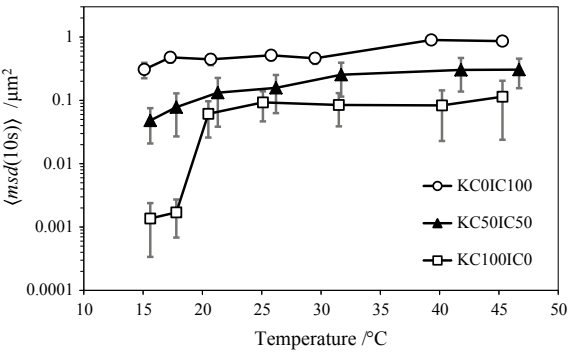

Fig. 4.2 Temperature dependence of $\langle msd(10\text{ s}) \rangle$ for particle with size of 0.1 μm in 1.5% carrageenan solutions in 10 mM KCl on cooling. Reproduced with permission from Geonzon et al. [6]. Copyright 2019, The Electrochemical Society

the lowest $\langle msd(10\ \mathrm{s})\rangle$ with a steep decrease at $T_{c,KC}$ showing the fast development of network formation of KC chain aggregates. The difference in the $\langle msd(10\ \mathrm{s})\rangle$ of particles in pure carrageenan gels was highly associated to the difference in the microscopic physical property between pure KC which forms a hard and brittle gel and IC which forms a soft and so-called "weak" gel described in reference [7]. Furthermore, the $\langle msd(10\ \mathrm{s})\rangle$ of particles in KC50IC50 showed an intermediate behavior and demonstrated a two-step decrease around $T_{c,IC}$ and $T_{c,KC}$. The two-step decrease in $\langle msd(10\ \mathrm{s})\rangle$ was consistent with the two-step increase in G' observed in the rheological measurements. The first decrease around $T_{c,IC}$ was attributed to the formation of IC chain aggregates which obstructs particle mobility while the second decrease around $T_{c,KC}$ was attributed to the formation of KC chain aggregates.

4.3.3 *Effect of 1 Day Storage on the Network Structure View by Particle Tracking*

The change in the network structure of the carrageenan gels were investigated after 1 day storage at 5 °C after cooling at 1 °C/min. Figure 4.3a–c present the *msd* of particles in (a) KC, (b) KC50IC50 and (c) IC. The particles in pure IC gels showed a diffusive behavior with the *msd* increasing with lag time τ while the particles in pure KC gels demonstrated a trapped behavior indicating the network formation

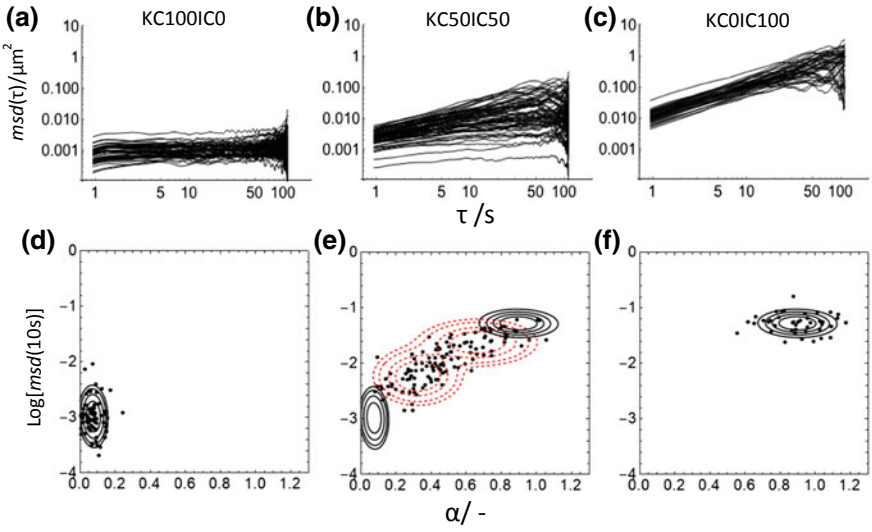

Fig. 4.3 (Top row) *msd* of particle with size of 0.1 μm in **a** KC, **b** KC50IC50 and **c** (IC) after 1 day storage at 5 °C using a cooling rate of 1 °C/min. (Bottom row) Distribution of $msd(10\ \mathrm{s})$ and α of individual particles for **d** KC, **e** KC50IC50 and **f** (IC). Reproduced with permission from Geonzon et al. [6]. Copyright 2019, The Electrochemical Society

of KC chain aggregates. Meanwhile, the particles in KC50IC50 presented a broad distribution of *msd* indicating the particles in the mixed carrageenan gels exist in different microenvironments due to the developed structural heterogeneity.

The observed heterogeneity in particle diffusivity in the KC50IC50 was attributed to the possible formation of phase separated structure made of KC-rich and IC-rich network domains [6]. The degree of heterogeneity in the mixed gels was characterized by plotting *msd* at $\tau = 10$ s *msd*(10 s) and the exponent α for individual particles. The *msd*(10 s) corresponds to the local viscosity at $\tau = 10$ s and α describes the type of particle diffusion where $\alpha = 1$ implies the free diffusion of particles while $\alpha = 0$ indicates the restricted diffusion of particles, i.e. trapped in the network. When α lies between 0 and 1, sub-diffusive behavior is considered. Figure 4.3d–f presents the plot of *msd*(10 s) against α for (d) KC, (e) KC50IC50 and (f) IC. The plots of pure KC and IC gels showed a unimodal bivariate Gaussian distribution indicated by the solid black lines suggesting the particles in pure gels probe the same microenvironment. There is a noticeable difference in the distribution between pure KC (with $\alpha \sim 0$ and low *msd*) and IC (with $\alpha \sim 1$ and high *msd*) indicating the difference in the microscopic physical properties between the pure gels. In addition, the diffusive behavior of particles observed in pure IC suggests that IC gels formed clusters of IC chain aggregates that are not connected with each other, which allows particle diffusion associated with the structure of a weak gel [7].

The plot of *msd*(10 s) and α for particles in KC50IC50 spread broadly in between pure KC and IC. Based on the considerations that the mixtures formed the phase separated structure and *msd*(10 s) and α are independent with each other, a bimodal bivariate Gaussian function with no correlation parameter between *msd*(10 s) and α was used to fit the data by the red dashed lines as shown in Fig. 4.3e. The observed bimodal bivariate distribution in KC50IC50 implies the presence of two groups of particles with restricted and diffusive mobility due to the formation of phase separated structures [6]. The restricted and diffusive particles were attributed to be in KC-rich and IC-rich domains, respectively. It is also worth noting that the particles in KC-rich domain exhibited higher mobility than in pure KC while the particles in IC-rich domain demonstrated slower mobility than in pure IC. This probably corresponds to the presence of non-negligible amount of other carrageenan chains in both domains. It was also proposed that the observed heterogeneity in KC50IC50 was on the way to the phase separated structure, however, frozen due to the aggregation of KC and IC chains at the cooling rate (1 °C/min) employed in this experiment.

4.3.4 Effect of Cooling Rate on the Network Structure View by Particle Tracking

The phase separated structure of mixed carrageenan gels was further investigated by varying the cooling rate [7]. Figure 4.4a presents the *msd* of particles in KC50IC50 using 0.055 °C/min cooling rate. A considerable splitting in the *msd* was observed

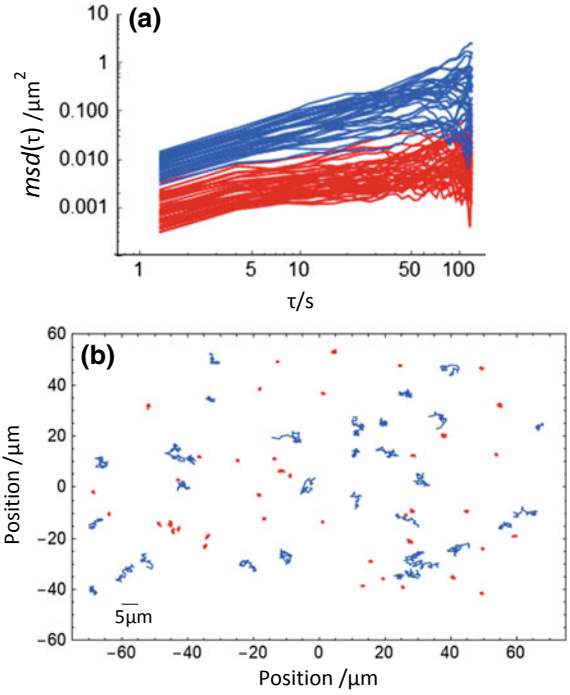

Fig. 4.4 **a** *msd* for particles with size of 0.1 μm in mixed KC50IC50 solutions with a cooling rate of 0.005 /min. The red and blue lines represent the restricted and diffusive particles. **b** Trajectory of individual particles in the mixture after grouping. The trajectories were magnified × 5 for clarity

suggesting a possibility of an enhanced phase separated structure made of KC-rich and IC-rich domains which were grouped into two populations using a clustering method in Mathematica 10 based on the plot of *msd*(10 s) and α. The red and blue lines in Fig. 4.4a represent the restricted and diffusive particles, respectively. The trajectories of individual particles in each group were plotted in red and blue in Fig. 4.4b. The restricted and diffusive particles showed a non-localization indicating that the particles were not migrated. Therefore, the domain size of phase separated structure was estimated to be larger than the particle size of 0.1 μm and smaller than the space of particles which is around 10 μm.

4.4 Conclusion

The phase separated structure in mixed KC and IC gels were investigated using rheological measurements and particle tracking. Dynamic rheological measurements suggest an independent aggregation of KC and IC chains in the mixture. Particle tracking of individual particles in the mixture after 1 day storage demonstrated a broad distribution of *msd* suggesting a high degree of heterogeneity which was associated to the formation of phase separated structure made of KC-rich and IC-rich network domain and frozen due to the aggregation of KC and IC chains to form

the network. Meanwhile, the *msd* of particles at 0.005 °C/min cooling rate showed a significant splitting indicating the enhanced phase separated structure in the mixed gel.

Acknowledgements The authors thank Prof. Toru Suzuki for a fruitful discussion about the results by fluorescence microscopy. This work was supported by JSPS KAKENHI Grant Number JP18H00962.

References

1. A. Usov, Sulfated polysaccharides of the red seaweeds. Food Hydrocolloids **6**(1), 9–23 (1992)
2. L. Du, T. Brenner, J. Xie, S. Matsukawa, A study on phase separation behavior in kappa/iota carrageenan mixtures by micro DSC, rheological measurements and simulating water and cations migration between phases. Food Hydrocolloids **55**, 81–88 (2016)
3. L. Du, T. Brenner, J. Xie, Z. Liu, S. Wang, S. Matsukawa, Gelation of iota/kappa carrageenan mixtures, in *Gums and Stabilisers for the Food Industry 18: Hydrocolloid Functionality for Affordable and Sustainable Global Food Solutions* (The Royal Society of Chemistry, 2016), pp. 47–55
4. T. Brenner, R. Tuvikene, A. Parker, S. Matsukawa, K. Nishinari, Food Hydrocolloids Rheology and structure of mixed kappa-carrageenan/iota-carrageenan gels. Food Hydrocolloids **39**, 272–279 (2014)
5. B. Hu, L. Du, S. Matsukawa, NMR study on the network structure of a mixed gel of kappa and iota carrageenans. Carbohyd. Polym. **150**, 57–64 (2016)
6. L. Geonzon, R. Bacabac, S. Matsukawa, Microscopic characterization of phase separation in mixed carrageenan gels using particle tracking. J. Electrochem. Soc. **166**(9), B3228–B3234 (2019)
7. L. Geonzon, R. Bacabac, S. Matsukawa, Network structure and gelation mechanism of kappa and iota carrageenan elucidated by multiple particle tracking. Food Hydrocolloids **92**, 173–180 (2019)
8. L. Geonzon, S. Matsukawa, Accuracy improvement of centroid coordinates and particle identification in particle tracking technique. J. Biorheology **33**(1), 2–7 (2019)
9. O. Lieleg, I. Vladescu, K. Ribbeck, Characterization of particle translocation through mucin hydrogels. Biophys. J. **98**, 1782–1789 (2010)
10. E.C. Wagner, S.B. Turner, M. Rubinstein, E.H. McKinley, K. Ribbeck, A rheological study of the association and dynamics of MUC5AC gels. Biomacromolecules **18**(11), 3654–3664 (2017)
11. X. Michalet, Mean square displacement analysis of single-particle trajectories with localization error: Brownian motion in isotropic medium. Phys. Rev. E: Stat., Nonlin, Soft Matter Phys. **82**(4 Pt 1), 041914 (2010)

Part II
Recycle Composites

Chapter 5
Synthesis of Na-P Zeolite from Geothermal Sludge

D. F. Fitriyana, Hazwani Suhaimi, Sulardjaka, R. Noferi and Wahyu Caesarendra

Abstract Geothermal waste from PT. Geo Dipa Energy Dieng was transformed to Na-P zeolite (CFA-ZP) experimentally at a low temperature (100 °C) via conventional hydrothermal. This study was conducted to determine the effect of the hydrothermal process holding time on the characterization of Na-P zeolite. Synthesis process via hydrothermal method was performed with different holding times of 10, 15 and 20 h at a constant temperature of 100 °C. The synthesized material were characterized using XRD and SEM techniques. The results showed conventional hydrothermal process successfully converts geothermal waste into Na-P zeolite, zeolite A and sodalite. Increasing the holding time in conventional hydrothermal method has affected the material characterization of the synthesized zeolite.

5.1 Introduction

Indonesia is geologically located at the confluence of three major tectonic plates; the Eurasian Plate, the Indo-Australian Plate and the Pacific Plate and this strategic geological condition makes a real contribution to the availability of geothermal energy

D. F. Fitriyana
Department of Mechanical Engineering, Semarang State University, Semarang 50229, Indonesia
e-mail: deniifa89@gmail.com

Sulardjaka · R. Noferi · W. Caesarendra
Department of Mechanical Engineering, Diponegoro University, Jl. Prof. Soedharto SH, Semarang 50275, Indonesia
e-mail: sulardjaka@gmail.com

R. Noferi
e-mail: naldorival@gmail.com

H. Suhaimi · W. Caesarendra (✉)
Faculty of Integrated Technologies, Universiti Brunei Darussalam, Jalan Tungku Link, Gadong BE1410, Brunei Darussalam
e-mail: wahyu.caesarendra@ubd.edu.bn

H. Suhaimi
e-mail: hazwani.suhaimi@ubd.edu.bn

R.-I. Murakami et al. (eds.), *NAC 2019*, Springer Proceedings in Physics 242,
https://doi.org/10.1007/978-981-15-2294-9_5

in Indonesia. However, in terms of geothermal energy development, Indonesia is still behind the United States and the Philippines which produces 3093 and 1904 MW of geothermal energy respectively, in comparison with Indonesia which produces a total of 1341 MW [1]. Geothermal energy is a renewable energy resource producing considerable amount of wastes in the form of geothermal brine and geothermal sludge. The geothermal sludge typically contains solids which precipitate out in the waste water treatment plant during the power generation process and the sludge can be highly concentrated in a variety of heavy metal salts namely iron, titanium, manganese, zinc, arsenic, boron, cadmium, lead, nickel and copper [2]. It also contains a large proportion of silica [2, 3]. Due to these, the geothermal waste cannot be directly disposed into a landfill without any prior treatments [3, 4].

Disposal of hazardous solid wastes at a geothermal power plant is a major concern where large amounts of geothermal sludge volumes are generated. Recent studies have shown that many countries were able to further refine the silica contained in the geothermal sludge into a saleable product. There is a variety of markets and possible uses for amorphous silica of which, depending on the form and purity, can be worth up to 15 US$/kg [5]. Silica is a chemical compound, also known as Silicon Dioxide and is most commonly found in nature as Quartz. It is used for a variety of applications such as an additive for structural materials, silicon for microelectronics, components in the food industry and pharmaceutical industry as well as a mineral for human intake, amongst others. Silica is a valuable product whose costs vary, depending on its properties. The desired properties are often the high surface area, large pore volume and a uniform pore size distribution. Some studies reported that the composition has less significance than the corresponding texture for most applications [6]. Zeolites are microporous crystalline aluminosilicates, composed of TO tetrahedra (T = Si, Al) with O atoms connecting neighboring tetrahedral [7]. There are two kinds of zeolite; natural zeolite and synthesized zeolite. The synthetic zeolites have been used commercially than natural zeolites due to its purity of crystalline products and the uniformity of its particle size. The main advantages of synthetic zeolites in comparison to naturally-occurring zeolites are that they can be engineered with a wide variety of chemical properties and different pore sizes and that they have greater thermal stability. The zeolite synthesis involves the hydrothermal crystallization of aluminosilicate gels [8].

The major drawback of zeolite synthesis is the availability and the cost of the raw material, specifically the silica source. The usage of silica contained in the geothermal waste as a starting material for zeolite synthesis does not only help to reduce its cost production but also contributes to the mitigation of environmental problems [9]. Many studies have used geothermal wastes as a silica source in zeolite synthesis. Zeolite A and hydroxysodalite (HS) were successfully synthesized from a geothermal sludge [3, 10]. Zeolite Na-P was also synthesized from coal fly ash, kaolin waste, clinoptilolite, paper sludge ash and coal bottom ash [11–16]. Zeolite A and zeolite X were successfully synthesized from silica in rice husk [17, 18]. The types and characteristics of zeolites produced from the synthesis processes are influenced by reaction time, temperature, pressure and synthesis conditions [3].

Previous experiments reported that geothermal waste contains silica and alumina: 81.26 and 0.14% (calcinated at a temperature of 850 °C for 3 h). The novelty of this study is to synthesize Na-P zeolite from geothermal wastes via hydrothermal reaction. Na-P zeolite is one of the most interesting synthesized zeolites because of its high cation exchange and adsorption capacity. This synthetic zeolite can be used in different applications such as gas separation application; removal of heavy metal, ammonium, toxic and radioactive waste species; extraction of potassium from sea water; water-softening; and as a builder and water-softening agent for eco-friendly detergent [19].

5.2 Experimental Procedures

The geothermal waste was obtained from Geo Dipa geothermal power plant, Dieng, Indonesia. The geothermal waste was dried under sunlight for a period of time until it was completely dried and screened with a mesh 100 to obtain the geothermal powder. The geothermal powder was calcined at 850 °C for 3 h. This process aimed to drive off volatile expunges, moisture, water of hydrates, organic matter and increase the yield of SiO_2 from the geothermal powder. The chemical compositions of geothermal powder before and after calcinations were characterized by atomic absorption spectroscopy (AAS). Calcined geothermal powder was used as a silica source in the synthesis of zeolite and was prepared through conventional hydrothermal method.

The precursor for zeolite synthesis process was carried out by reacting 30 mL of sodium silicate solution and 30 mL of sodium aluminate solution using a magnetic stirrer with 200 rpm for 2 h at room temperature. This process produced natrium aluminosilicate. Sodium silicate was made from 3 g of geothermal powder mixed with 30 mL of NaOH 3M, and then stirred at a temperature of 1000 °C for 20 min. Sodium aluminate was made from 8.5 g of $Al(OH)_3$ mixed with 100 mL of NaOH 5M [20]. The precursor was poured into a Teflon autoclave and hydrothermal reaction was conducted on a conventional hydrothermal reactor at a temperature of 100 °C for 10, 15, and 20 h. The synthesized products were washed with distilled water and filtered with a Whatman 42 paper to separate filtrate from solid. The solid was dried in the oven at a temperature of 80 °C for 4 h to obtain the final product. The final products were examined by X-ray powder diffraction (XRD) for amorphicity and crystalline analysis. Crystalline phases present in the samples were identified with the help of Joint Committee on Powder Diffraction Standards (JCPDS). The morphological structures of the synthesized products were obtained and analysed using Scanning Electron Micrograph (SEM).

5.3 Results and Discussions

In this study, Atomic Absorption Spectrophotometer (AAS) is used to characterize the chemical constituents of geothermal powder. The potential application of atomic absorption principle is necessary to determine metallic constituents of silicate materials. The analysis of raw geothermal powder is presented in Table 5.1.

XRD plays an important role in the qualitative and quantitative characterization of synthesized products. Data obtained in the form of the intensity and angle 2θ were then matched with the XRD pattern JCPDS in order to identify the crystal phases present in the sample [10, 20]. An effective method to determine the phase of the grown samples is by comparing the XRD data with standard database of JCPDS. As presented in Fig. 5.1, some similarities were observed with respect to the diffractogram from JCPDS data number 11-0401 (hydroxy-sodalite), 40-1464 (zeolite Na-P) and 31-1269 (Zeolite A). This result shows that the synthesized products contain crystals of Zeolite A, zeolite Na-P and hydroxy-sodalite. It is also observed that the XRD peaks at 24.7663, 24.1773 and 43.2287 indicates that the synthesized product contains sodalite. The presence of zeolite A is indicated with the XRD peaks

Table 5.1 Elemental analysis (in % wt) of the raw materials

No	Oxide	Uncalcined geothermal powder	Calcined geothermal powder
1	Al_2O_3	0.0559	0.1421
2	Fe_2O_3	0.1919	0.4506
3	Na_2O	0.6088	0.7601
4	SiO_2	49.100	80.0426
5	Others	50.0433	18.6040

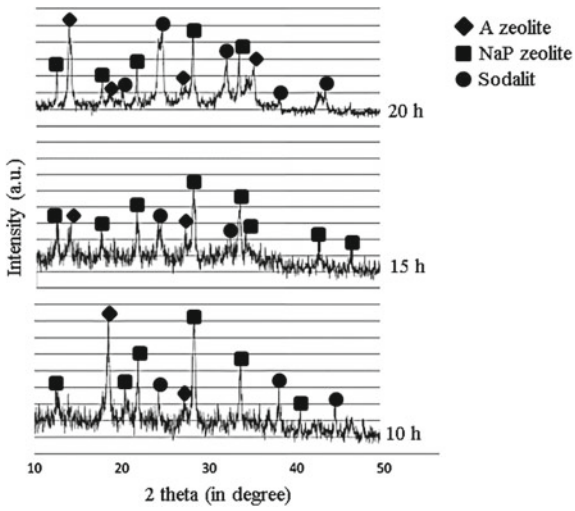

Fig. 5.1 XRD patterns of hydrothermal product of geothermal waste at different holding times of 10, 15 and 20 h

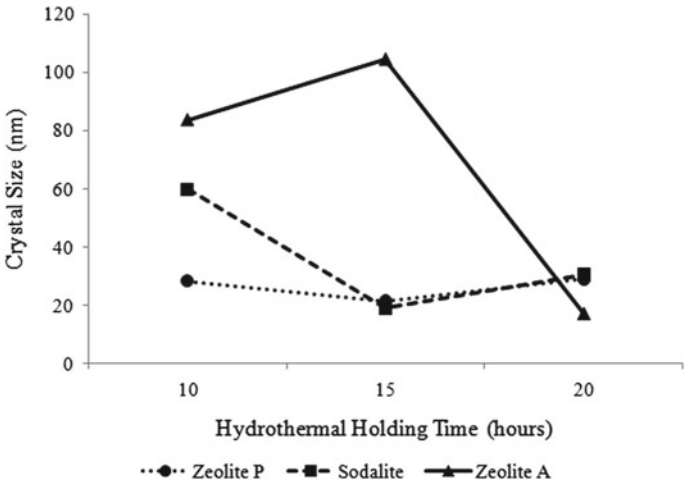

Fig. 5.2 Crystal size of zeolite Na-P, zeolite A and hydroxy-sodalite at different holding times of 10, 15 and 20 h

at 13.8076, 13.4088 and 13.9422 while the presence of zeolite Na-P is observed with the XRD peaks at 28.2511, 28.0813 and 28.3809.

The crystal size was determined using the Scherer formula based on the XRD characterization of synthesized products [10, 21]. The crystal size of zeolite synthesized from geothermal waste at variations of hydrothermal holding time are shown in Fig. 5.2.

The respective crystal size of zeolite Na-P at holding time variations of 10, 15 and 20 h were 28.5, 21.4 and 29.2 nm while the crystal size of zeolite A at holding time variations of 10 h, 15 h and 20 h were 83.6 nm, 104.4 nm and 17.1 nm, respectively. The crystal size of sodalite at holding time variations of 10 h, 15 h and 20 h were 59.7 nm, 18.9 nm and 30.4 nm, respectively. It was also observed that the hydrothermal holding time affects the crystal size of zeolite A, zeolite Na-P and sodalite formed. By increasing the hydrothermal holding time from 10 to 15 h increases the crystal size of zeolite A. The same phenomenon was discovered in the crystal size of zeolite Na-P and sodalite by increasing the hydrothermal holding time from 15 to 20 h. The results from this study indicate that the crystal size of zeolite Na-P, zeolite A and sodalite increases significantly with increasing hydrothermal holding time. Similar results were reported by Muhammad et al. and Zou et al. that increasing the reaction time resulted in an increase in the average particle size [22, 23]. As reported by Liang et al. the duration of the hydrothermal reaction affected the size and morphology of nanoapatite crystals due to larger crystal growth with prolonged reaction times. Prolonging the hydrothermal treatment time promotes solvent evaporation and maintains the solution in a supersaturation state, thereby assisting crystal growth [24].

On the other hand, increasing the hydrothermal holding time beyond 15 h resulted in a decrease in the crystal size of zeolite A. The same phenomenon was discovered

Table 5.2 The effect of crystallization time on synthesised zeolites

Hydrothermal holding time (h)	Total relative intensity (zeolite phase)		
	Zeolite A	Na-P Zeolite	Sodalite
10	6	100	4
15	8	100	46
20	100	17	86

in the crystal size of zeolite Na-P and sodalite where it decreased with an increase of holding time from 10 to 15 h. Increasing the crystallization time results in dissolved synthesized zeolites in the alkaline solution and this causes a decrease in its crystallinity and crystal size [21]. This observation agrees with the work of Hanipa et al. which reported the longer the crystallization time the slower the crystal growth rate and nucleation rate and thus producing a small crystal size [25].

The crystallization time beyond 15 h for zeolite Na-P could decrease the intensity for zeolite Na-P and increase the intensity for sodalite and zeolite A, which is consistent with the XRD results as shown Fig. 5.1. Figure 5.1 illustrates the crystallinity which increased with extending times at 100 °C. It started to decrease beyond 20 h due to collapsed of zeolite framework. As can be seen in Fig. 5.2, the optimum crystallinity of zeolite Na-P in 15 h hydrothermal holding time was characterized by the smallest crystal size [26, 27]. Table 5.2 summarizes the effects of crystallization time on XRD patterns of the prepared zeolite samples. It is observed that the synthesized zeolite tends to have higher crystallinity with flat baseline and no amorphous was formed in comparison to the provided JCPDS data base.

The result of this study is also in accordance with the result reported by Alrubaye and Zou et al. [23, 26]. In general, Ostwald's law of successive reactions is followed in zeolite synthesis, i.e., a metastable phase appears first and then successively more stable phases are then replaced. For instance, with prolonged crystallization time, zeolite-A (LTA) is dissolved to form zeolite-sodalite (SOD), when synthesized in an alkaline aluminosilicate-gel [21].

The photographs show the morphology of the zeolites formed where Fig. 5.3a shows SEM micrographs of zeolite Na-P (scale bar, 2 μm) while Fig. 5.3b shows SEM micrographs of zeolite A (scale bar, 8 μm). Figure 5.3c shows SEM micrographs of sodalite (scale bar, 2 μm). As evident from Fig. 5.3a–c, zeolite Na-P is identified by pseudo-spherical forms constituted by small plates, which formed polycrystals, zeolite A particles formed cubic shapes and sodalite particles presented spherical shapes with an obvious array of long fibers [10, 20, 23].

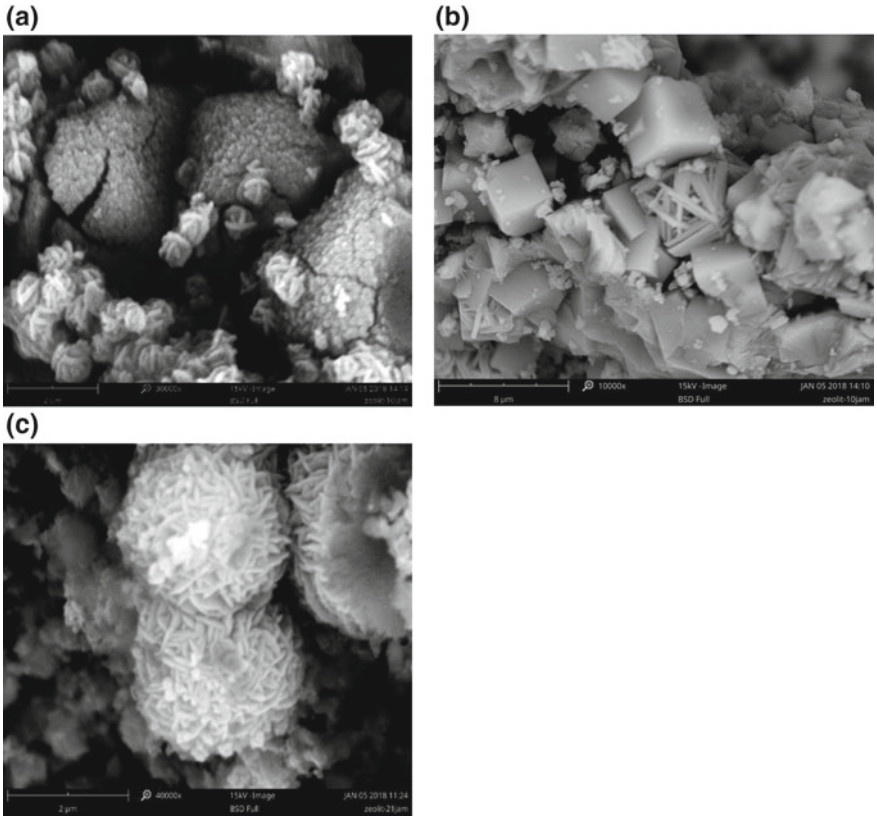

Fig. 5.3 SEM micrographs of **a** Zeolite Na-P at ×30000 magnification, **b** zeolite A at ×10000 Magnification and **c** sodalite at ×40000 magnification

5.4 Conclusions

Zeolite Na-P, zeolite A and sodalite have been successfully synthesized from geothermal wastes using silica as the source via the conventional hydrothermal method with holding time variations of 10, 15 and 20 h. The effects of hydrothermal holding time (hydrothermal duration) in the synthesis of possible zeolites on the crystalline end products were investigated. The results of this study showed that increasing the hydrothermal holding time from 10 to 15 h increases the crystal size of zeolite A and reduces the crystal size of zeolite Na-P and sodalite. However, increasing the hydrothermal holding time from 15 to 20 h reduces the size of zeolite A crystals but increases the size of Na-P and sodalite zeolite crystals.

Acknowledgements The first Author gratefully acknowledge the Faculty of Engineering Diponegoro University for funding this research which made this work possible (strategic research scheme, 2017).

References

1. P. Suharmanto, A.N. Fitria, S. Ghaliyah, in *Indonesian geothermal energy potential as source of alternative energy power plant*. Renewable Energy and Energy Conversion Conference and Exhibition (2015), pp. 119–124
2. D. Gallup, F. Sugiaman, V. Capunoc, A. Manceaud, Laboratory investigation of silica removal from geothermal brines to control silica scaling and produce usable silicates. Appl. Geochem. **18**, 1597–1612 (2003)
3. D.F. Sulardjaka, Fitriyana, A.P. Adi, Synthesis of zeolite from geothermal waste. Appl. Mech. Mater. **660**, 157–161 (2014)
4. A.J. Karabelas, N. Andritsos, A. Mouza, M. Mitrakas, F. Vrouzi, K. Christanis, Characteristics of scales from the Milos geothermal plant. Geothermics **18**, 169–174 (1989)
5. J.O. Were, in *Aspects of Waste Management and Pollution Control*. Olkaria Geothermal Field, Kenya, Geothermal Training Programme (1998), pp. 16–54
6. A. Hauksdóttir, Geothermal Energy: Silica Precipitation and Utilization. Thesis of the School of Science and Engineering at Reykjavík University, Iceland, 2016
7. P. Payra, P.K. Dutta, Zeolite: a primer, The Ohio State University, Columbus Ohio. U.S.A., in *Handbook of Zeolite Science And Technology*, ed. by Auerbach, M.C. Scott, A. Kathleen, P.K. Dutta (The Ohio State University Columbus Ohio, U.S.A., 2003)
8. D. Georgiev, B. Bogdanov, K. Angelova, I. Markovska, Y. Hristov, Synthetic zeolites—structure, classification, current trends in zeolite synthesis, (Review). Int. Sci. Conf., Stara Zagora **7**, 1–5 (2003)
9. I. Petrov, T. Michalev, *Synthesis of Zeolite A: A Review* (Scientific Work of The Russian University, 2012), pp. 30–35
10. A.P.A. Sulardjaka, S. Nugroho, in *Microwave-Hydrothermal Versus Conventional-Hydrothermal Synthesis of Zeolite A from Geothermal Waste*. 1st International Joint Conference on Advanced Engineering and Technology proceeding (2012). ISBN: 978-602-097-299-2
11. W. Chansiriwat, D. Tanangteerapong, K. Wantala, Synthesis of zeolite from coal fly ash by hydrothermal method without adding alumina and silica sources: effect of aging temperature and time. Sains Malays. **45**(11), 1723–1773 (2016)
12. M. Chigondo, U. Guyo, M. Shumba, F. Chigondo, B. Nyamunda, M. Moyo, T. Nharingo, Synthesis and characterisation of zeolites from coal fly ash (CFA). Synthesis **3**(4) (2013)
13. E.A. Hildebrando, C.G.B. Andrade, C.A.F.D. Rocha Junior, R.S. Angélica, F.R. Valenzuela-Diaz, R.D.F. Neves, Synthesis and characterization of zeolite NaP using kaolin waste as a source of silicon and aluminum. Mater. Res. **17**, 174–179 (2014)
14. J. Behin, H. Kazemian, S. Rohani, Sonochemical synthesis of zeolite NaP from clinoptilolite. Ultrason. Sonochem. **28**, 400–408 (2016)
15. P.W.D. Plessis, T.V. Ojumu, L.F. Petrik, Waste minimization protocols for the process of synthesizing zeolites from South African coal fly ash. Materials **6**(5), 1688–1703 (2013)
16. T. Wajima, M. Haga, K. Kuzawa, H. Ishimoto, O. Tamada, K. Ito, T. Nishiyama, R.T. Downs, J.F. Rakovan, Zeolite synthesis from paper sludge ash at low temperature (90 °C) with addition of diatomite. J. Hazard Mater. **132**(2), 244–252 (2006)
17. C. Bhavornthanayo, P. Rungrojchaipon, Synthesis of zeolite A membrane from rice husk ash. J. Met. Mater. Miner. **19**(2), 79–83 (2009)
18. D. Prasetyoko, Z. Ramli, S. Endud, H. Hamdan, B. Sulikowski, Conversion of rice husk ash to zeolite beta. Waste Manag. **26**, 1173–1179 (2006)
19. Z. Huo, X. Xu, Z. Lü, J. Song, M. He, Z. Li et al., Synthesis of zeolite Na-P with controllable morphologies. Microporous Mesoporous Mater. **158**, 137–140 (2012)
20. Sulardjaka, D.F. Fitriyana, The effect of concentration of NaOH and holding time on characteristic of zeolite sinthesized from geothermal waste. Reactor **17**(1), 17–24 (2017)
21. M. Mirfendereski, T. Mohammadi, in *Effects of Synthesis Parameters on the Characteristics of NaA Type Zeolite Nanoparticles*. Proceedings of the World Congress on Recent Advances in Nanotechnology (2016), pp. 1–8

22. S. Muhammad, I.M. Sofyana, A. Munandar, T.E. Agustina, E. Saputra, S. Wang, M.O. Tade, in *Hydrothermal Synthesis of Nanocrystalline Zeolite using Clear Solution*. Proceedings of The 5th Sriwijaya International Seminar on Energy and Environmental Science and Technology (2014), pp. 80–86
23. J. Zou, C. Guo, C. Wei, F. Li, Y. Jiang, Synthesis of pure Na-X and Na-P zeolite from acid-extracting residues of CFB fly ash by a single-step hydrothermal method. Mater. Trans. **57**(5), 726–731 (2016)
24. W. Liang, Y. Niu, S. Ge, S. Song, J. Su, Z. Luo, Effects of hydrothermal treatment on the properties of nanoapatite crystals. Int. J. Nanomedicine. **7**, 5151–5158 (2012)
25. P.H. Pardoyo, T. Arnelli, Y. Astuti, Effect of hydrothermal time variation on synthesis and characterization of zeolite A nanocrystal from rice husk ash. J. Sci. Appl. Chem. (2), 79–83 (2017)
26. R.T.A. Alrubaye, in *Influence Factors on Zeolite Y Crystal growth*. 1st International Conference on Recent Trends of Engineering Science and Sustainability (2017)
27. M. Farshid, H. Rouein, A. Sima, The synthesis of nano-sized ZSM-5 zeolite by dry gel conversion method and investigating the effects of experimental parameters by Taguchi experimental design. J. Exp. Nanosci. **13**(1), 160–173 (2018)

Chapter 6
Green Composites Based on Poly (Lactic Acid) and Bamboo Fiber: Flame Retardancy, Thermal, and Mechanical Properties

Yeng-Fong Shih and Zhong-Zhe Lai

Abstract A series of green composites composed of polylactic acid (PLA), bamboo fiber and halogen-free flame retardant (ammonium polyphosphate, APP) were prepared. Moreover, the APP was chemically modified with a silane coupling agent, 3-glycidoxypropyltrimethoxysilane to promote its compatibility with PLA. These green composites were prepared by melt-blending and its flame retardancy, thermal, and mechanical properties were investigated. The results reveal that the thermal degradation temperature and char yield of PLA were significantly elevated when modified APP was added. Furthermore, the storage and loss moduli of the composites can be enhanced effectively by the addition of bamboo fibers. This means that the addition of the bamboo fibers can reinforce both the rigidity and toughness of PLA. Moreover, scanning electron microscopy (SEM) analysis revealed that modified APP has better compatibility with PLA and bamboo fiber. According to the UL-94 analysis, the composite with modified APP and bamboo fiber can reach the highest retardant level V-0. These results indicate that modified APP can enhance the thermal resistance and flame retardant properties better than unmodified ones can. Moreover, the bamboo fibers can not only reinforce the mechanical properties of PLA, but also play an important role of synergistic flame retardancy with modified APP.

6.1 Introduction

Ammonium polyphosphate (APP) has attracted great attention because it is halogen-free and effective. The char produced protects underlying materials from heat and oxygen [1]. Recently, the development of biodegradable polymers has become a subject of great interest in materials science due to the environmental damage over the last few decades caused by plastic materials [2]. One of the biodegradable polymers is poly (lactic acid) (PLA), which is produced by a renewable source [3]. PLA is a

Y.-F. Shih (✉) · Z.-Z. Lai
Department of Applied Chemistry, Chaoyang University of Technology, No. 168, Jifeng E. Rd, Wufeng District, Taichung 41349, Taiwan
e-mail: syf@cyut.edu.tw

R.-I. Murakami et al. (eds.), *NAC 2019*, Springer Proceedings in Physics 242,
https://doi.org/10.1007/978-981-15-2294-9_6

thermoplastic, high-strength, high-modulus polymer and is easily processed using standard equipment to form molded parts, film or fibers [4]. However, the high brittleness and poor thermal stability of PLA currently limit its range of applications [5]. For wider applications of PLA, flame-retardant PLA composites have been widely studied [6–9]. In Shukor et al.'s study [10], PLA was blended with kenaf core fiber, polyethylene glycol and APP, respectively. It was found that APP was very effective in improving the flame-retardant properties with high limiting oxygen index (LOI) value and increased char residue at high temperatures. However, the compatibility between the PLA and kenaf fiber was poor, resulting in a significant reduction in the mechanical properties of the PLA composites.

Shaoa et al. [11] modified APP by ethylenediamine in order to reduce its hydrophilic property. It can be observed that when simply adding the unmodified APP into polypropylene (PP), the LOI of the composite is only increased from 18 to 20.9, and the flame retardant grade has no rating. This reveals that the addition of unmodified APP cannot achieve the flame retardant effect. After adding modified APP, the LOI of the composite increased from 18 to 32.5, and the flame retardant grade reached V-0, indicating that the modification of APP by ethylenediamine can not only reduce its hydrophilic property, but also improve the flame retardancy of the composite. Qin et al. [12] use vinyltrimethoxysilane (VTMS) to modify the surface of the APP. It can be observed that the flame retardancy of PP/dipentaerythritol (DPER)/APP composites has no rating. On the other hand, the flame retardancy of PP/DPER/modified APP composites can reach V-0 grade. It can be observed that the modification of APP is important in improving its flame retardant effect.

In this study, we incorporated bamboo fiber and flame retardant into PLA in order to prepare the flame retardant green composites with excellent mechanical and thermal properties. In addition, 3-glycidoxypropyltrimethoxysilane (GOPTS) was used to modify APP to improve its water resistance and enhance its interface compatibility with PLA. The flame retardancy, thermal, and mechanical properties of these green composites based on PLA and bamboo fiber were further investigated.

6.2 Experimental Procedures

6.2.1 Material

Polylactic acid (PLA) pellets (MW > 100,000) were purchased in 2003D grade from NatureWorks. The ammonium polyphosphate (APP) was provided by Parchem-fine & specialty chemicals. 3-glycidoxypropyltrimethoxysilane (GOPTS) was purchased from Echo Chemical.

6.2.2 Characterizations

Thermal behavior was determined using a TA Instruments' TGA Q50 thermogravimetric analyzer (TGA). A GT-HV 2000 analyzer was used to measure the heat deflection temperature (HDT) of the composites. Dynamic mechanical behaviors of the composites were measured by TA Instruments Q800. The UL-94 vertical tests were performed with an HVUL2 vertical burning tester (Atlas Technology Corp., Taiwan). A Hitachi scanning electron microscopy (SEM; model S-3000 N) was used to evaluate the morphologies and fractured surfaces of pure PLA and the composites.

6.2.3 Modification of APP

200 g APP, 4 g GOPTS and 200 mL ethanol were placed in a 500 mL three necked round-bottomed flask fitted with a stirrer and reflux condenser. The reaction was conducted for 1 h at 70 °C. The schematic diagram is shown as Fig. 6.1. Then the products were dried at 105 °C for 3 h in a vacuum oven.

6.2.4 Preparation of PLA Composite

The PLA, bamboo fiber, APP and modified APP had been dried in an oven at 100 °C for 4 h under reduced pressure until the moisture content was below 1.0 wt%. Immediately after drying, the PLA pellets were pre-melted at 175 °C in a counter-rotating internal mixer (Brabender PL2000, Duisburg, Germany) with a rotation speed of 50 rpm. Subsequently, the APP or modified APP were loaded into the mixer and blended with PLA for 5 min. Bamboo fiber was then further loaded into the mixer and blended with the mixture for another 10 min. Afterwards, the PLA composite was granulated. The sample was then processed by compression molding at 175 °C for 5 min (under 20 kgf/cm^2 or 50 kgf/cm^2), 3 min (under 75 kgf/cm^2) and 2 min (under 100 kgf/cm^2) in sequence. PLA contains 30% bamboo fiber named PF; PLA contains 20% APP named PA; PLA contains 30% bamboo fiber and 20% APP named PFA; PLA contains 20% modified APP named PEA; PLA contains 30% bamboo fiber and 20% modified APP named PFEA.

6.3 Results and Discussions

As can be seen from Table 6.1, whether or not a bamboo fiber is added, composites (PA and PFA) with unmodified APP, their 5 wt% degradation temperature (T_{d5}) and maximum degradation temperature (T_{dmax}) are all lower than those of composites

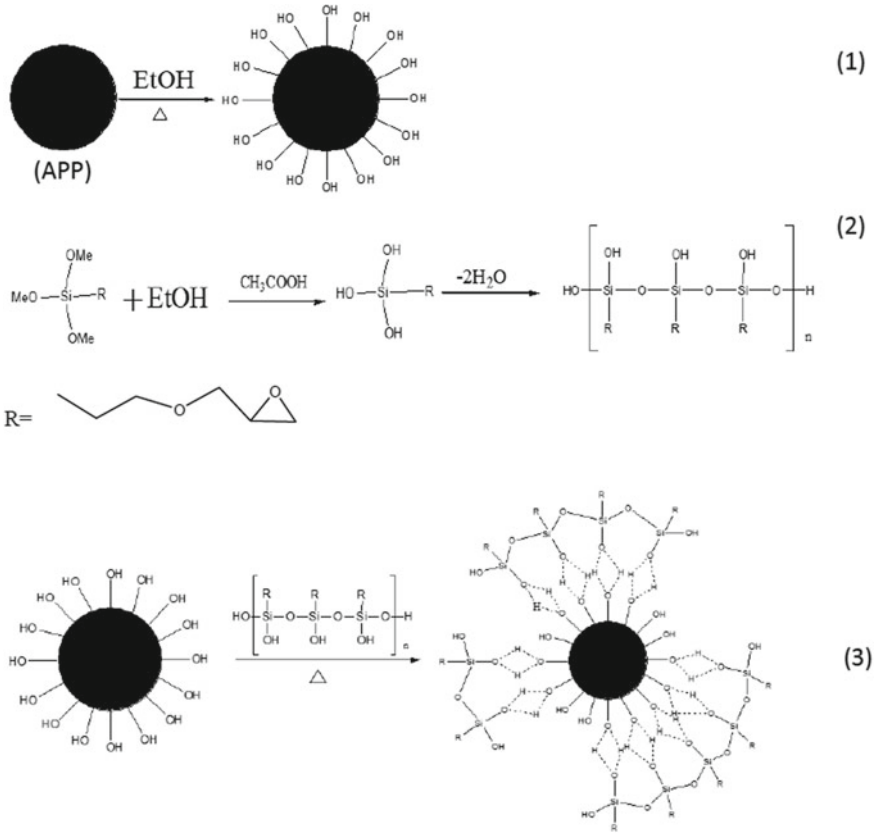

Fig. 6.1 Schematic diagram of APP modified by GOPTS

Table 6.1 TGA data of PLA and composites

Sample	T_{d5} (°C)	T_{dmax} (°C)	Char yield at 550 °C (%)
PLA	338.2	383.8	0.10
PF	308.2	364.1	7.60
PA	341.6	377.0	15.9
PFA	311.3	368.1	31.4
PEA	350.2	386.2	20.2
PFEA	311.7	371.5	30.8

(PEA and PFEA) with modified APP. Presumably, because the APP is modified by GOPTS, its surface layer is then coated with siloxane, and the siloxane also has the function of improving the heat resistance of the material, so the degradation temperature of the composites with modified APP is slightly improved. The 5 wt% and maximum degradation temperature (350.2 and 386.2 °C) of the composite containing

20% modified APP but no bamboo fiber (PEA) were the highest. However, in regard to the composites (PF, PFA and PFEA) containing bamboo fibers, the degradation temperature can be found to be lower because plant fibers usually begin to crack between 270 and 290 °C, resulting in an advance of the cracking temperature of the composites [13]. In addition, no matter whether adding APP or bamboo fiber, the char yield follows an increasing trend. Especially, the composite with the modified APP and bamboo fiber (PFEA) has the largest char yield of 30.8%, showing that the non-flammable ratio is effectively increased.

Table 6.2 shows the thermal deflection temperature (HDT) and dynamic mechanical properties of PLA and its composites. It can be observed that after simply adding APP or unmodified APP, the HDT is increased from 54.7 to 73.81 and 75.8 °C; after adding bamboo fiber, the HDT is significantly increased to 108.8 and 115.3 °C. This reveals that the rigidity and heat-resistant properties of the material can be effectively enhanced by adding bamboo fiber.

At the same time, it is found that the storage modulus of PLA was elevated by the addition of APP or bamboo fiber, representing that the rigidity of the material was enhanced, especially the bamboo fiber added ones. Among these, PFEA performed the best (4423 MPa). In addition, the storage moduli of PEA and PFEA (2051, 4423 MPa) were larger than those of unmodified APP containing ones—PA and PFA (1916, 2997 MPa). It is speculated that the modified APP can have better compatibility with PLA, so there is a better reinforcing effect. The proposed reaction mechanisms between modified APP and PLA are shown as Fig. 6.2.

From Table 6.2, it can be found that with the addition of bamboo fiber or APP to PLA, the loss moduli of composites have an increasing trend, representing that the toughness of the composites has been increased, especially the samples containing bamboo fibers (PF, PFA and PFEA). It is speculated that the hollow structure of the fiber can assist the PLA composites to absorb energy, so that the loss modulus of PLA can be improved.

Table 6.3 shows the results of the flame retardant analysis of PLA and its composites. It can be observed that the evaluation of pure PLA is not flame retardant (no rating), and still has no rating by the addition of bamboo fiber. It also did not achieve flame retardancy by the simple addition of flame retardant APP or modified APP (PA and PEA); the testing specimen produced a serious droplet phenomenon. The flame retardant grade can reach V-2 by adding bamboo fiber and APP (PFA) to the

Table 6.2 HDT and DMA data of PLA and composites

Sample	HDT (°C)	E′ (MPa)	E''_{max} (MPa)
PLA	54.7	1740	324.6
PF	58.4	2825	470.2
PA	73.1	1916	315.3
PFA	108.8	2997	469.5
PEA	75.8	2051	348.8
PFEA	115.3	4423	400.8

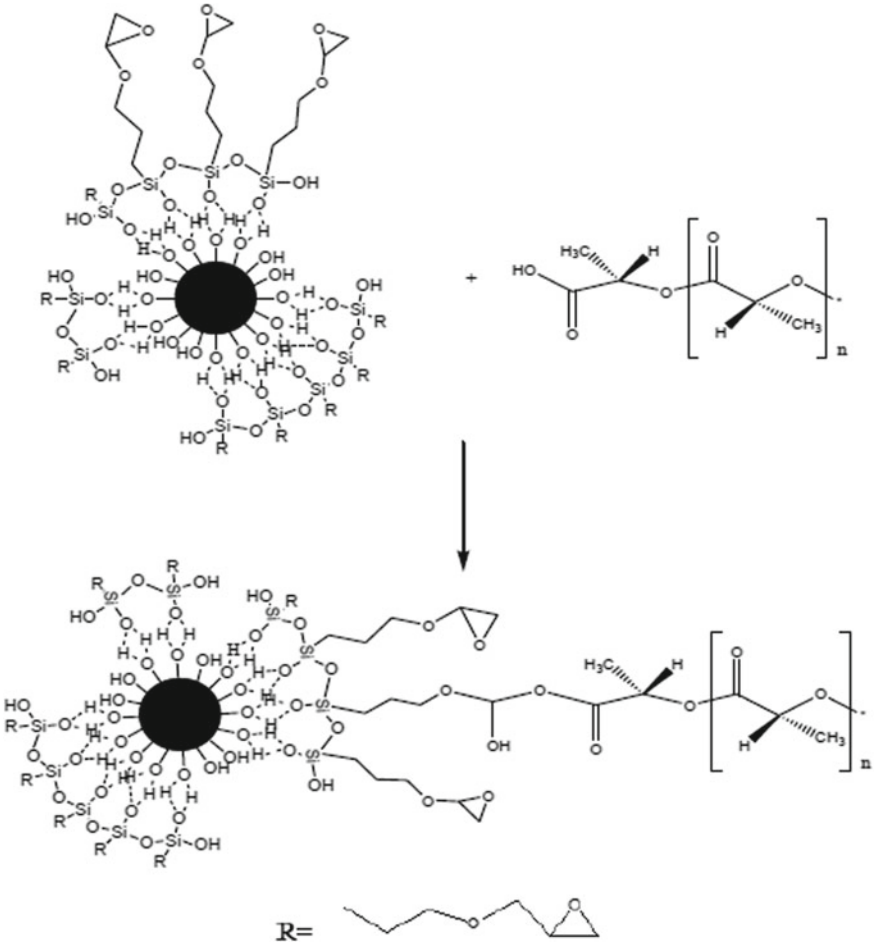

Fig. 6.2 Proposed reaction mechanisms between modified APP and PLA

Table 6.3 UL-94 test data of PLA and composites

	Flame retardancy
PLA	No rating
PF	No rating
PA	No rating
PFA	V-2
PEA	No rating
PFEA	V-0

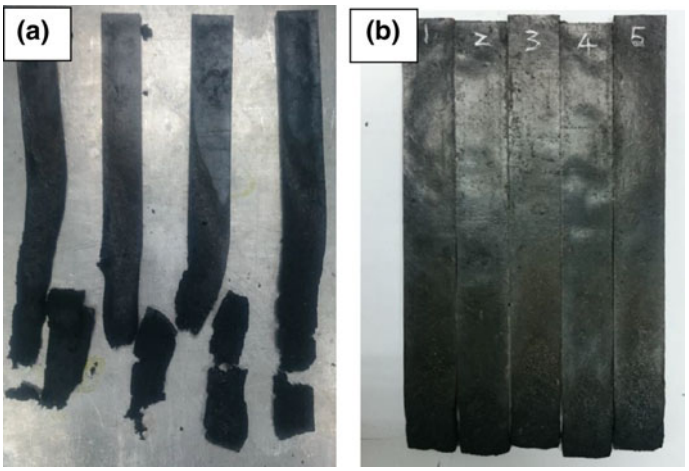

Fig. 6.3 Appearance of the **a** PFA and **b** PFEA test specimen after the UL-94 test

PLA. Moreover, the grade can reach the highest level of flame retardant V-0 with the addition of bamboo fiber and the modified APP (PFEA). It can be seen that the flame retardant effect of modified APP is better than that of APP. In addition, bamboo fiber can not only enhance the mechanical properties and heat resistance of PLA, but also produce synergistic flame retardant effects with flame retardants. Figure 6.3 is the appearance of the PFA and PFEA test specimen after the UL-94 test. It can be seen that the PFEA specimen is still very intact; however, the PFA specimen shows a little fragmentation phenomenon.

The SEM photographs of the fracture surface of PFA and PFEA are shown in Fig. 6.4. It is found from Fig. 6.4a that the compatibility of the unmodified APP and the PLA matrix is poor, as evidenced by the presence of voids and pull-out bamboo fibers on the fracture surface, which led to its weak thermal and mechanical properties. On the other hand, a densely knitted texture was found in Fig. 6.4b, indicating that the compatibility between modified APP and the PLA matrix is improved. This result corroborates the results of the thermal and mechanical analysis which determined that better adhesion in the additives/matrix increases both the HDT and the strength of the composite.

6.4 Conclusions

The green composite with the modified APP and bamboo fiber has a high non-flammable ratio with a char yield of 30.8%. The HDT and storage modulus of PLA can be significantly increased by the addition of both flame retardant and bamboo fiber.

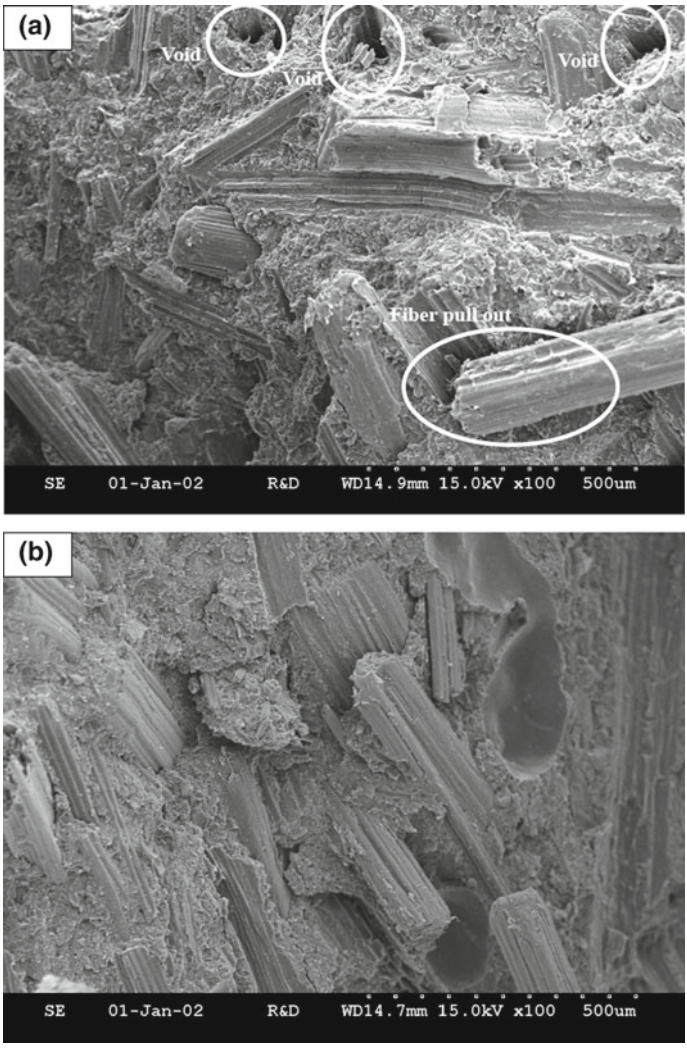

Fig. 6.4 SEM photographs of the fracture surface of **a** PFA and **b** PFEA

Moreover, the storage moduli of modified APP containing composites were larger than those of unmodified APP containing ones. It is speculated that the compatibility between the modified APP and PLA has improved, leading to a better reinforcing effect.

It also can be found that the loss moduli of composites were significantly increased by the addition of bamboo fiber due to its ability to absorb energy by the hollow structure of the fiber. Moreover, the flame retardant grade of PLA can reach the highest level of V-0 after the addition of both the bamboo fiber and the modified APP. It revealed that the flame retardant effect of modified APP is better than that of

APP. Moreover, bamboo fiber can not only enhance the mechanical properties and heat resistance of PLA, but also play an important role in synergistic flame retardancy with flame retardants.

References

1. H. Zhu, Q. Zhu, J. Li, K. Tao, L. Xue, Q. Yan, Synergistic effect between expandable graphite and ammonium polyphosphate on flame retarded polylactide. Polym. Degrad. Stab. **96**, 183–189 (2011)
2. Y. Ikada, H. Tsuji, Biodegradable polyesters for medical and ecological applications. Macromol. Rapid Commun. **21**, 117–132 (2000)
3. O. Martin, L. Averous, Poly(latic acid): plasticization and properties of biodegradable multiphase systems. Polymer **42**, 6209–6219 (2001)
4. D. Garlotta, A literature review of poly(lactic acid). J. Polym. Environ. **9**, 63–84 (2001)
5. S.S. Ray, K. Yamada, K. Okamoto, K. Ueda, New polylactide-layered silicate nanocomposites. 2. Concurrent improvements of material properties, biodegradability and melt rheology. Polymer **44**, 857–866 (2003)
6. C.H. Ke, J. Li, K.Y. Fang, Q.L. Zhu, J. Zhu, Q. Yan et al., Synergistic effect between a novel hyperbranched charring agent and ammonium polyphosphate on the flame retardant and anti-dripping properties of polylactide. Polym. Degrad. Stab. **95**, 763–770 (2010)
7. L.L. Wei, D.Y. Wang, H.B. Chen, L. Chen, X.L. Wang, Y.Z. Wang, Effect of a phosphorus-containing flame retardant on the thermal properties and ease of ignition of poly(lactic acid). Polym. Degrad. Stab. **96**, 1557–1561 (2011)
8. X. Wang, Y. Hu, L. Song, S. Xuan, W. Xing, Z. Bai et al., Flame Retardancy and thermal degradation of intumescent flame retardant poly(lactic acid)/starch bio-composites. Ind. Eng. Chem. Res. **50**, 713–720 (2011)
9. Y.Y. Wang, Y.F. Shih, Flame-retardant recycled bamboo chopstick fiber reinforced poly(lactic acid) green composites via multifunctional additive system. J. Taiwan Inst. Chem. Eng. **65**, 452–458 (2016)
10. F. Shukor, A. Hassan, Mds. Islam, M. Mokhtar, M. Hasan, Effect of ammonium polyphosphate on flame retardancy, thermal stability and mechanical properties of alkali treated kenaf fiber filled PLA biocomposites. Mater. Des. **54**, 425–429 (2014)
11. Z.B. Shaoa, C. Denga, Y. Tana, M. Chen, L. Chena, Y.Z. Wang, Flame retardation of polypropylene via a novel intumescent flame retardant: Ethylenediamine-modified ammonium polyphosphate. Polym. Degrad. Stab. **106**, 88–96 (2014)
12. Z. Qin, D. Li, W. Zhang, R. Yang, Surface modification of ammonium polyphosphate with vinyltrimethoxysilane: preparation, characterization, and its flame retardancy in polypropylene. Polym. Degrad. Stab. **119**, 139–150 (2015)
13. P. Pan, B. Zhu, W. Kai, S. Serizawa, M. Iji, Y. Inoue, Crystallization behavior and mechanical properties of bio-based green composites based on poly(L-lactide) and Kenaf Fiber. J. Appl. Polym. Sci. **105**, 1511–1520 (2007)

Part III
Green Composites

Chapter 7
Study of Morphology and Environmental Properties of Styrene-Butadiene Rubber-Carbon Black Nanocomposites

Rajesh H. Gupta, Rani V. Mankar and Wasudeo B. Gurnule

Abstract Rubber-nanocomposite (SBR-carbon black) was incorporated by the emulsion method. Rubber-nanocomposite pieces have been resolved based on their elemental examination. FTIR and Raman spectra were concentrated to clarify the structure. The exterior morphology of the copolymer gum was examined by checking SEM and it sets up the transition state among crystalline and shapeless nature. Ozone resistance was concentrated to clarify intermittent perceptions of the outside of the examples were made for break commencement. Tests were uncovered for longer moment in time. Fire resistance was concentrated to measures the simplicity of annihilation of a fire and four evaluations are conceivable, contingent on the consuming point and the nearness of burning drips. The current examination involving the emulsion method where environmental performance of rubber-nanocomposite is found to be good.

7.1 Introduction

As of late, incredible considerations have been paid to nanoparticles because of its uncommon highlights, for example, surface impacts, little size impacts, limit reactions and the naturally visible quantum impacts [1–3]. Polymer degradation includes the difference in at least one physical property, bringing about defeat of the appropriateness of the objects for the expected functions [4]. Be that as it may, the total of nanoparticles inferable from the high surface vitality and surface extremity debilitates their exceptional nature [5]. Trans-polyoctylene elastic (TOR) has been presented as a compatibilizer for inconsistent elastic mixes including polar elastics, for example, acrylonitrile butadiene elastic and non-polar elastic styrene butadiene elastic (SBR), and as a preparing helps for a very firm elastic compound, for

R. H. Gupta
Department of Chemistry, KZS Science College, Kalmeshwar, Nagpur 441501, India
e-mail: gupta.vaishna@gmail.com

R. V. Mankar · W. B. Gurnule (✉)
Department of Chemistry, Kamla Nehru Mahavidyalaya, Nagpur 440024, India
e-mail: wbgurnule@yahoo.co.in

R.-I. Murakami et al. (eds.), *NAC 2019*, Springer Proceedings in Physics 242,
https://doi.org/10.1007/978-981-15-2294-9_7

example, profoundly filled elastic mixes for skim-covering of steel wires for tires [6]. Trans-polyoctylene elastic (TOR) is a low atomic weight polymer, produced using cyclo-octene by metathesis polymerization, it is an elite polymer that exhibits a double character: during preparing, it has the capacity of a plasticizer, and after vulcanization, it carries on as an elastic and has been known as a compatibilizer for inconsistent mixes. Styrene elastic (SBR) is a broadly useful manufactured elastic having high filler stacking limit; great flex obstruction, split commencement opposition and scraped spot safe, which make it helpful for a few designing and modern application. By and by, as other unsaturated rubbers, it's profoundly helpless against debasement because of essence of twofold securities in the fundamental chain [7]. When alluding to enduring presentation there are a kind of corruption that ought to be viewed as, for example, bright light debasement which is the elastic influenced by UV beam and photo degradation and furthermore the ozone debasement. In spite of the fact that ozone is available in the climate at fixations regularly in the scope of 0–7 sections for each pphm, it can seriously assault on non safe elastics. The cooperation of elastic with ozone is great recorded when the elastic is focused or extended being used. Progression of splits creates, after some time, which is opposite to the applied pressure. Further presentation of these split surfaces to ozone cause the break to end up more extensive and more profound until the elastic falls flat [8, 9].

In this work, we prepared SBR- nanocomposites copolymer with the use of nano carbon black as filler by emulsion polymerization method. The impact of nano carbon black on the elemental, spectral, SEM and environmental properties has been studied. Elemental analysis, fourier transform infrared (FTIR), raman spectroscopy, morphology and environmental properties are carried out for all five composites (Fig. 7.1).

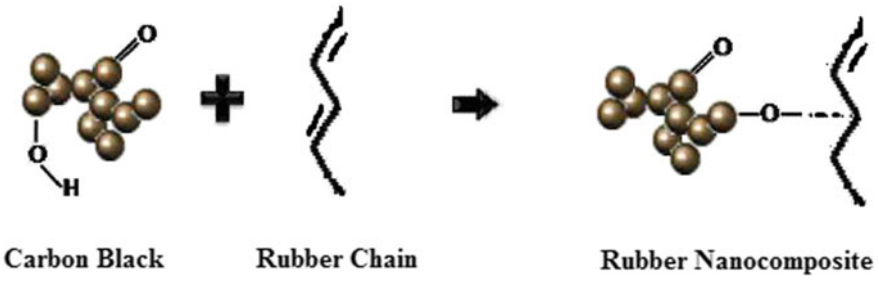

Fig. 7.1 Graphical diagram of SBR-carbon black nanocomposites

7.2 Experimental

7.2.1 Materials

Nanocomposites were acquired from Centre Scientific Company Nagpur, India. Tetramethyl Thiuram Disulfide, 2, 2′- Dithiobis, Stearic Acid and *N, N′* - Diphenyl *P*-Phenylene Diamine were purchased from Centre Scientific Company Nagpur, India. Zinc oxide and sulphur (Post Graduate Department of chemistry Kamla Nehru Mahavidyalaya, Nagpur, India). Styrene butadiene rubber latex obtained from Shree Radha Polymer Company, Nagpur, India.

7.2.2 Styrene Butadiene Rubber Nanocomposites Preparation

In the first place, carbon black was scattered in toluene with lively stirring and carbon black mixture was acquired at room temperature. At that point styrene butadiene rubber matrix was included into the carbon black mixture and mixed up to consistent blending of SBR into the carbon black. The blend was coagulated at room temperature. At that point rinsed with water a few times and afterward dried at 70 °C for 12 h. At that point SBR-nanocomposite was obtained.

7.2.3 Rubber Compounding

SBR matrix was blended with different fixings appeared in Table 7.1. The SBR-nanocompound then was vulcanized at 150 °C. The blend of SBR-nanocomposites

Table 7.1 Rubber formulation

Fixings	Parts per hundred ratio of rubber				
Sample code	1	2	3	4	5
Styrene Butadiene Rubber	100	100	100	100	100
Carbon black	0	2	6	10	12
Stearic Acid	2	2	2	2	2
Zinc Oxide	5	5	5	5	5
2, 2′-Dithiobis	0.5	0.5	0.5	0.5	0.5
Tetramethyl Thiuram Disulfide	0.2	0.2	0.2	0.2	0.2
N, N′- Diphenyl *P*-Phenylene Diamine	1	1	1	1	1
Sulphur	2	2	2	2	2

were straightforwardly operate on two-roll mill and blending for 15 min., at that point including every single fundamental fixings which are recorded in Table 7.1 and blending for 10 min. The final complex was vulcanized at 150 °C.

7.3 Characterizations

7.3.1 Fourier Transform Infrared Spectroscopy (FTIR)

FTIR spectra of SBR-nanocomposites were obtained by using a shimadzu IR-Affinity spectrophotometer (Kamla Nehru Mahavidyalaya, Nagpur, India).

7.3.2 Raman Spectra

The Raman distribution analyses were carried out by employing a Jobin-Yvon T64000 spectrometer. In order to restrict the fluorescence sway, Styrene Butadiene Rubber, SBR with nanocompound were lit up with an argon-krypton molecule laser (Coherent model Innova 70C) working at the 647.1 nm (red line). The laser bar was locked in by a × 100 enhancement focuses of a confocal intensifying focal point (Olympus BX40) (from National Chemical Laboratory Pune, India). Each range was accumulated in the repeat run 400–3500 cm^{-1} in excess of 60 s and with 10 collections to avoid electronic apexes and ordinary establishment.

7.3.3 Morphology

Exterior morphology of the nanocomposites was investigated by using Scanning electron microscope JEOL (JSM-6390, STIC Cochin) at a speeding up voltage of 3 kV. Because of the extremely restricted electron shaft, SEM images have a huge profundity of field yielding a trademark 3-dimensional form helpful for identifying the exterior structure of tests.

7.3.4 Ozone Obstruction

The cavity gave an air a restricted grouping of ozone and temperature. Ozone focus chose was 50 pph, which is created by UV light. The examination was completed according to ASTM D1149-99 particulars at 38.50 C (from Shree Radha Polymer Rubber Industry Nagpur, India).

7.3.5 Flame Resistance

Fire resistance of vulcanizates of SBR elastic nanocomposites were assessed according to UL 94 diagram examination for combustibility of rubber samples for parts in gadgets and apparatuses (from Shree Radha Polymer Rubber Industry Nagpur, India). Strategy V 94, utilized for perpendiculars consume examination was applied. The experimental examples were (portions of 12 × 100 and width 2.0 mm slice from formed vulcanizates) seized toward one side in the perpendicular place.

7.4 Results and Discussion

7.4.1 Elemental Measurements

All five rubber nanocomposites were analyzed at Sophisticated Analytical Instrumentation Facility, Cochin for C, H, N and S. The empirical formula for all the five SBR, SBR-carbon black (2 phr), SBR-carbon black (6 phr), SBR-carbon black (10 phr) and SBR-carbon black (12 phr) were determined on the basis of C, H, N and S by messenger method. The watched outcomes are seen as in great concurrence with the determined qualities. From the empirical formula, the observational load of a single repeating unit was determined. Analytical data for all the five SBR-carbon black nanocomposites are presented in Table 7.2.

Table 7.2 Microanalysis information of Styrene-Butadiene rubber-carbon black composites

Rubber samples	% of C observed (Cal.)	% of H observed (Cal.)	% of N observed (Cal.)	% of O observed (Cal.)	% of S observed (Cal.)	Empirical formula	Empirical weight
Styrene butadiene rubber	83.44 (81.44)	8.11 (8.05)	2.56 (2.31)	5.85 (5.08)	2.34 (1.39)	$C_{38}H_{44}N_1O_2S$	546.993
SBR-CB (2 phr)	85.12 (84.87)	8.16 (8.10)	2.10 (2.21)	5.40 (5.04)	1.07 (1.00)	$C_{42}H_{48}NO_2S$	592.657
SBR-CB (6 phr)	84.26 (83.20)	9.09 (8.99)	2.24 (2.20)	5.34 (5.01)	1.07 (1.02)	$C_{42}H_{54}N_1O_2S$	598.705
SBR-CB (10 phr)	80.40 (81.22)	9.65 (8.89)	2.23 (2.10)	5.66 (4.60)	2.99 (2.05)	$C_{42}H_{60}N_1O_1S_1$	627.008
SBR-CB (12 phr)	82.89 (80.67)	10.27 (9.12)	2.29 (2.12)	5.26 (4.20)	1.58 (1.02)	$C_{42}H_{62}N_1O_2S$	612.963

7.4.2 Fourier Transform Infrared Spectroscopy

FTIR spectra of various loadings levels of carbon black shows in Fig. 7.2. In every spectrum, the expansive top at 3400 cm^{-1} is appointed to extending vibration of –OH group stretching vibrations alongside adsorbed water. The tops at 950 and 860 cm^{-1} are because of C–H bending of aromatic ring in carbon black. The peak at 1100 and 470 cm^{-1} are because of antisymmetric and symmetric extending. The presence of two sharp peaks at 2930 and 2840 cm^{-1} and one top around 1450 cm^{-1} for all the spectra of SBR-filler also of the assimilation groups comparing to the vibration of explicit useful gathering. These little pinnacles of around 2930 and 2840 cm^{-1} are main groups of symmetric and antisymmetric extending vibrations of $–CH_2$ bunch individually. 1450 cm^{-1} corresponding to bending vibrations of $–CH_2$ group. Every one of these pinnacles is seen in spectra of SBR-nanocomposites in

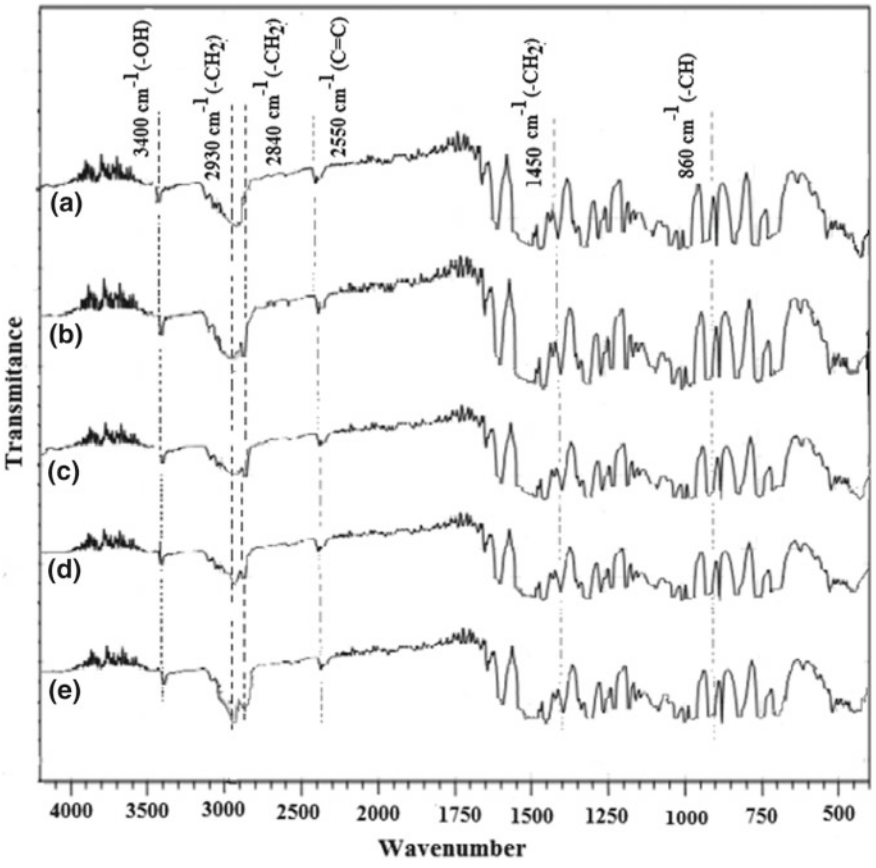

Fig. 7.2 FTIR spectra of SBR-nanocomposite **a** unfilled rubber composites, **b** 2 phr carbon black, **c** 6 phr carbon black, **d** 10 phr carbon black, **e** 12 phr carbon black

Table 7.3 FTIR spectral data of SBR-carbon black nanocomposites

Assignment	Expected wavenumber (cm^{-1})	Observed wavenumber (cm^{-1})
OH (phenolic)	3100–3500	3400 (b)
Functional group(C=O)	1700–1730	1750 (st)
Aromatic ring (C–H)	960–990	950 and 860 (sh)
[(CH_2) methylene bridges]	2500–3100	2930 and 2840 (sh)
Alkene group	990–1000	1080 (w)
Aromatic ring (C=C)	2100–2550	2550 (b)
[(CH_2) methylene bridge]	1250–1360	1450 (sh)

Sh sharp, *b* broad, *st* strong, *w* weak

Fig. 7.2. This is furthermore bolstered by the nearness of group at 1080 cm^{-1} which is characteristic band of alkene gathering. The top at 1750 cm^{-1} of carbon black when CO initiation which shows the nearness of C=O functional gatherings portrayed by aldehydes, ketones, carboxylic acids and esters. The nearness of band at 2550 cm^{-1}, which is trademark band of C=C fragrant gathering. On account of carbon black, the filler-rubber collaboration is mostly of objective character [10] (Table 7.3).

7.4.3 Raman Spectra

The closeness of contaminating impact and development of crosslinking operators, fillers and other elastic fixings into versatile are the essential reasons of fluorescence parasite flag in Raman dispersing range, principally with the laser excitation lines in the noticeable locale [11]. The yield of the fluorescence procedure is a lot greater than that of the Raman procedure, and in this way the primary raman data is covered. So as to unmistakably distinguish the trademark groups of SBR and SBR-nanocomposites, the coagulated elastic without carbon black was initially chosen to carry out Raman spectroscopy. The spectrum of SBR and SBR-carbon black composites are analyzed in Fig. 7.3 and band assignments are done dependent on correlation with writing spectra. The Raman pinnacles of SBR are just halfway doled out in the writing [12]. This work gives a complete credit for which Raman investigation of styrene and butadiene elastic is great direction. Both symmetric and unbalanced $–CH_2$ and $–CH_3$ extending sensations ordinarily show up in the 2800–3000 cm^{-1} district. Clearly, C=C extending atmosphere of SBR are seen at 1666 and 1668 cm^{-1}, individually. Likewise, there are a couple of secured indication of SBR and SBR-carbon black

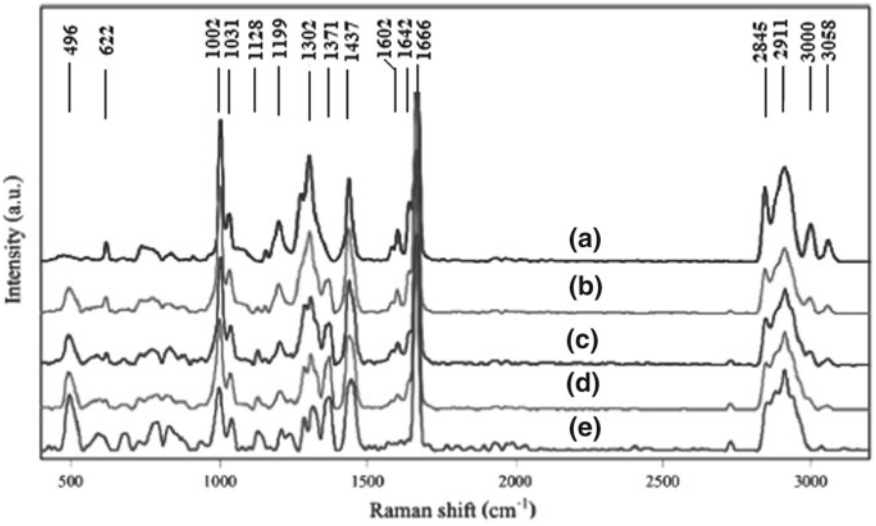

Fig. 7.3 Raman spectra of SBR-nanocomposite **a** unfilled rubber composites, **b** 2 phr carbon black, **c** 6 phr carbon black, **d** 10 phr carbon black, **e** 12 phr carbon black

matrix which can't be utilized to perceive their responsibilities, in this way just the characteristic pinnacles allowing partition will be based on. Raman spectra of unfilled SBR tests at various blend extents are appeared in Fig. 7.3. The outcomes show that force of Raman pinnacles relies upon the mix piece. As can be seen, the powers of characteristic signals at 1002, 1302, 1602 and 3058 cm^{-1} will in general increment with expanding carbon dark substance in the SBR elastic, though the forces of the confined trademark groups of SBR at 1371, 1128 and 496 cm^{-1} lessening. The top at 1666 cm^{-1} isn't subject to SBR proportion and is utilized as an interior standard. From this relationship, it is conceivable to affirm synthesis in the mixes by plotting the power proportion of trademark sign of each elastic versus mix proportion. It could be noted here that the characteristic signals at 1371 and 1302 cm^{-1} of $–CH_3$ antisymmetric deformation and =C–H in-plane deformation for SBR, individually, were picked for construct an modification bend. This is on the grounds that these selected tops have the best aims and the characteristic top at 1371 cm^{-1} isn't covered. Raman trademark sign of SBR are not fundamentally changed after expansion of carbon black. This perception is presumably because of the combination of low quantum effectiveness in this recurrence run (647.1 nm) and the frail Raman force of carbon black particles which have an indistinct character. Tragically, pinnacles of SBR appointed to $=CC_2$ shaking and $C–CH_2$ extending are situated in a similar recurrence district at 496 and 1000 cm^{-1}, separately, [13]. In this manner, it is hard to recognize the Raman sign of carbon black from those of SBR.

7.4.4 Morphology

Figure 7.4 shows SEM pictures for SBR-carbon black nanocomposites. The estimations were performed legitimately on the break surface (cross area) of the examples utilizing amplification level of multiple times [14, 15]. Morphology of the elastic complex at a variety of filler load up viz. at 2, 6, 10 and 12 phr was researched by scanning electron microscopy (SEM) and micrographs are appeared in Fig. 7.4. Figure 7.4 demonstrates the filler elements are homogenously spread all through the elastic lattice with few totals at 2 phr filler content in rubber composites (Fig. 7.4a)

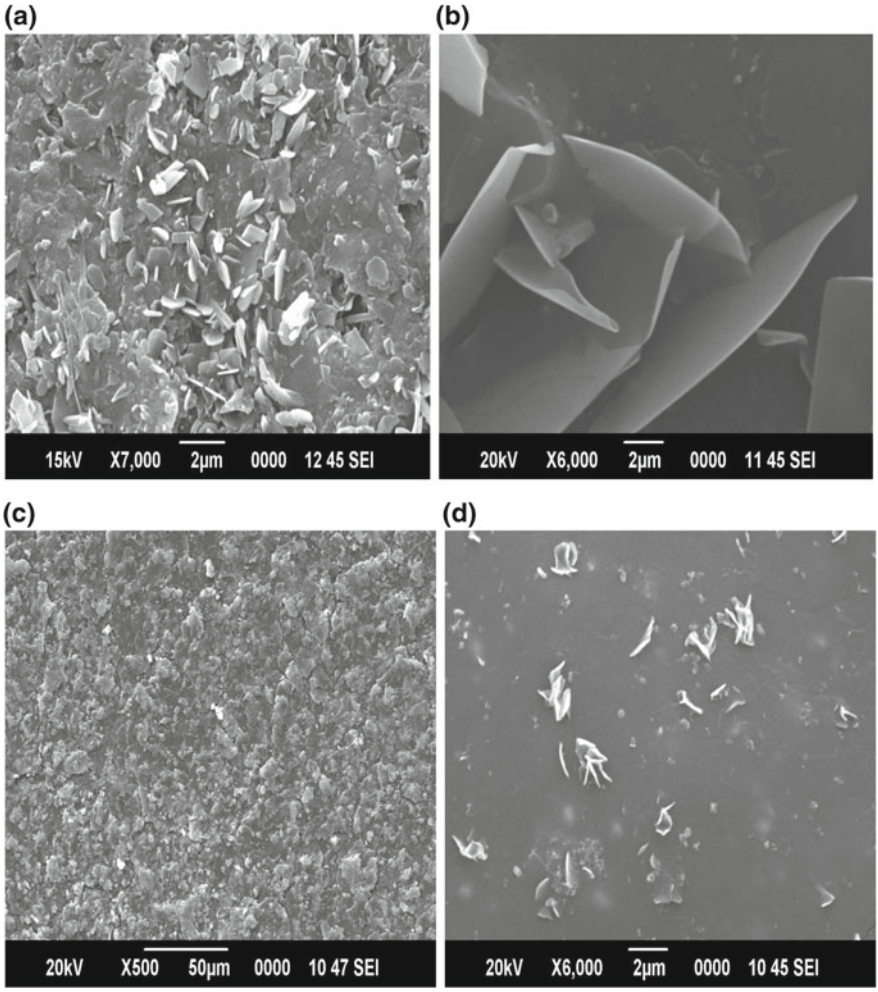

Fig. 7.4 SEM images of SBR-nanocomposite: **a** 2 phr filler, **b** 6 phr, **c** 10 phr, **d** 12 phr

with growth in filler loading (10 and 12 phr), the collection tendency of filler particles growth and it is a lot of overwhelming for elastic grid loaded up with 12 phr (Fig. 7.4d). In Fig. 7.4d, demonstrates the molecule size dispersion is in the scope of 100–150 nm for littler elements while size of larger filler elements totals deception in the scope of 300–450 nm. Homogeneous dispersion of filler into rubber structure is apparent in all plane arranged filler compounds a–d (Fig. 7.4).

7.4.5 Ozone Resistance

SBR elastic nanocomposites vulcanisates show great defense from ozone for the reason that of its polar character. Figures 7.5 and 7.6 reveals the visual photos of the ozone lighted planes of SBR elastic nanocomposites in an ozone compartment at 50 pphm ozone fixations at 380 °C. Inside the principal 4 h itself breaks were formed on the exterior of SBR gum analysis. In any case, it is considered that to be the filler load up is expanded up to 12 wt% the time taken for the initiation of split is extended. For SBR-nanocomposites at 2, 6, 10 and 12 weight percent of carbon black fillings, the breaks were grown after 5, 6, 7 and 8 h separately. It is comprehended that SBR-Carbon black nanocomposites (12 phr) up to specific carbon black substance are fewer disposed to ozone light which shows that the best probable spreading of carbon black in the elastic network is up to that level. The spreading out in carbon black filling verified a more slow improvement and proliferation of breaks.

Elastomers, principally those including energetic twofold bonds in the principle series, are genuinely ambushed by ozone realizing significant parts toward a way inverse to the applied weight. Insurance against ozone assault can be cultivated by the use of antiozonants. A couple of assessments have been represented on the affirmation of versatile against ozone ambush [16]. The pro pack tests shows favored ozone restriction over the basic techniques on account of increasingly unmistakable obstacle to the headway of break front experienced on account of the identical transport of carbon black in the versatile cross section and the superior flexible filler collaboration.

Fig. 7.5 Ozone images of SBR rubber after exposure of 4 h

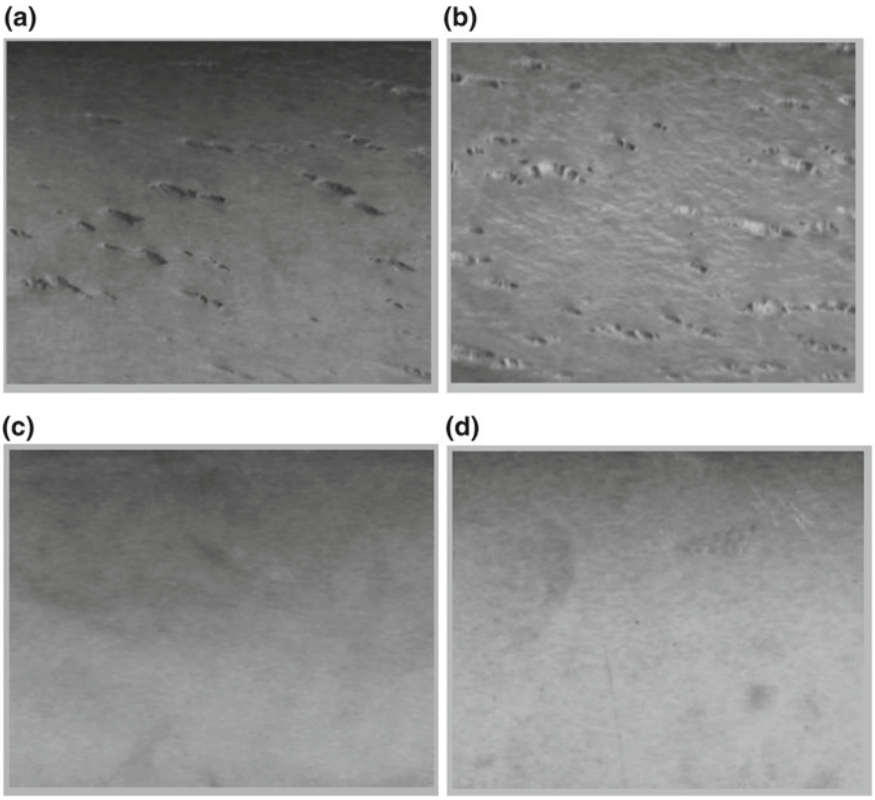

Fig. 7.6 Ozone images of SBR-nanocomposites **a** 2 phr carbon black, **b** 6 phr carbon black, **c** 10 phr carbon black, **d** 12 phr carbon black after exposure of 8 h

7.4.6 Flame Resistance

Fire resistance of vulcanisates of SBR elastic carbon dark nanocomposites were surveyed by UL 94 outline test for instability Vulcanizates of shifting carbon black substance in Styrene Butadiene Rubber were tried according to UL 94 by vertical consume test. SBR-carbon black nanocomposites kept consuming after the burner fire application and flaring dribbles touched off the cotton set beneath the example, yet set aside more effort to finish consuming than unadulterated SBR, showing improvement in fire opposition [17, 18]. In the event that we need to use a framework as a fire retardant, it must qualify under the UL-94 convention. This is just a test that estimates the simplicity of annihilation of a fire and four evaluations are conceivable, contingent on the consuming time and the nearness of blazing dribbles. On the off chance that a material stifles quickly, without trickling, it's managed the ranking V-0; a substance that consumes to some degree longer, yet doesn't dribble, is delegated V-1; a material that doesn't self-smother in a brief timeframe yet dribbles is specified

Table 7.4 Dripping and consuming attributes, just as the UL-94 arrangement for the frameworks

Nanocomposites	Dripping	Consuming	UL-94
Styrene butadiene rubber	Slow	Yes	NC
SBR-carbon black (2 phr)	Slow	Yes	NC
SBR-carbon black (6 phr)	Yes	Little	V-2
SBR-carbon black (10 phr)	Yes	Little	V-2
SBR-carbon black (12 phr)	Yes	Little	V-2

the ranking V-2; if a substance consumes longer than the convention determines, it's said to be not grouped, NC. SBR-carbon black nanocomposites at 2, 6, 10 and 12 phr weight percentage of carbon black stacking indicates fairly improved combustibility property than its gum as given in Table 7.4. This improvement in property is a direct result of the fireproof property of carbon black.

7.5 Conclusions

Rubber-nanocomposite was prepared by the process of emulsion polymerization of SBR with carbon black and other ingredients i.e. accelerators and antioxidants. Morphology of rubber-nanocomposite demonstrates the filler particles are homogenously dissipated all through the flexible cross section. The ace group tests shows preferable ozone resistance over the normal methods because of more noteworthy deterrent to the advancement of break front experienced because of the uniform dissemination of carbon dark in the elastic grid and the improved elastic filler cooperation. Fire obstruction use a framework as a fire retardant, it must qualify under the UL-94 convention. This is essentially a test that estimates the simplicity of elimination of a fire and four evaluations are conceivable, contingent on the consuming time and the presence of flaming drips. SBR-carbon black nanocomposites at 2, 6, 10 and 12 phr weight percentage of carbon black stacking demonstrates to some degree enhanced combustibility property than its gum. This upgrade in property is because of the flame resistant property of carbon black.

Acknowledgements The authors are thankful to STIC, Cochin for elemental analysis results. Authors are also thankful to National Chemical Laboratory, Pune for carrying out Raman Spectroscopy of the rubber-nanocomposites.

References

1. A. Hoffman, A. Lafosse, Sh Michaelson, M. Bertin, R. Azria, Surf. Sci. **602**, 3026 (2008)
2. H. Du, S.W. Lee, J. Gong, C. Sun, L.S. Wen, Mater. Lett. **58**, 1117 (2004)
3. D.G. Peng, J.S. Zhang, Q.L. Liu, E.W. Taylor, J. Inorg. Biochem. **101**, 1457 (2007)
4. T. Sahin, T. Sınmazcelik, S. Sahin, The effect of natural weathering on the mechanical, morphological and thermal properties of high impact polystyrene (HIPS). Mater. Des. **28**, 2303–2309 (2007)
5. J. Viguie, J. Sukmanowski, B. Nölting, F. Royer, Colloids Surf. A **302**, 269 (2007)
6. C. Nah, Effects of trans-polyoctylene rubber on rheological and green tensile properties of natual rubber/acrylonitrile-butadiene rubber blends. Polym. Int. **51**, 245–252 (2002)
7. C.K. Radhakrishan, A. Rosamma, G. Unnikrishnan, Thermal, ozone and gamma ageing of styrene butadiene rubber and poly (ethylene-co-vinyl acetate) blends. Polym. Degrad. Stab. **91**, 902–910 (2006)
8. P.B. Sulekhaa, R. Josepha, K.N. Madhusoodanan, K.T. Thomas, New oligomer-bound antioxidants for improved flex crack resistance and ozone resistance. Polym. Degrad. Stab. **77**, 403–416 (2002)
9. F. Findik, R. Yilmaz, T. Koksal, Investigation of mechanical and physical properties of several industrial rubbers. Mater. Des. **25**, 269–276 (2004)
10. J. Frohlich, W. Niedermeier, H.D. Luginsland, Compos.: Part A. **36**, 449 (2005)
11. T. Jawhari, A. Roid, J. Casado, Raman spectroscopic characterization of some commercially available carbon black materials. Carbon N. Y. **33**, 1561–1565 (1995)
12. S.W. Cornell, J.L. Koenig, The Raman spectra of polybutadiene rubbers. Macromolecules **2**, 540–545 (1969)
13. P.J. Hendra, K.D.O. Jackson, Applications of Raman spectroscopy to the analysis of natural rubber. Spectrochim. Acta A Mol. Spectrosc. **50**, 1987–1997 (1994)
14. T.A. Vilgis, Polymer **46**, 4223 (2005)
15. C.A. Rezende et al., Natural rubber-clay nanocomposites: mechanical and structural properties. Polymer **51**, 3644–3652 (2010)
16. N. Celette, I. Stevenson, L. Devenas, G. David, Vigier, IRAP Nucl. Instr. Meth. B. **185**(2001), 305, (2000)
17. D. Wang, K. Echols, A.W. Charls, Fire Mater. **29**, 283 (2005)
18. J.C. Wang, W.L. Hao, Effect of organic modification on structure and properties of room-temperature vulcanized silicone rubber/montmorillonite nanocomposites. J. Appl. Polym. Sci. **129**, 1852–1860 (2013)

Chapter 8
Comparative Study of Dye Removal Using PANI/TiO_2 and PANI/GNS Nanocomposites

Jitendra N. Ramteke, Neha V. Nerkar and Subhash B. Kondawar

Abstract The preparation of polyaniline/titania (PANI/TiO_2) and polyaniline/graphene nanosheets (PANI/GNS) nanocomposites by in situ chemical oxidation polymerization is reported for the comparison of their study for the removal of methyl orange (MO) from aqueous solution. Scanning electron microscopy (SEM) and ultraviolet-visible spectroscopy (UV-VIS) have been used to analyse the nanocomposites towards their morphology and adsorption kinetics for finding the suitability of metal oxide or graphene embedded polyaniline based nanocomposites. This study is a comparison for PANI/TiO_2 and PANI/GNS towards their applicability for the removal of MO in aqueous solution. The nanocomposites of different dimensionality PANI/TiO_2 and PANI/GNS are effective to remove the MO dye by 65–70%. The results obtained from adsorption kinetics by using pseudo first order model and pseudo second order model, it is indicated that the adsorption of dye is a physical adsorption. In comparison, metal oxide incorporated polyaniline has shown better percentage of removal of dye as compared to that of graphene incorporated polyaniline.

8.1 Introduction

It is generally known that dyes are colouring materials, organic in nature and used in many industries like textile, leather industry which are the major causes of environmental pollution. The textile industry uses excessively the various dyes which lead to severe pollution for the surface water causes contamination in groundwater due to release of toxic and colored effluents [1, 2]. Due to non-degradable and water soluble properties of most of the dyes, it is difficult to remove them from water once released into water from the textile industries. For the removal of dyes from the water, the

J. N. Ramteke
Department of Physics, Mohata Science College, Nagpur, India
e-mail: ramtekejitendra@yahoo.com

N. V. Nerkar · S. B. Kondawar (✉)
Department of Physics, Rashtrasant Tukadoji Maharaj Nagpur University, Nagpur, India
e-mail: sbkondawar@yahoo.co.in

R.-I. Murakami et al. (eds.), *NAC 2019*, Springer Proceedings in Physics 242,
https://doi.org/10.1007/978-981-15-2294-9_8

methods are available which includes reverse osmosis, ion exchange, precipitation and adsorption. Out of these, the adsorption is cost effective, simple and hence widely used [3]. For the removal of dye pollutants, semiconductor metal oxides such as TiO_2, ZnO, ZnS, CdS, Fe_2O_3 nanoparticles (NPs) and activated carbon have been shown to be the most promising materials in this field. TiO_2 and ZnO semiconductors have quite similar band gaps (ZnO, 3.37 eV and TiO_2, 3.2 eV) and have become the most extensively used photocatalysts in recent years. ZnO and TiO_2 photocatalysts have been reported for the photodegradation of organic pollutants from wastewaters [4, 5]. These photocatalysts are applicable to a wide range of organic synthetic dyes. Now-a-days, carbon nanotubes (CNT) and graphene nanosheets (GNS) have been used as photocatalysts [6]. Further to improve the photocatalytic activity of the materials, researchers have reported the preparation of various dimensional nonmaterial's and their composites with conducting polymers. Since, conducting polymers are reported to be the most photocatalytic material because of high electrical conductivity which provide better binding site for the adsorption of dyes molecules. Due to synergistic effect of two component such as nanomaterials with different dimension possesses high surface area to volume ratio and conducting polymer possesses high electrical conductivity, such composites material are highly photocatalytic advance material researching world-wide. One class of such hybrid material is conducting polymer such as polyaniline (PANI), polypyrrole (PPY), polythiophene (PTH), etc. PANI has been considered as a model conducting polymer due to its good environmental stability, redox properties, good electrical conductivity which is responsible for providing proper binding site for the adsorption of dye molecules [7].

With this background of preparation of conducting polymer nanocomposites especially for the removal of methyl orange dye present in water, herewith we report the preparation of PANI/TiO_2 and PANI/GNS for comparative study of removal of methyl orange with the application of ultraviolet and visible light. The kinetic modeling has been systematically applied for the comparison of photodegradation of dye using PANI/TiO_2 and PANI/GNS with the help of pseudo first order model, pseudo second order model and intra-particle diffusion model which have been tested and the validity of the models were verified by the linear equation analysis.

8.2 Experimental

8.2.1 Synthesis of Pure PANI

In 50 mL aqueous solution of aniline monomer (0.2 M) and hydrochloric acid (1 M), 50 mL of aqueous solution of ammonium persulphate (0.25 M) was added drop wise with constant stirring for 6 h and then kept for over night. PANI was obtained by centrifugation and washing with distilled water several times and then dried.

8.2.2 Synthesis of TiO_2 Nanoparticles

In a typical process for the synthesis of TiO_2 nanoparticles, the solution of titanium tetrachloride (3 mL) and ethanol (30 mL) was constantly stirred for 24 h. The sol was converted into gel and by heating at 120 °C for 1 h to evaporate water. Finally, the gel was calcined for 1 h at 900 °C to get TiO_2 nanoparticles [8].

8.2.3 Synthesis of PANI/TiO_2 Nanocomposite

PANI/TiO_2 nanocomposite was prepared by chemical oxidative polymerization. In a typical process, as-synthesized TiO_2 nanoparticles (0.93 g) were dispersed ultrasonically in 50 mL aqueous solution of aniline monomer (0.2 M) and hydrochloric acid (1 M). 50 mL of aqueous solution of ammonium persulphate (0.25 M) was added drop wise to above solution with constant stirring for 6 h and then kept for over night [9]. PANI/TiO_2 nanocomposite was obtained by centrifugation and washing with distilled water several times and then dried.

8.2.4 Synthesis of PANI/GNS Nanocomposite

Firstly, graphene nanosheets (GNS) were functionalized by using mixture of HCl and HNO_3 in 3:1 proportion [10]. Functionalized GNS (0.93 g) were dispersed ultrasonically in 50 ml aqueous solution of aniline monomer (0.2 M) and hydrochloric acid (1 M). 50 mL of aqueous solution of ammonium persulphate (0.25 M) was added drop wise to above solution with constant stirring for 6 h and then kept for over night. PANI/GNS nanocomposite was obtained by centrifugation and washing with distilled water several times and then dried.

8.3 Results and Discussion

8.3.1 Scanning Electron Microscopy

Figure 8.1 shows SEM images for (a) PANI/TiO_2 and (b) PANI/GNS. The encapsulation of layer of PANI on TiO_2 nanoparticles forming the core shell type structure for PANI/TiO_2 nanocomposite indicating more surface area which is beneficial for the molecules to be attracted [11, 12]. In case of PANI/GNS, the encapsulation of PANI on two dimensional functionalized graphene sheets also indicates the usefulness for the increase in dye adsorptivity. Pure PANI represents the spherical grain with well interconnection forming a net like structure but not uniform throughout as shown in

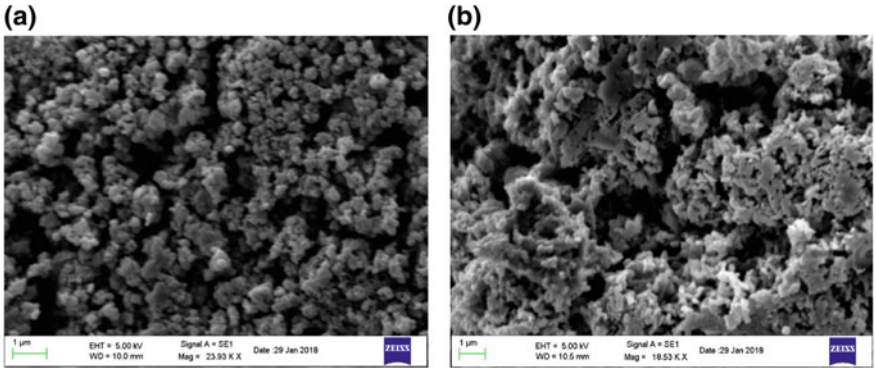

Fig. 8.1 SEM images of **a** PANI/TiO_2 and **b** PANI/GNS

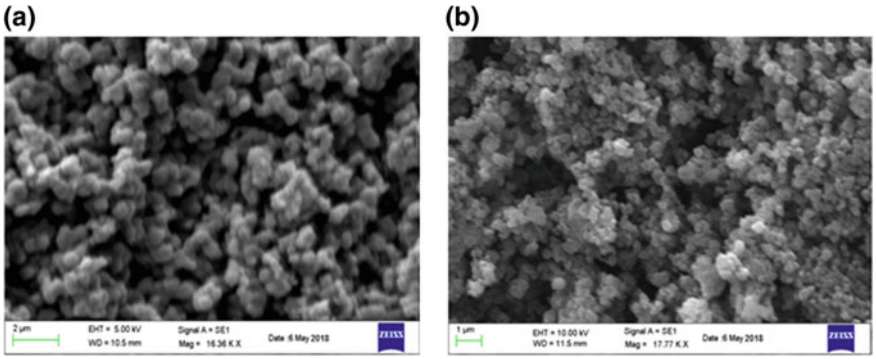

Fig. 8.2 SEM images of **a** PANI and **b** TiO_2 nanoparticles

Fig. 8.2a. The shape of the TiO_2 nanoparticles is close to have an almost spherical morphology consists of small grains distributed randomly as shown in Fig. 8.2b.

8.3.2 UV-Visible Spectroscopy

UV-Vis spectra of pure PANI, PANI/TiO_2 and PANI/GNS are shown in Fig. 8.3. The percentage of removal of methyl orange (MO) dye by using PANI/TiO_2 and PANI/GNS nanocomposites was calculated by Eq. (8.1);

$$percentage\ of\ removal = \frac{(C_o - C_e) * 100}{C_o} \tag{8.1}$$

where, C_o = Initial concentration and C_e = final concentration.

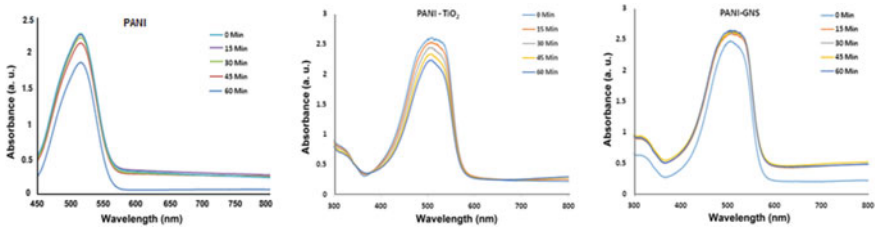

Fig. 8.3 UV-VIS spectra of pure PANI, PANI/TiO_2 and PANI/GNS

The experiment was carried out by taking initial dye concentration $C_o = 0.1$ gm/L prepared in de-ionized water. The dye solution in the presence of nanocomposite was stirred and readings were taken after each 15 min using UV-visible spectrophotometer [9]. From UV-Vis spectra of PANI/TiO_2 and PANI/GNS solutions as shown in Fig. 8.3, the absorbances have been tabulated as given in Table 8.1 with respect to time. After 60 min, the solution was filtered and dried. The final concentration Ce was measured by applying Beer Lamberts law $C = A/\in l$.

For PANI/TiO_2 nanocomposite, Ce was found to be 0.030 gm/L,

$$\% \text{ removal of MO} = (0.1 - 0.03) * 100/0.1 = 0.7 * 100 = 70\%$$

Similarly, for PANI/GNS nanocomposite, Ce was found to be 0.035 gm/L,

$$\% \text{ removal of MO} = (0.1 - 0.035) * 100/0.1 = 0.65 * 100 = 65\%$$

The pseudo first order model and pseudo second order model were tested and the validity of the models were verified by the linear equation analysis, by applying kinetic mechanism [13–15]. The pseudo-first-order kinetic model describes the adsorption of liquid/solid system based on solid capacity. The pseudo-first-order rate equation is given by Eq. (8.2)

$$\log(Q_e - Q_t) = \log Q_e - \frac{k_1}{2.303} t \tag{8.2}$$

where, Q_e and Q_t (mg g^{-1}) refer to the amount of dye adsorbed at equilibrium and time t (min), respectively, and k_1 is the pseudo-first-order rate constant. The values of Q_e and k can be determined experimentally by plotting $\log(Q_e - Q_t)$ versus t

Table 8.1 Absorbance for nanocomposites at different time

Nanocomposites	Absorbance (nm) at different time in min				
	0	15	30	45	60
PANI/TiO_2	2.598	2.439	2.328	2.231	2.198
PANI/GNS	2.636	2.621	2.598	2.581	2.428

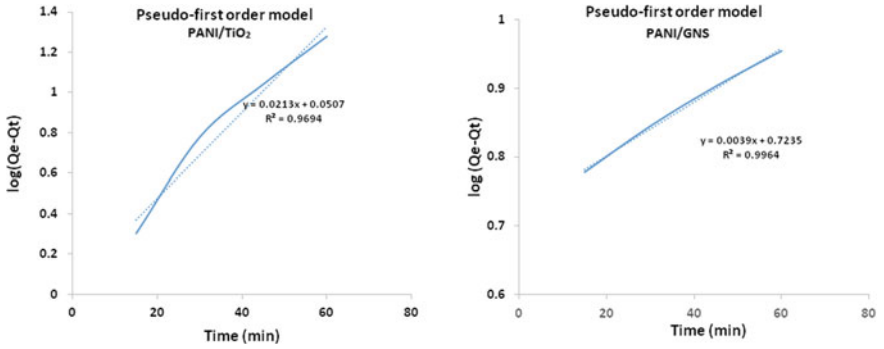

Fig. 8.4 Pseudo-first-order for plot of log(Qe-Qt) versus time for PANI/TiO_2 and PANI/GNS

and extracting information from the least squares analysis of slope and intercept and substituting into Eq. (8.2). Figure 8.4 shows the plot of the pseudo-first-order for PANI/TiO_2 and PANI/GNS nanocomposites.

The pseudo-second-order model can be represented by Eq. (8.3);

$$\frac{t}{Q_t} = \frac{1}{Q_e^2 k_2} + \frac{t}{Q_e} \tag{8.3}$$

where, k_2 is the rate constant of the pseudo-second-order model (g mg^{-1} min^{-1}). Figure 8.5 shows the curve-fitting plot of (t/Qt) versus time for PANI/TiO_2 and PANI/GNS nanocomposites. By closely comparing the linearity in the curves, it is seen that the pseudo second order model is quite applied to the adsorption of methyl orange dye using both PANI/TiO_2 and PANI/GNS nanocomposites.

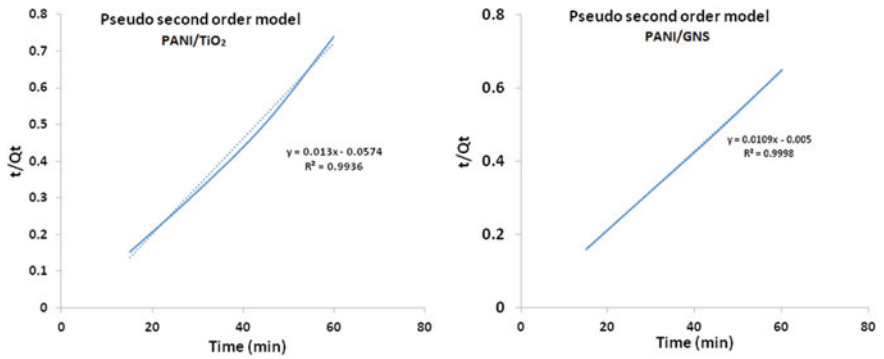

Fig. 8.5 Curve-fitting plot of (t/Qt) versus time PANI/TiO_2 and PANI/GNS nanocomposites

8.4 Conclusions

Polyaniline/titania (PANI/TiO_2) and polyaniline/graphene nanosheets (PANI/GNS) nanocomposites have been successfully synthesized by in situ chemical oxidation polymerization and systematically compared for the removal of methyl orange (MO) from aqueous solution. Photodegradation of methyl orange dye and adsorption kinetics were studied using UV-visible spectroscopy for finding the suitability of PANI/TiO_2 and PANI/GNS nanocomposites. The results obtained from adsorption kinetics by using pseudo first order model and pseudo second order, it is indicated that the adsorption of dye is a physical adsorption. In comparison, metal oxide incorporated polyaniline has shown better percentage of removal of dye as compared to that of graphene incorporated polyaniline.

References

1. A. Ozacan, A. Ozacan, Adsorption of acid dyes from aqueous solutions onto acid-activated bentonite. J. Colloid Interface Sci. **276**, 39–46 (2014)
2. E. Forgacs, C. Tibor, O. Gyula, Removal of synthetic dyes from wastewaters. Environ. Int. **30**, 953–971 (2004)
3. G. Annadurai, M. Chellapandian, M. Krishnan, Adsorption of reactive dye on chitin. Environ. Monitor. Asses. **59**, 111–119 (1999)
4. J. Kaur, S. Singhal, Facile synthesis of ZnO and transition metal doped ZnO nanoparticles for the photocatalytic degradation of Methyl Orange. Ceram. Int. **40**, 7417–7424 (2014)
5. S. Siuleiman, N. Kaneva, A. Bojinova, K. Papazova, A. Apostolov, D. Dimitrov, Photodegradation of Orange II by ZnO and TiO_2 powders and nanowire ZnO and ZnO/TiO_2 thin films. Colloids Surf. A Physicochem. Eng. Asp. **460**, 408–413 (2014)
6. G. Mahanta, M. Giridhar, S. Radhakrishanan, P. Satish, Adsorption and desorption kinetics of anionic dyes on doped polyaniline. J. Phys. Chem B. **113**, 2293–2299 (2009)
7. N. Nerkar, S. Kargirwar, S. Kondawar, D. Burghate, P. Burghate, Ultrasonicated organic acid doped polyaniline nanotubes for anionic dye detection in waste water. Int. Symp. Ultra. **22**(24), 195–198 (2015)
8. M.V. Bhute, Y.P. Mahant, S.B. Kondawar, Titanium dioxide/poly(vinylidene fluoride) hybrid polymer composite nanofibers as potential separator for lithium ion battery. J. Mat. NanoSci. **4**(1), 6–12 (2017)
9. N.V. Nerkar, S.B. Kondawar, S.K. Brahme, Y.H. Kim, Polyaniline/ZnO nanocomposites for the removal of methyl orange dye from waste water. Int. J. Modern Phys. B **32**(19), 1840085 (2018)
10. P. Modak, S.B. Kondawar, D.V. Nandanwar, Synthesis and characterization of conducting polyaniline/graphene nanocomposites for electromagnetic interference shielding. Procedia Mater. Sci. **10**, 588–594 (2015)
11. R. Saravanan, S. Karthikeyan, V. Gupta, G. Sekaran, V. Narayanan, A. Steapha, Enhanced photocatalytic activity of ZnO/CuO nanocomposite for the degradation of textile dye on visible light illumination. Mate. Sci. Engg. C **33**, 91–98 (2013)
12. B. Agarwal, T. Das, S. Baruah, Improvement of photocatalytic activity of Zinc Oxide nanoparticles using Zinc sulphide shell. J. Eng. **4**, 175–180 (2016)
13. F. Wu, R. Tseng, R. Juang, Initial behavior of intraparticle diffusion model used in the description of adsorption kinetics. Chem. Eng. J. **153**, 1–8 (2009)

14. J. Lin, L. Wang, Comparison between linear and non-linear forms of pseudo-first-order and pseudo-second-order adsorption kinetic models for the removal of methylene blue by activated carbon. Front. Environ. Sci. Eng. **3**, 320–324 (2009)
15. D. Zhao, W. Zhang, C. Chen, C. Wang, Adsorption of methyl orange dye onto multiwalled carbon nanotubes. Procedia Environ. Sci. **18**, 890–895 (2013)

Chapter 9
Electrospun Eu(TTA)$_3$Phen/Polymer Blend Nanofibers for Photoluminescent Smart Fabrics

Manjusha P. Dandekar, Sangeeta G. Itankar, Deoram V. Nandanwar and Subhash B. Kondawar

Abstract Here, we report an innovative electrospun composite nanofiber having a complex of Eu(TTA)$_3$Phen doped in a matrix of polymer blends prepared by electrospinning for designing smart fabrics. Europium complex Eu(TTA)$_3$Phen contains 2-thenoyltrifluoroacetone(TTA), 1,10-phenanthroline(Phen) and europium. It was synthesized by co-precipitation technique for the preparation of electrospun nanofibers of Eu(TTA)$_3$Phen/polymer blends such as Eu(TTA)$_3$Phen/PVDF-PMMA(Polyvinylidene fluoride-Polymethylmethacrylate) and Eu(TTA)$_3$Phen/PVDF-PS(Polyvinylidene fluoride-Polystyrene. Nanofibers of Eu(TTA)$_3$Phen/polymer blends were characterized by Scanning Electron Microscopy (SEM), Fourier Transform Infra Red (FTIR), X-ray diffraction (XRD) and Photoluminescence (Pl). Photoluminescence study of the nanofibers shows red emission which is allocated to the transitions between the first excited state ($^5D_0$) and the multiplet states ($^7F_{0\text{-}4}$). Due to the integration of Eu(TTA)$_3$Phen complex into the polymer matrix and subsequent distortion of the symmetry around the Eu^{3+} ions by the chapping Polymer, the polarization of the Eu^{3+} ions was improved, which increased the probability for electronic dipole allowed transitions. The Judd-Ofelt theory was used to calculate intensity parameters from emission data of Eu(TTA)$_3$Phen/polymers blends. As compared to PS and PMMA, presence of PVDF in both polymer blends generally increases the intensity of hypersensitive transition and perhaps is responsible for enhancement of photoluminescence properties. Electrospun nanofibers of Eu(TTA)$_3$Phen/PVDF-PS and Eu(TTA)$_3$Phen/PVDF-PMMA can be important candidate for designing photoluminescent smart fabrics.

M. P. Dandekar · S. G. Itankar · S. B. Kondawar (✉)
Department of Physics, Rashtrasant Tukadoji Maharaj Nagpur University, Nagpur, India
e-mail: sbkondawar@yahoo.co.in

M. P. Dandekar
e-mail: manjusha.dandekar@gmail.com

D. V. Nandanwar
Department of Physics, Mohata Science College, Nagpur, India

R.-I. Murakami et al. (eds.), *NAC 2019*, Springer Proceedings in Physics 242,
https://doi.org/10.1007/978-981-15-2294-9_9

9.1 Introduction

There has been an increasing interest in use of europium complex with β-diketones due to their intense emission peaks in the visible and near infrared region when excited by ultraviolet radiation. These photoactive europium complexes are of both essential and technological interest due to their distinguishing luminescence properties such as extremely sharp emission bands, potential high internal quantum efficiency and long lifetime of emission. The trivalent europium ion (Eu^{3+}) exposes strong and intense emission bands due to their f-f-electronics transition and broad range of luminescent lifetime, suitable for various applications, but they have low absorption coefficient, limiting the lighting output. However, these limitations can be improved by forming complexes of the rare-earth ions with organic ligands such as TTA and phen [1].

Chromophores of organic ligands used with europium shows strong absorption bands, so europium complex $Eu(TTA)_3Phen$ have ability to absorb much more light than the Eu^{3+} ions. These organic ligands used as an antenna effect in which it absorbs the excitation light and to shift the excitation energy to the higher energy levels of the Eu^{3+} ion, as of the emitting excited levels of Eu^{3+} ion can be populated [2, 3]. Organic ligand in complex such as Phen is a synergic shielding ligand which used to reduce the rate of non-radiative decays and strongly enhance the fluorescence intensity of the complex. Therefore, the key problem related to rare earth complex is to try to find a suitable matrix material to load them. Inorganic solid matrixes are promising host materials due to their good optical, thermal and chemical stability. In fact, many RE complexes have already been encapsulated in or adsorbed on host materials including silica, sol-gels and zeolite. A number of properties make polymers attractive hosts for rare-earth ions, including low cost, ease of fabrication on a wide range of substrates, low dispersion, and broad luminescence bands. Such europium complexes doped in polymers possess enhanced photoluminescence properties with this it shows improved thermal stability and mechanical flexibility [4]. The incorporation of europium complex into organic polymers presents an ideal and multipurpose approach to generate hybrid materials. It has been verified that the polymer-capped $Eu(TTA)_3Phen$ complexes possess improved photoluminescence properties and thermal stability, and are mechanically flexible. There is tremendous work going in textile for the fabrication of smart clothes with the use of nanofibers. Nanofibers of photoluminescent materials prepared by electrospinning method are in special demand. One-dimensional (1D) nanofibers are very interesting because of their surface properties, different from bulk materials. The photoactive $Eu(TTA)_3Phen$ complexes doped in polymer matrixes presents a class of new materials that shows the properties of both the europium complexes and the polymer matrix materials, useful in a wide range of new technologies. Nanofibers of $Eu(TTA)_3Phen$ complex cannot be directly obtained by electrospinning without the use of polymers. Polymer nanofibers do not emit light without lanthanide complexes mixed with polymers. Therefore, there is the need of composites of both categories to have fibers in nanoscale and light emission. Use of polymer not only as a carrier but it helps to

enhance luminescent properties of material. The enhancement of luminescent efficiencies in Eu(TTA)$_3$Phen/Polymer occurs as uniform distribution of the complex units along macromolecular chains of polymers. In present work PS, PMMA, PVDF with their blends are used as matrix material for observing the good coordination between Eu(TTA)$_3$Phen complex and polymer so as to get enhanced luminescent fibers for fabric designing in the textile industries.

9.2 Experimental

9.2.1 Preparation of Eu(TTA)$_3$Phen Complex

Eu(TTA)$_3$Phen complex powder was prepared by simple solution method [5]. TTA (6.63 mmol, 1.4725 g) and phen (2.21 mmol, 0.3979 g) were dissolved in 20 ml of ethanol in flask. This solution neutralized with NaOH solution to obtained pH = 7. In another flask europium chloride salt $EuCl_3$ (2.21 mmol, 0.5708 g) was dissolved in 10 mL of double distilled water. Prepared solution was poured into the solution of TTA and phen. Finally, prepared solution was heated at 60 °C with continuous stirring for 1 h for obtaining homogenous solution. After 1 h precipitate of solution was formed and it was separated by using filter paper. The color of obtained compound was off-white which was then dried in oven at 80 °C for 2 h.

9.2.2 Preparation of Eu(TTA)$_3$Phen/Polymer Blend Solutions

Preparation of electrospinning solution of Eu(TTA)$_3$Phen/PVDF-PS composites, 1 g PVDF and 1 g PS were dissolved in 10 mL THF (tetrahydrofuran) solvent in one flask for obtained mass fraction of 20 wt%. Obtained mixture was magnetically stirred for 12 h till becoming uniform solution. Then 20% of Eu(TTA)$_3$Phen was added to above uniform solution of polymer and again magnetically stirred for 12 h. Now solution is ready for electrospinning process for preparation of nanofibers. The same process was repeated for preparation of electrospinning solution of Eu(TTA)$_3$Phen/PVDF-PMMA blend.

9.2.3 Preparation of Eu(TTA)$_3$Phen/Polymer Blend Nanofibers

The prepared uniform electrospinning solution of Eu(TTA)$_3$Phen/PVDF-PS blend was firstly filled into a 5 mL plastic syringe for preparation of nanofibers by electrospinning method. For the electrospinning process, prepared solution was fed to the tip using a syringe pump and adjust flow rate of 0.3 mL/h. A positive voltage of 25 kV was applied to the needle of the syringe that containing electrospinning solution. Metallic plate wrapped with aluminum foil and connected with grounded electrode. Distance between needle of the syringe and metallic plate must kept at a distance of 15 cm. The uniform electrospun nanofibers were collected on the conducting aluminum foil. After electrospinning process, collected membranes of nanofibers on aluminum foil were dried in a vacuum oven at 60 °C for 12 h so that to eliminate the residual organic solvent present with nanofibers. Same electrospinning method was repeated for another electrospinning solution of Eu(TTA)$_3$Phen/PVDF-PMMA polymer blend.

9.3 Results and Discussion

9.3.1 Scanning Electron Microscopy

Surface morphological and structural properties of prepared nanofibers of different composites by electrospinning method can be studied by SEM (scanning electron microscopy). It examines the surface information of the materials and a detailed study of the morphological features like diameter of fibers, their length, and alignment etc. of all the samples had been carried. SEM study of synthesized nanofibers is important since they directly affect the photoluminescence emission intensity of the materials. As compare with nanofibers of pure polymer, diameter of Eu(TTA)$_3$Phen/polymer blends are found to be smaller, this may be due to effect of increased conductivity of the electrospinning solution as addition of Eu(TTA)$_3$Phen in pure polymer solutions. With addition of Eu(TTA)$_3$Phen in pure polymer solutions, europium complex uniformly distributed along macromolecular chain of the polymers and it helps to increase conductivity of electrospinning solution which results to decrease diameter of nanofibers of Eu(TTA)$_3$Phen/polymer blends. The presence of europium complex into the polymer matrix can efficiently recover the morphology of the electrospinning fibers. Such Eu(TTA)$_3$Phen/Polymer blend nanofibers show more photoluminescence intensity as compared to nanofibers of pure Eu(TTA)$_3$Phen complex, Increased in intensity of Eu(TTA)$_3$Phen/Polymer blend nanofibers which may be due to their large surface area and small diameter as they show high aspect ratio that confirmed from their SEM images.

SEM images of Eu(TTA)$_3$Phen/PVDF-PS blend electrospun nanofibers shows diameters in the range of 300 to 700 nm and Eu(TTA)$_3$Phen/PVDF-PMMA blend

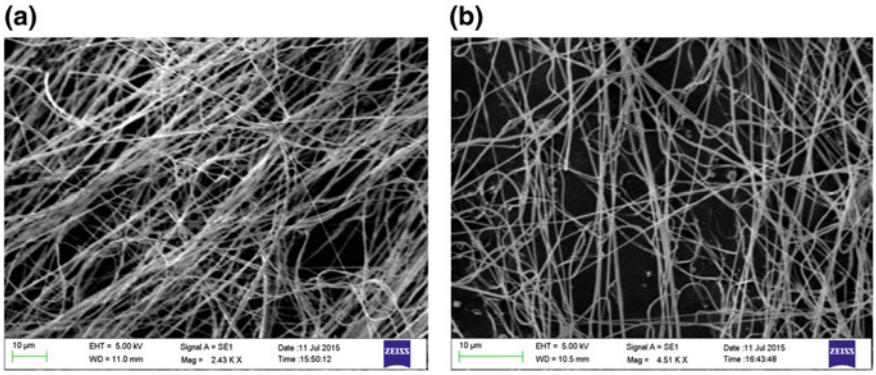

Fig. 9.1 SEM images of **a** Eu(TTA)$_3$Phen/PVDF-PS blend and **b** Eu(TTA)$_3$Phen/PVDF-PMMA blend nanofibers

electrospun nanofibers shows diameters in the range of 100 to 500 nm as respectively shown in Fig. 9.1a, b. Obtained nanofibers of Eu(TTA)$_3$Phen/polymer blends are aligned in random orientation on the collector, which was occurred by the bending instability of the spinning jet and stationary collector [6, 7].

9.3.2 FTIR Spectroscopy

FTIR spectra of Eu(TTA)$_3$Phen/PVDF-PS blend and Eu(TTA)$_3$Phen/PVDF-PMMA blend nanofibers are shown in Fig. 9.2. In the spectrum of Eu(TTA)$_3$Phen/PVDF-PS blend there are presence of bands of PS and PVDF with europium complex. FTIR spectra shows bands of PS which are shifted from its original position to slightly higher frequencies at 756, 1450, 1492 and 1602 cm^{-1}, shows the vibrations of the benzenoid ring in PS and one extra broad band appeared at 3400 cm^{-1} arises by the vibration of hydroxyl groups of PS [8]. FTIR spectra shows the bands of stretching vibration of the C=O group at 1185 cm^{-1} which are characteristic peak of PVDF, which shows a little shift to the higher frequencies as compared with pure PVDF spectra. These shifting of bands for PS and PVDF in Eu(TTA)$_3$Phen/polymers blends occur due to coordination of europium complex with PS and PVDF polymer matrix [9]. The vibration peaks of Eu(TTA)$_3$Phen complex also get shifted to higher frequencies due to the surrounding polymer matrix. In FTIR spectrum of Eu(TTA)$_3$Phen/PVDF-PMMA polymer blends, there are presence of characteristic bands of PMMA and PVDF at 1724 cm^{-1} and 1185 cm^{-1} respectively, at higher frequency region with some bands of Eu(TTA)$_3$Phen complex [10]. These shifting of bands from its positions, show that the europium complexes are effectively incorporated into polymer blend matrix.

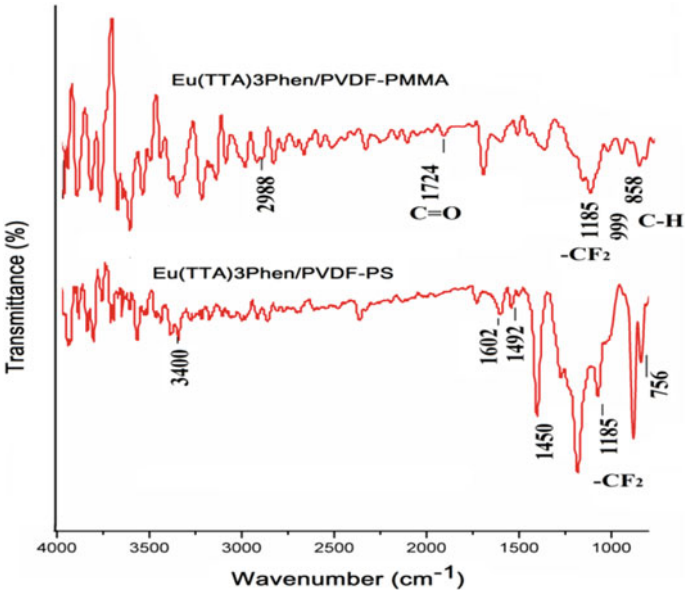

Fig. 9.2 FTIR spectra of $Eu(TTA)_3Phen$/PVDF-PS blend and $Eu(TTA)_3Phen$/PVDF-PMMA blend nanofibers

9.3.3 X-Ray Diffraction

Figure 9.3 shows X-ray diffraction patterns of $Eu(TTA)_3Phen$/PVDF-PS blend and $Eu(TTA)_3Phen$/PVDF-PMMA blend nanofibers. In XRD pattern of $Eu(TTA)_3Phen$/Polymer blends, there are diffraction peaks of PMMA, PVDF and PS exist. Diffraction peaks shows the maximum sharp peak intensity for polymer/polymer blends as europium complex Eu(TTA)/phen doped in polymer blend matrix which results a maximum degree of crystallinity due to increasing degree of ordering of atoms at polymer blend, means that the crystal structure remained constant [11]. X-ray diffraction patterns also shows a sharp peak of europium complex in $Eu(TTA)_3Phen$/polymer blend, it represented that chemical bonding exist between polymers and europium complex. There are small corresponding diffraction peaks at $2\theta = 15°–58°$ of europium observed. Presence of all these peaks of europium complex in XRD pattern of $Eu(TTA)_3Phen$/Polymer blends, indicates the development of a solid solution of $Eu(TTA)_3Phen$ in polymer blend matrix.

9.3.4 Photoluminescence

The emission spectra of europium complex $Eu(TTA)_3Phen$, $Eu(TTA)_3Phen$/PVDF-PS blend and $Eu(TTA)_3Phen$/PVDF-PMMA blend electrospun nanofibers are shown

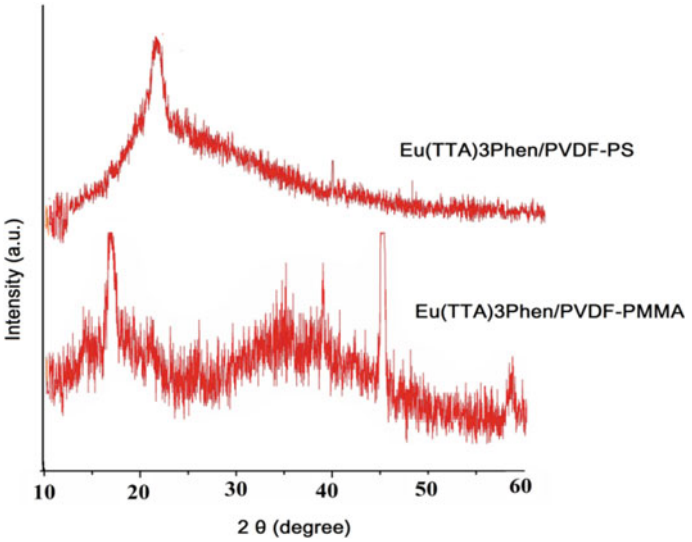

Fig. 9.3 XRD patterns of Eu(TTA)$_3$Phen/PVDF-PS and Eu(TTA)$_3$Phen/PVDF-PMMA nanofibers

in Fig. 9.4. Under excitation at 354 nm, emission spectrum of Eu(TTA)$_3$Phen was extended from 550 to 655 nm [12]. The emission spectrum shows four emission peaks at 579, 592, 612, 642, 654 nm, for the transitions $^5D_0 \rightarrow {}^7F_0$,$^5D_0 \rightarrow {}^7F_1$, $^5D_0 \rightarrow {}^7F_2$, $^5D_0 \rightarrow {}^7F_3$, $^5D_0 \rightarrow {}^7F_4$ respectively. These transitions can be characteristically the f–f transitions of Eu^{3+} ions in the europium complex. The transition $^5D_0 \rightarrow {}^7F_1$ is a magnetic dipole transition, it allowed by the Laporte selection rule. The intensity of $^5D_0 \rightarrow {}^7F_1$ transition are very weak as it is unaffected by the influence of surrounding material environment. The lower transitions $^5D_0 \rightarrow {}^7F_0$ and $^7F_3$ are forbidden transitions and its intensities not change with external change in surrounding materials. The transition $^5D_0 \rightarrow {}^7F_2$ called as hypersensitive transition and its emission intensity strongly influenced by surrounding polymer matrix as well as local

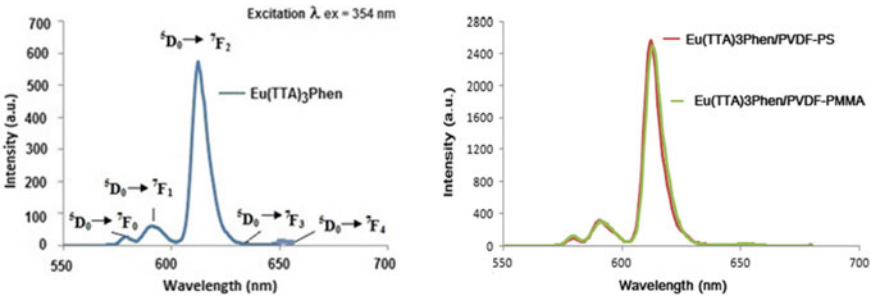

Fig. 9.4 Emission spectra of Eu(TTA)$_3$Phen complex, Eu(TTA)$_3$Phen/PVDF-PS and Eu(TTA)$_3$Phen/PVDF-PMMA nanofibers

symmetry of the europium ions of the complex and nature of ligands. The emission spectra of $Eu(TTA)_3Phen$/PVDF-PS blend and $Eu(TTA)_3Phen$/PVDF-PMMA blend electrospun nanofibers shows much stronger intensity of hypersensitive transition $^5D_0 \rightarrow {}^7F_2$ than hypersensitive transition of $Eu(TTA)_3Phen$ complex, indicates that Eu^{3+} ion is in a single site without a center of inversion and presence of surrounding polymer matrix region around the europium complex which influenced the chemical environment around the Eu^{3+} ions due to this, higher probability for the electronic dipole allowed transitions which leads to increased hypersensitive transition rate and varies its intensity [13–19]. Hypersensitive transition are intraconfigurational electric dipole transitions which are initially forbidden by the Laporte selection rule but when a europium ions of europium complex conjugated to a chemical complex of $Eu(TTA)_3Phen$, the Eu^{3+} ion commencing is in a coordinating environment and the forbidden transitions changes into partly allowed.

As compare with hypersensitive intensity of $Eu(TTA)_3Phen$ complex, intensity of $Eu(TTA)_3Phen$/PVDF-PS and $Eu(TTA)_3Phen$/PVDF-PMMA blends are much high, due to the presence of PVDF in both polymer blends. Increased in intensity of $Eu(TTA)_3Phen$/Polymer blend nanofibers which may be due to their large surface area and small diameter as they show high aspect ratio that confirmed from their SEM images study. The enhancement of luminescent efficiencies in $Eu(TTA)_3Phen$/Polymer blend occurs as there uniform distribution of the complex units along macromolecular chains of polymer matrix.

The CIE (Commission Internationale de l' Eclairage) color model is used to study emission intensity in terms of intensity of color emitted during transitions. This study used coordinates system. The coordinates of the $Eu(TTA)_3Phen$ complex, $Eu(TTA)_3Phen$/PVDF-PS and $Eu(TTA)_3Phen$/PVDF-PMMA nanofibers were obtained by color calculator software of CIE using PL emission data of each sample. The CIE coordinates calculated for $Eu(TTA)_3Phen$ complex shows red emission in visible region with coordinates $x = 0.61$, $y = 0.32$ shown in Fig. 9.5a.

Figure 9.5b, c show CIE calculated coordinates for $Eu(TTA)_3Phen$/PVDF-PS and $Eu(TTA)_3Phen$/PVDF-PMMA, respectively. For $Eu(TTA)_3Phen$/PVDF-PS CIE coordinates are $x = 0.64$, $y = 0.33$ and for $Eu(TTA)_3Phen$/PVDF-PMMA CIE coordinates are $x = 0.64$, $y = 0.34$. As addition of polymers PS and PVDF into pure $Eu(TTA)_3Phen$ complex, CIE results shows slightly change in coordinates with position of color in CIE graph. CIE coordinates for $Eu(TTA)_3Phen$/PVDF-PS and $Eu(TTA)_3Phen$/PVDF-PMMA deviated from its original position as in europium complex and it shows good red color saturation. The calculated CIE shows good color saturation for red emission. As europium complex is integrated with polymers matrix, the emission intensity of hypersensitive transitions increased and the CIE color coordinates for its moves towards pure or deep saturated red emission region. The CIE calculated color coordinates for europium complex showed red color region and for europium complex incorporated polymer matrix showed deep saturated red emission region.

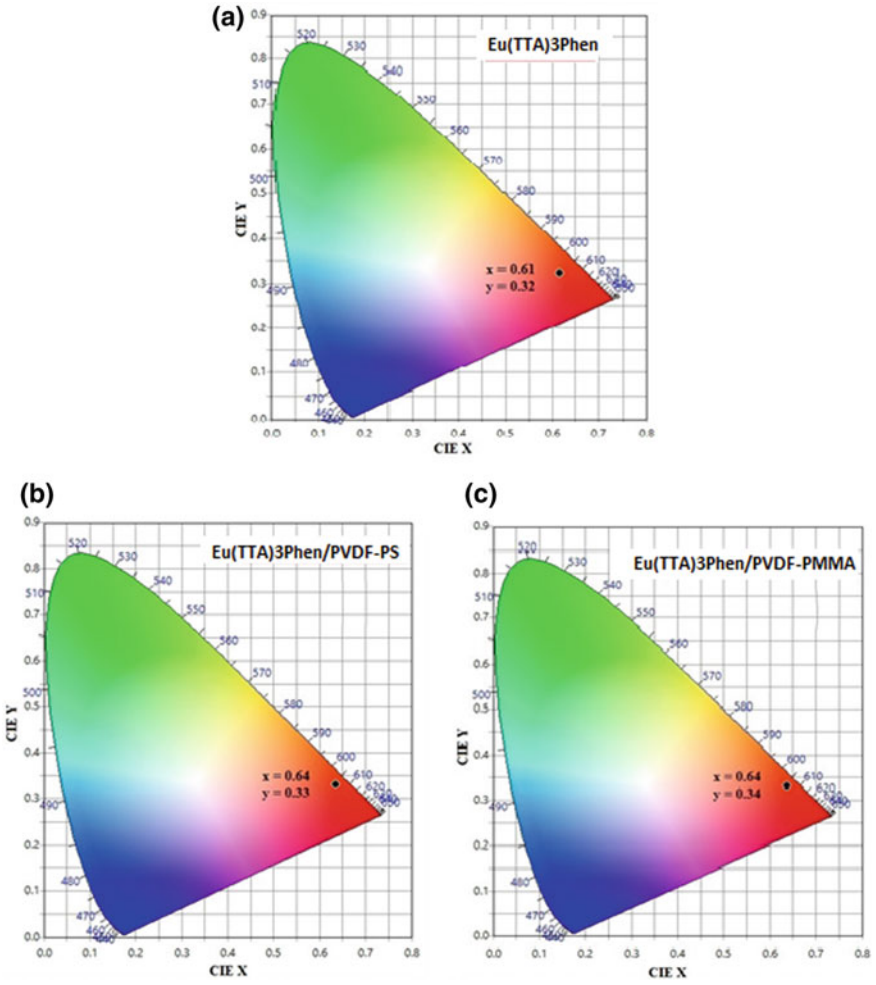

Fig. 9.5 CIE chromaticity coordinates for **a** Eu(TTA)$_3$Phen, **b** Eu(TTA)$_3$Phen/PVDF-PS and **c** Eu(TTA)$_3$Phen/PVDF-PMMA

9.4 Conclusion

Eu(TTA)$_3$Phen/PVDF-PS blend and Eu(TTA)$_3$Phen/PVDF-PS blend nanofibers with diameters in nano range were prepared by electrospinning process. Due to the addition of Eu(TTA)$_3$Phen complex into the polymer matrix and successive distortion of the symmetry around the Eu^{3+} ions by the chapping Polymer, the polarization of the Eu^{3+} ions was improved, which increased the probability for electronic dipole allowed transitions. As increased in electronic dipole allowed transitions there were

increased in intensity of hypersensitive transition. Addition of $Eu(TTA)_3Phen$ complex in polymers generally enhances the luminescent intensity as compared to pure europium complex $Eu(TTA)_3Phen$. Polymers like PS, PMMA and PVDF generally increases the luminescent intensity of the $^5D_0 \rightarrow {}^7F_2$ hypersensitive transition of Eu^{3+} ions. As compare with hypersensitive intensity of $Eu(TTA)_3Phen$ complex, intensity of $Eu(TTA)_3Phen$/PVDF-PS and $Eu(TTA)_3Phen$/PVDF-PMMA blends are much high, due to the presence of PVDF in both polymer blends. Nanofibers of $Eu(TTA)_3Phen$/polymer blends shows large surface area and small diameter as they represents high aspect ratio that confirmed from their SEM images. As $Eu(TTA)_3Phen$/PVDF-PS and $Eu(TTA)_3Phen$/PVDF-PMMA blend nanfibers shows good morphology and excellent luminescent property, it could be applied for the designing of photoluminescent smart fabric.

Acknowledgements The Department of Science and Technology (DST, New Delhi, India) supports this work under DST-FIST Program, Grant No. SR/FST/PSI-178/2012(C).

References

1. X. Cui, H. Ming, T. Zhang, W. Feng, Electrospinning preparation and photoluminescence properties of erbium complex doped composite fibers. Spectrochim. Acta Part A **79**, 1998–2002 (2011)
2. B. Rajamouli, C.S. Dwaraka Viswanath, S. Giri, C.K. Jayasankar, V. Sivakumar, Carbazole functionalized new bipolar ligand for monochromatic red light-emitting europium(III) Complex: combined experimental and theoretical study. New J. Chem. **41**, 3112–3123 (2017)
3. J. Feng, H. Zhang, Hybrid materials based on lanthanide organic complexes: a review. J. Chem. Soc. Rev. **42**, 387–410 (2013)
4. K. Binnemans, P. Lenaerts, K. Driesen, C. Gorller-Walrand, A luminescent tris(2-thenoyltrifluoroacetonato) europium(III) complex covalently linked to a 1,10-phenanthrolinefunctionalised sol–gel glass. J. Mater. Chem. **14**, 191–219 (2004)
5. L.R. Melby, N.J. Rose, E. Abrmson, J.C. Caris, Synthesis and fluorescence of some trivalent lanthanide complexes. J. Am. Chem. Soc. **86**, 5117–5128 (1964)
6. C. Chang, C. Huang, Y. Chang, C. Kuo, Enhancement of light scattering and photoluminescence in electrospun polymer nanofibers. J. Opt. Express A. **18**, 174–189 (2010)
7. X. Zhang, S. Wen, S. Hu, Q. Chen, H. Fong, L. Zhang, L. Liu, Luminescence properties of Eu(III) complex/polyvinylpyrrolidone electrospun composite nanofibers. J. Phys. Chem. C **114**, 3898–3903 (2010)
8. Y. Hongquan, L. Tao, C. Baojiu, W. Yanbo, L. Yue, Preparation of aligned $Eu(DBM)_3$phen/PS fibers by electrospinning and their luminescence properties. J. Colloid Interface Sci. **8**, 23–56 (2013)
9. N. Betz, L. Moel, E. Balanzat, J.M. Ramillon, J. Lamotte, FTIR study of PVDF irradiated by means of swift heavy ions. Polym. Sci. Part. J Polym. Phys. **32**, 1493–1502 (1994)
10. J. Kai, C. Maria, C. Felinto, A. Luiz, O. Nunes, L. Oscar, Intermolecular energy transfer and photostability of luminescence-tuneable multicolour pmma films doped with lanthanide β-diketonate complexes, supplementary material (ESI) for journal of materials chemistry. J. Roy. Soc. Chem. **5**, 123–156 (2011)
11. Y. Li, C. Zhang, D. Yu, X. Wang, Tailoring spatial distribution of Eu(TTA)3phen within electrospun polyacrylonitrile nanofibers for high fluorescence efficiency. J. RSC Adv. **87**, 548–568 (2016)

12. Z. Xiaoping, W. Shipeng, H. Shui, Z. Liqun, L. Li, Electrospinning preparation and luminescence properties of Eu(TTA)3phen/polystyrene composite nanofibers. J. Rare Earths **28**, 332–337 (2010)
13. A. Sharma, D. Singh, I. Singh, Synthesis and characterization of optical properties of europium (III) complex with 4,4,4-trifluoro-1-phenyl-1,3-butanedione and 1,10 Phenanthroline. Proc. of ASID New Delhi **5**, 862–945 (2006)
14. L.V. Rosa, A. Paula, A. Marques, T.S. Tanaka, V. Motta, A. Varela, R. Leite, Europium(III) concentration effect on the spectroscopic and photoluminescent properties of BaMoO4:Eu. J. Fluoresce. **19**, 495–500 (2009)
15. A. Zhang, N. Sun, L. Liping, Y. Yamin, Z. Xijin, J. Husheng, L. Xuguang, X. Bingshe, Tunable white light emission of Eu, Tb, Zn-containing copolymers by RAFT polymerization. J. Mater. Chem. C. **3**, 9933–9941 (2015)
16. D. Chitnis, N. Thejo Kalyani, S.J. Dhoble, Structural and optical investigation of novel europium hybrid organic complex for OLEDs and solid state lighting. J. Mater. Phys. Chem. **5**, 1–10 (2017)
17. H. Shao, Q. Ma, X. Dong, W. Yu, M. Yang, Y. Yang, J. Wang, G. Liu, Electrospun flexible coaxial nanoribbons endowed with tuned and simultaneous fluorescent color-electricity-magnetism trifunctionality. Art. Sci. Rep. **8**, 10452–10486 (2015)
18. S. Corneliu, S. Stan, P. Horlescu, M. Popa, A. Coroabab, L. Laura, E. Ursub, Photoluminescent polymer composites with R, G, B emission and their potential applications in LCD displays. New J. Chem. **40**, 6505–6512 (2016)
19. S.L. Sonawane, S.K. Asha, Blue, green, and orange-red emission from polystyrene microbeads for solid-state white-light and multicolor emission. J. Phys. Chem. B. **118**, 9467–9475 (2014)

Chapter 10
Influence of Polymer in Photoluminescence Properties of Electrospun Eu^{3+} Doped Polymer Nanofibers

Sangeeta G. Itankar, Manjusha P. Dandekar, Pankaj M. Koinkar and Subhash B. Kondawar

Abstract Eu^{3+} doped polymer nanofibers were fabricated by electrospinning technique using various polymers such as poly(vinylidene fluoride) (PVDF), polyethylene oxide (PEO), poly(vinyl pyrrolidone) (PVP) to study the influence of polymer in their photoluminescence properties. As-fabricated nanofibers were characterized by scanning electron microscopy (SEM), energy dispersive spectroscopy (EDX) and photoluminescence (PL). Spectral analysis of Polymer/Eu^{3+} nanofibers was based on their emission spectra. The photoluminescence property shows superior bright red emission spectra from the Eu^{3+} and relatively stronger hypersensitive behavior of the $^5D_0 \rightarrow {}^7F_2$ transition. Eu^{3+} doped polymeric nanofibers are very much suitable for photoluminescent fabric designing in smart textiles. The enhanced properties of this photoluminescence indicated a more polarized chemical environment for the Eu^{3+} ions and greater hypersensitivity for the $^5D_0 \rightarrow {}^7F_2$ transition, which showed the potential for application in various polymer optoelectronic devices.

10.1 Introduction

Photoluminescent materials are the products which glow in the dark like photoluminescent paint, exit sign stickers which are used in offices, cinema halls which are helpful in power failure situation or used as safety purposes. Photoluminescent thread which embroidered on the clothes attracts more attention as compared to ordinary clothes. Apart from these, photoluminescence spectroscopy is of great significance in other fields of analysis, especially semiconductors in band gap determination, impurity levels and defect detection, recombination mechanisms, surface structure and excited states. Currently, functional and practical applications of this physical phenomenon in our daily life can be found in light-emitting diodes, lasers, lamps, solar

S. G. Itankar · M. P. Dandekar · S. B. Kondawar (✉)
Department of Physics, Rashtrasant Tukadoji Maharaj Nagpur University, Nagpur, India
e-mail: sbkondawar@yahoo.co.in

P. M. Koinkar
Department of Optical Science, Tokushima University, Tokushima, Japan

R.-I. Murakami et al. (eds.), *NAC 2019*, Springer Proceedings in Physics 242,
https://doi.org/10.1007/978-981-15-2294-9_10

cells, sensors, scintillates, electronic displays, etc. Photoluminescence spectroscopy is a widely used technique for characterization of the optical and electronic properties of semiconductors and molecules. Now a day these photoluminescent materials are specially used in designing fabric and in military purposes also. But all this is possible only because of rare earth ions, which are highly, valued for their unique properties, especially as optically active material in ionized state for lasers.

Among all the rare earth (RE) ions, the material Eu^{3+} is selected because europium metal ions exhibit a high yield of luminescence in the visible light region and extremely sharp emission bands due to their 4f electrons well shielded by closed 5s and 5p outer shells. The energy levels of the 4f shell have equal parity and hence electric dipole transitions are forbidden. RE ions can transform their absorption energy from the shorter wavelength region into luminescence energy in the longer wavelength region with high luminosity. The material Eu^{3+} is one of the most attractive rare earth ions due to its excellent luminescence properties that originate from the 4f–4f transition. Europium is used in the printing of euro banknotes. It glows red under UV light, and forgeries can be detected by the lack of this red glow. Europium is excellent at absorbing neutrons, making it valuable in control rods for nuclear reactors. Europium-doped plastic has been used as a laser material. It is also used in making thin super-conducting alloys. Because europium are strongly influenced by its half filed electron shell, it has second lowest melting point and it become superconductor when cooled below 1.8 K and compressed to above 80 GPa. A recent application of europium is in quantum memory chips which can reliably store information for days at a time; this could allow sensitive quantum data to be stored to a hard disk like device and shipped around. In the field of lighting, white light emitting diode (WLED), a new generation solid source has been highlighted due to its high luminous efficiency, low energy consumption and great potential in environmental protection. There is a tremendous growth in the development of WLED worldwide due to its various applications like lighting, motor vehicle and backlight for mobile panel and liquid crystal display.

To increase its optical property rare earth ions are doped with polymers. The polymer material is well recognized for its high transparency, flexible, excellent optical properties and simple synthesis process, which make the material to be perfect host for rare earth ions. The rare earth ions doped with polymers gives a new class of material which makes them applicable in wide range of new technologies. To design a fabric, new technology is used with the help of fibers made of materials at nanoscale [1–3]. These nanofibers can be easily fabricated by electrospinning method. Electrospinning is an effective and easy method for generating one dimensional nanofibers with diameter ranging from nanometer to micrometer. The electrospun nanofibers possess properties like high surface area to volume ratio, high aspect ratio (length to diameter), controlled pore size and superior mechanical performance. The superior mechanical properties associated with the electrospun nanofibers arise from the decrease in diameter that cannot be achieved through conventional spinning processes. It is a technique with which rich variety of materials such as polymers, organic, inorganic compounds can be used for fabrication of nanofibers. These photoluminescent electrospun nanofibers become the new trend in textile industry [4–7].

Electrospun polymer nanofibers have been studied for use as medical or consumer products and in industrial or high-tech applications. Electrospun carbon nanofibers prepared from PAN have been used extensively to make bullet proof military jackets because of their properties of hardness as well as bending flexibility. Similarly, by using this introduced method for nanofibers manufacture, photoluminescent fibers can be prepared as a protective textile for soldiers, or as medical textiles or smart textiles using suitable polymers. With this background, we have reported in this paper by using polymers such as poly(vinylidene fluoride) (PVDF), polyethylene oxide (PEO), poly(vinyl pyrrolidone) (PVP) for doping Eu^{3+} ions into these polymers to fabricate Eu^{3+} doped polymer nanofibers by electrospinning technique and to study the influence of these polymers in their photoluminescence properties.

10.2 Experimental

The starting material europium oxide (Eu_2O_3, 99.9%) was used as received without further purification for the preparation of europium ion doped polymer nanofibers. $EuCl_3$ solution was prepared by dissolving the corresponding europium oxide (Eu_2O_3) in a dilute hydrochloric acid solution and stirring at 100 °C. During heating excess HCl was evaporated. $EuCl_3$ powder was obtained after drying under vacuum [8]. For the preparation of PVDF/Eu^{3+} nanofibers by electrospinning, PVDF solution was prepared by using 1 g of PVDF (Mw = 40,000) powder in 10 mL N, *N*-dimethylformadide (DMF). Then solution was stirred for 5 h at room temperature. $EuCl_3$ (0.5 g) was dissolved in the PVDF solution and rigorously stirred for 12 h at room temperature for homogenous mixing to obtain $EuCl_3$/PVDF solution with 1:2 concentration. $EuCl_3$/PVDF solution was then loaded into a syringe for electrospinning. The physical parameters of electrospinning were set by high voltage 17 kV between the needle of syringe and the grounded collector (aluminum foil) placed at a distance of 20 cm from needle. The solution flow rate was kept at 0.4 mL/h and maintained using computer control programming. PVDF/Eu^{3+} nanofibers were collected after 10 h and then dried in vacuum oven at 80 °C [9–11]. Then same procedure was repeated for the preparation of PEO/Eu^{3+} and PVP/Eu^{3+} nanofibers by electrospinning technique. Figure 10.1 shows the synthesis process for preparation of polymer/Eu^{3+} nanofibers. As-synthesized electrospun nanofibers were characterized by using Scanning Electron Microscopy (SEM) and Energy Dispersive X-ray spectroscopy (EDX) performed on Carl Zeiss EVO-18 SEM-EDX and photoluminescence spectra were recorded on FP8200 spectrophotometer.

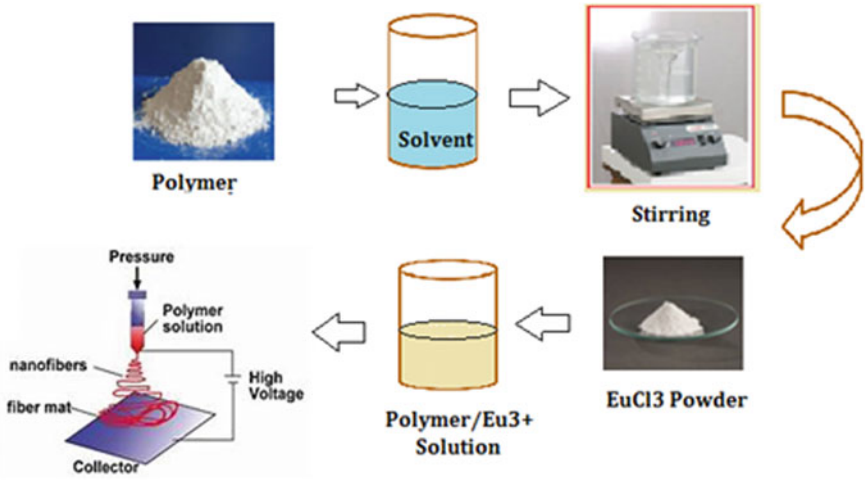

Fig. 10.1 Synthesis process for preparation of polymer/Eu^{3+} nanofibers

10.3 Results and Discussion

10.3.1 Scanning Electron Microscopy (SEM) and Energy Dispersive X-Ray Spectroscopy (EDX)

SEM images and histogram of PVDF/Eu^{3+}, PEO/Eu^{3+} and PVP/Eu^{3+} nanofibers are shown in Fig. 10.2a–c respectively. The diameter of the nanofibers was found to be 1200 nm, 672 nm and 584 nm for PVDF/Eu^{3+}, PEO/Eu^{3+} and PVP/Eu^{3+} nanofibers respectively. All SEM images are having different magnification as these images have been provided by SEM user. However, with the help of histograms of as-synthesized electrospun nanofibers the average diameter can be obtained as mentioned. From SEM results, it is seen that PVP/Eu^{3+} electrospun nanofibers are very smooth, fine and smaller in diameter as compared to the nanofibers of PVDF/Eu^{3+} and PEO/Eu^{3+}. This may be due to strong interaction between the polymer molecule chains of PVP and Eu^{3+} ions which avoids the formation of beads in nanofibers as demonstrated by Tang et al. [5]. These results are possible because PVP is good solvents i.e. it is soluble in various alcohols, such as methanol and ethanol. It has bearing active C=O groups, which made PVP to be able to use as carrier for preparation of many composite functional materials. If C=O groups of PVP coordinate with Eu^{3+} ions, it would influence the coordinative environment of the Eu^{3+} ions and change the energy transfer probabilities of the electric dipole transitions. PEO and PVDF are also water-soluble polymers heat resistance, resistance to chemical corrosion and low protein binding with high thermal stability with semi-crystalline nature because of that there may not be as good as interaction and hence having larger diameter [12].

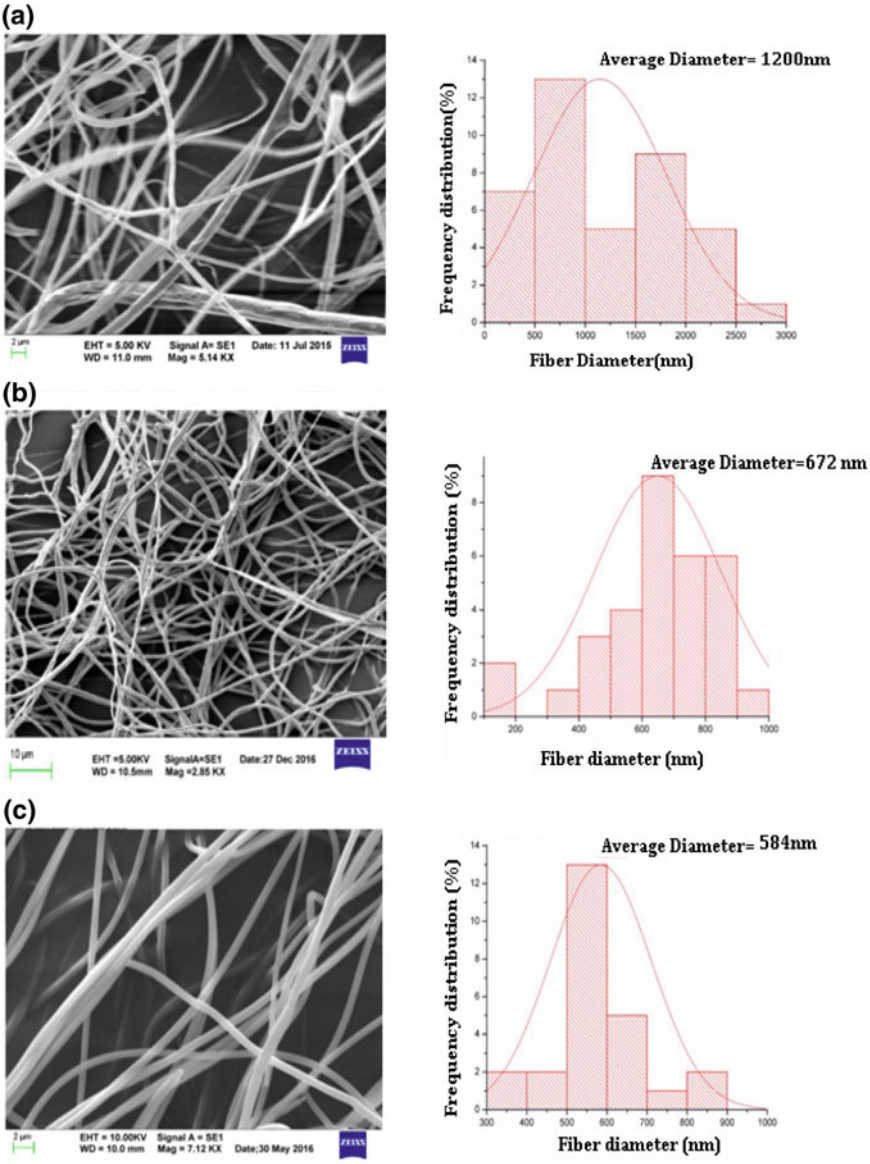

Fig. 10.2 **a** SEM image and histogram of PVDF/Eu^{3+} nanofibers, **b** SEM image and histogram of PEO/Eu^{3+} nanofibers, **c** SEM image and histogram of PVP/Eu^{3+} nanofibers

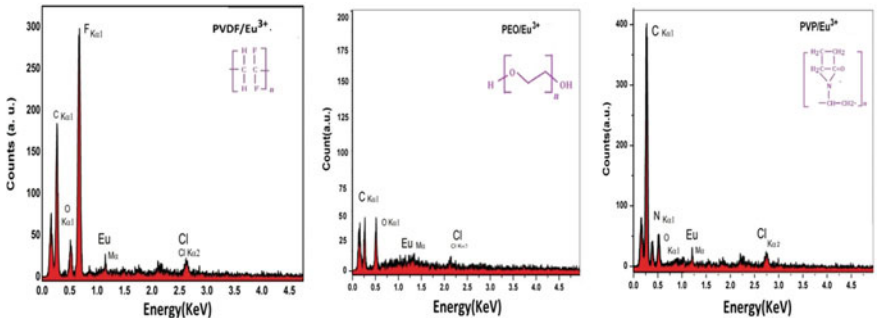

Fig. 10.3 EDX spectra of PVDF/Eu^{3+}, PEO/Eu^{3+}, PVP/Eu^{3+} nanofibers

Figure 10.3 shows EDX spectra of PVDF/Eu^{3+}, PEO/Eu^{3+} and PVP/Eu^{3+} nanofibers, which indicates the peak for element Eu confirming its existence in the prepared PVDF/Eu^{3+}, PEO/Eu^{3+}, PVP/Eu^{3+}nanofibers. PVDF/Eu^{3+} contain maximum concentrations of the elements like fluorine and carbon indicates their presence due to PVDF polymer. In PEO/Eu^{3+} nanofibers, peaks of carbon, oxygen, europium and chlorine are observed along with the peak for element Eu confirming its existence in PEO/Eu^{3+} nanofibers. From the EDX spectrum PVP/Eu^{3+}, the europium peak can be detected confirming its existence in PVP/Eu^{3+}. Hence when Eu^{3+} ions are doped in the polymer PVP the peaks of Europium and chlorine are clearly visible, along with the contents carbon and nitrogen of PVP.

10.3.2 Photoluminescence

The excitation of all synthesized Eu^{3+} doped polymer nanofibers was registered at room temperature by monitoring the luminescence intensity of the $^5D_0 \rightarrow {}^7F_2$ transition at 615 nm. Figure 10.4a shows the excitation and emission spectra of PVDF/Eu^{3+} nanofibers. It is observed that the nanofibers exhibit an intense broad excitation band at 411 nm. In the emission spectra of PVDF/Eu^{3+} nanofibers, sharp peak at around 615 nm is assigned due to $^5D_0 \rightarrow {}^7F_2$ electric dipole transition [8, 13, 14]. The $^5D_0 \rightarrow {}^7F_2$ transition is responsible for the typical red luminescence observed in europium (III).

Figure 10.4b shows the excitation and emission spectra of PEO/Eu^{3+} nanofibers. It is observed that the nanofibers exhibit an intense broad excitation band at 411 nm. In emission spectra, peaks at around 592 and 613 nm are assigned to $^5D_0 \rightarrow {}^7F_J$ transition (J = 1, 2) respectively. The $^5D_0 \rightarrow {}^7F_2$ transition is a called as "hypersensitive transition" (electric dipole transitions). Transition $^5D_0 \rightarrow {}^7F_2$ shows a very high intense peak at 613 nm. Hyper-sensitive transitions obey the selection rules $|S| = 0$, $|L| \leq 2$ and $|J| \leq 2$ which are same as the selection rules for a quadrupole transition. The intensity of the hypersensitive transition $^5D_0 \rightarrow {}^7F_2$ is often used as

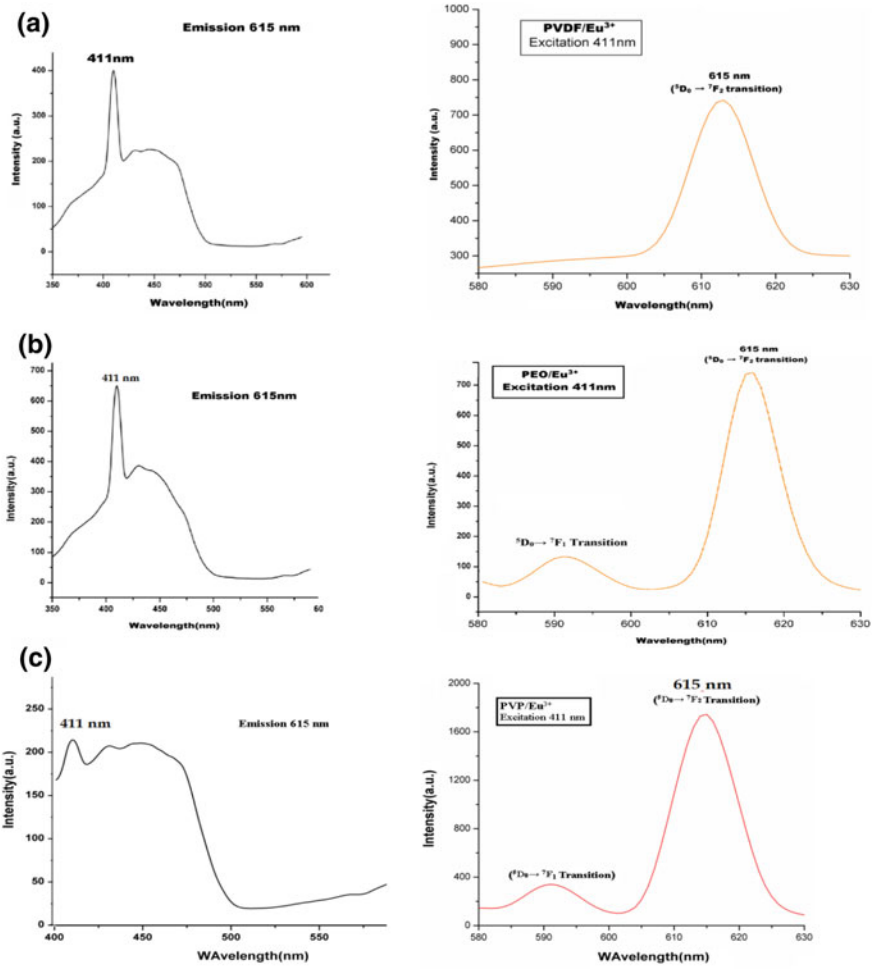

Fig. 10.4 **a** Excitation and emission spectra of PVDF/Eu^{3+} nanofibers, **b** excitation and emission spectra of PEO/Eu^{3+} nanofibers, **c** excitation and emission spectra of PVP/Eu^{3+} nanofibers

a measure for the asymmetry of the Eu^{3+} site i.e. intensity is much more affected by the environment of Eu^{3+} ions. Another peak is because of $^5D_0 \rightarrow {}^7F_1$ transition called as magnetic dipole transitions. Laporte selection rule is only applicable for this type of transition. The intensity of magnetic dipole transition is very weak as compared to electric dipole transitions. The weak emission intensity of $^5D_0 \rightarrow {}^7F_1$ transition at 592 nm is because of independent of the coordination environment of the Eu^{3+} [15]. Figure 10.4c shows the excitation and emission spectra of PVP/Eu^{3+} nanofibers. Transition $^5D_0 \rightarrow {}^7F_2$ shows a very high intense peak at 615 nm. Intensity is much more affected by the environment of Eu^{3+} ions. It is observed that the intensity of PVP/Eu^{3+} nanofibers is greater than the other polymer nanofibers. It

may be due to the smaller the range of nanofibers higher will be the surface area of PVP/Eu^{3+} nanofibers, so that more emission centers Eu^{3+} could be excited. And hence the intensity of PVP/Eu^{3+} nanofibers had a significant increase [16, 17]. It is observed that when europium ion is doped with polymers the intensity of emitting light increased because of the well homogeneous distribution of the Eu^{3+} ions with the polymers as well as high surface area of the nanofibers due to which more emission centres could be excited. So, the emission intensity of the nanofibers had a significant increase [18].

Photoluminescence (PL) spectra of all synthesized Eu^{3+} doped polymer nanofiber s were further qualitative analysed by Judd-Ofelt theory for the study of f–f inner shell electronic transitions and its intensity parameters [19]. Judd-Ofelt intensity parameters for transitions are denoted by Ω_λ ($\lambda = 2$, 4 and 6) which are obtained from emission data of electronic transitions $^5D_0 \rightarrow {}^7F_2$, $^5D_0 \rightarrow {}^7F_4$ and $^5D_0 \rightarrow {}^7F_6$ respectively. Judd-Ofelt intensity parameters (Ω_λ) are important for the investigation of local structure and bonding in the vicinity of rare earth ions. A_{RAD} is the total radiative transition rate of the $^5D_0 \rightarrow {}^7F_{0\text{-}4}$ transitions. Judd-Ofelt theory is a useful tool for analyzing f–f inner shell electronic transitions. The intensity parameter (Ω_λ) gives the emission intensity of the prepared material and it can be calculated by using radiative transition rate (A_{RAD}) which are well explained by Zhang et al. [20].

From the emission spectra of Eu^{3+} doped polymer nanofibers, the experimental intensity parameters Ω_2 was determined by using the $^5D_0 \rightarrow {}^7F_2$ transition by expressing the emission intensity I_{0J} in terms of the surface 'S' under the emission curve. The radiative transition rate (A_{RAD}) emitting level $^5D_0$ was determined from intensity I_{0J} and used it for the determination of intensity parameters Ω_2 [20]. Intensity parameters Ω_2 for Eu^{3+} doped polymer nanofibers are reported in Table 10.1. It was found that the emission wavelength for all Eu^{3+} doped polymer nanofibers is nearly same as 615 nm which is the characteristics of $^5D_0 \rightarrow {}^7F_2$ transition called hypersensitive transition. The International Commission on Illumination (CIE) chromaticity coordinates of PVDF/Eu^{3+}, PEO/Eu^{3+} and PVP/Eu^{3+} nanofibers are calculated by using PL spectra and represented in Fig. 10.5. Purpose of colorimetry is to express color as numerical values and colorimetry is nothing but a technique of color measurement. The coordinates of CIE indicates that what is the actual color of the prepared materials. The location of coordinates indicates the intensity of the color. The prepared material emits red color and their coordinates indicates the less and high

Table 10.1 Judd-Ofelt intensity parameter Ω_2 and radiative transition rate A_{RAD} of Eu^{3+} doped polymer nanofibers

Polymer nanofibers	Intensity (a.u.)	Ω_2 (10^{-20} $cm^{2)}$	A_{RAD} (s^{-1})
PVDF/Eu^{3+} nanofibers	742.3	7.802	263.60
PEO/Eu^{3+} nanofibers	742.3	7.802	263.60
PVP/Eu^{3+} nanofibers	1744.0	18.337	619.48

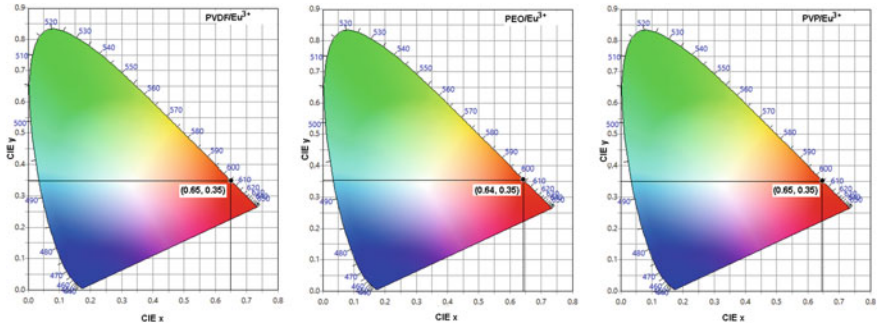

Fig. 10.5 Chromaticity diagram of PVDF/Eu^{3+}, PEO/Eu^{3+} and PVP/Eu^{3+} nanofibers

intensity of the material. If the coordinate is more towards x and less towards y then the intensity of red light emission is more. CIE values for PVDF/Eu^{3+}, PEO/Eu^{3+} and PVP/Eu^{3+}nanofibers are calculated to an average (0.65, 0.35), which is closed to the standard red chromaticity of Nation Television Standard Committee (NTSC) (x = 0.68, y = 0.32). The CIE chromaticity coordinates for these PVDF/Eu^{3+}, PEO/Eu^{3+} and PVP/Eu^{3+}nanofibers are located in the red region. It can be clearly seen from the diagram that all the nanofibers give an intense red emission due to the presence of relatively intense 615 nm lines ($^5D_0 \rightarrow {}^7F_2$) under 411 nm excitation.

10.4 Conclusion

Eu^{3+} doped polymer nanofibers were fabricated by electrospinning and comparatively studied their photoluminescence properties for fabric designing. Among all nanofibers, PVP shows good photoluminescence because Eu^{3+} ions dispersed in the PVP molecule chain and there could be some more interaction between the C=O group of PVP and Eu^{3+} ions. Due to high surface area to volume ratio and outstanding fluorescent property, Eu^{3+} doped polymer nanofibers showed potential applications in preparation of various polymer optoelectronic devices and nanofabric in textiles industries which show photoluminescent properties for making new kind of light emitting clothes.

Acknowledgements This work was supported by the Department of Science and Technology (DST, New Delhi, India) Support under DST-FIST Program, Grant No. SR/FST/PSI-178/2012(C).

References

1. H. Timothy, G. Froerer, Photoluminescence in analysis of surfaces and interfaces, in *Encyclopedia of Analytical Chemistry* (2006), pp. 9209–9239
2. V. Prajzler, V. Lyutakov, I. Hutte, J. Oswald, V. Jerabek, Optical and spectroscopic properties of polymer layers doped with rare earth ions source, in *Advances in Lasers and Electro Optics*, ed. by N. Costa, A. Cartaxo (2010). ISBN 978-953-307-088-9, p. 838
3. S. Itankar, M. Dandekar, S. Kondawar, B. Bahirwar, Eu^{3+} doped polystyrene and polyvinylidene fluoride nanofibers fabricated by electrospinning for photoluminescent fabric design. J. Luminescence **32** (2017)
4. S. Tang, C. Shao, M.R. Yichun, Electrospun nanofibers of poly(acrylonitrile)Eu^{3+} and their photoluminescent properties. J. Phys. Chem. Solids **71**, 273–278 (2010)
5. S. Tang, C. Shao, Y.C. Li, Electrospun nanofibers of poly (vinyl pyrrolidone)/Eu^{3+} and its photoluminescence properties. Chin. Chem. Lett. **18**, 465–468 (2007)
6. J. Liang, F. Xie, X. Ren, Y. Chen, B. Chen, F. Guo, Temperature dependent luminescence of a europium complex incorporated in poly(methyl methacrylate). Mol. Biomol. Spectrosc. **116**, 317–320 (2013)
7. M. Dandekar, S. Kondawar, S. Itankar, D. Nandanwar, Luminescence properties of electrospun nanofibers of europium complex Eu(TTA)3phen/polymers. Procedia Mater. Sci. **10**, 580–587 (2015)
8. X. Li, G. Shen, X. Jin, M. Liu, L. Shi, J. Lu, Novel polyimide containing 1,10-phenanthroline and its europium (III) complex: synthesis, characterization and luminescence properties. J. Mater. Sci. **51**, 2072–2078 (2016)
9. S. Tang, S. Shao, S. Li, Electrospun nanofibers of poly (vinyl pyrrolidone)/Eu^{3+} and its photoluminescence properties. Chin. Chem. Lett. **18**, 465–468 (2007)
10. S. Tang, C. Shao, Y. Liu, R. Mu, Electrospun nanofibers of poly(acrylonitrile)/Eu^{3+} and their photoluminescence properties. J. Phys. Chem. Solids **71**, 273–278 (2010)
11. Z. Zhang, Y. Long, H. Yin, B. Sun, J. Zheng, H. Zhang, X. Ji, C. Gu, Electrospun fluorescein/polymer composite nanofibers and their photoluminescent properties. Chin. Phys. B. 21, 097805-1-6 (2012)
12. S. Itankar, M. Dandekar, S. Kondawar, B. Bahirwar, Comparative photoluminescent study of PVDF/Eu^{3+} and PEO/Eu^{3+} electrospun nanofibers in photonic fabric. AIP Conf. Proc. **2104**, 1 (2019)
13. S. Itankar, M. Dandekar, S. Kondawar, B. Bahirwar, Synthesis and characterization of electrospun Eu^{3+} doped poly(methylmethacrylate) nanofibers. Int. J. Res. Biosci. Agric. Technol. **1**, 419–425 (2014)
14. M. Mondragon, G. Trujillo, I. Moggio, E. Arias, Luminescent polylactic acid and polysulfone electrospun fibers containing europium (III) complexes. Eur. Polymer J. **80**, 126–133 (2016)
15. J. Zhao, W. Zang, E. Xie, Z. Ma, A. Zhao, Z. Liu, Structure and photoluminescence of Ga2O3:Eu^{3+} nanofibers prepared by electrospinning. Appl. Surf. Sci. **275**, 4968–4972 (2011)
16. R. Argauer, C. White, Fluorescent compounds for calibration of excitation and emission unit of spectroflurometer. Anal. Chem. **36**, 368–371 (1964)
17. K. Sivaiah, S. Buddhudu, Light emission in Tb^{3+} and Eu^{3+} polymer films. Indian J. Pure Appl. Phys. **49**, 377–381 (2011)
18. L. Saravanan, S. Diwakar, R. Mohankumar, A. Pandurangan, R. Jayavel, Synthesis, structural and optical properties of PVP encapsulated CdS nanoparticles. Nanomater. Nanotechnol. **1**, 42–48 (2011)
19. Y. Tao, P. Yan, C. Wang, G. Li, Luminescent electrospun composite nanofibers of [Eu(TFI)$_3$(Phen)].CHCl$_3$/polyvinylpyrrolidone. J. Mater. Sci. **48**, 6682–6688 (2013)
20. X. Zhang, S. Wen, L. Zhang, L. Liu, Electrospinning preparation and luminescence properties of Eu(TTA)$_3$phen/polystyrene composite nanofibers. J. Rare Earths **28**, 333–338 (2010)

Part IV
Mechanical Materials

Chapter 11
The Effect of Compressed Air Pressure and Stand-off Distance on the Twin Wire Arc Spray (TWAS) Coating for Pump Impeller from AISI 304 Stainless Steel

D. F. Fitriyana, Wahyu Caesarendra, S. Nugroho, G. D. Haryadi, M. A. Herawan, M. Rizal and R. Ismail

Abstract Twin Wire Arc Spray Coating (TWAS) is thermal spraying technique that has been widely adopted in many industries due to its flexibility, and cost effectiveness in producing superior quality of coating. The demand of high-technology industries and the availability of new advanced materials have generated major advances in this field. The TWAS thermal spray process has been utilised in many industries for coating purpose on components to protect against wear, heat and corrosion, and also to build up worn components. In this study, Iron-Chrome based metal coating is used to increase the lifetime of pump impeller from AISI 304 stainless steel. The addition of nickel in the process is carried out to improve adhesive properties. A combination of NiAl and FeCrBSiMn on substrate is conducted in the experimental work to assess the coatings properties. Investigations were carried out on the effect of stand-off distance (100, 200, 300, and 400 mm) and compressed air pressure (3, 4, and 5 bar) on coating properties including coating thickness, hardness, wear resistance and bond strength (adhesive coating). The result shows that coating thickness tend to increase with increasing stand-off distance and compressed air pressure. The results reveals that there is a strong correlations between the coating thickness, hardness, wear resistance, bonding strength (adhesive coating) in coatings properties.

D. F. Fitriyana
Department of Mechanical Engineering, Semarang State University, Semarang 50229, Indonesia
e-mail: deniifa89@gmail.com

W. Caesarendra (✉) · S. Nugroho · G. D. Haryadi · M. A. Herawan · M. Rizal · R. Ismail
Department of Mechanical Engineering, Diponegoro University, Jl. Prof. Soedharto SH, Semarang 50275, Indonesia
e-mail: wahyu.caesarendra@ubd.edu.bn

W. Caesarendra
Faculty of Integrated Technologies, Universiti Brunei Darussalam, Jalan Tungku Link, Gadong BE1410, Brunei Darussalam

R.-I. Murakami et al. (eds.), *NAC 2019*, Springer Proceedings in Physics 242,
https://doi.org/10.1007/978-981-15-2294-9_11

11.1 Introduction

Irrigation and drainage are important parts of environmental engineering, especially for water engineer where the pump acts as the key equipment. The sediment concentration of the river affects the lifetime of pump components [1]. The movement of the suspense material sediment entrained by water, the hard sands with a certain kinetic energy impact and cut repeatedly the flow parts of pump machinery [2]. The existence of sand particles will cause a serious abrasion and low efficiency of moving parts, affect the service life of the pump, and also reduce the operation quality of the pump [3]. Thermal spray coating can be used to improve friction, wear resistance and lifetime of pump components [4, 5]. Thermal spraying technologies include detonation spraying (DS), high-velocity oxygen-fuel (HVOF) spraying, plasma spraying (PS), and twin wires arc spraying (TWAS). TWAS coating method was utilized because it is one of the most cost-effective coating processes with high efficiency and has been proven to be applicable in high volume productions [6, 7].

The Twin Wire Arc process is a common commercial thermal spray process. A Twin Wire Arc coating is applied using a spray torch, which brings two electrically energized feed stock wires together. When the wires cross, an arc—similar to a welding arc—forms between the wire tips and causes them to melt. A gas stream injected behind the arcing wire tips atomizes the molten feed stock material and propels it downstream. When molten droplets of the feed stock material encounter the substrate the droplets flatten, solidify, and form a coating containing the characteristic lamellar structure associated with thermal sprayed materials [8]. The wire arc spray process is shown schematically in Fig. 11.1 [9]. Many researches were reported on twin wires arc sprayed coatings.

Zhou et al. [10] described that TWAS Fe-based coating is very hard due to its abrasion resistant and elevated-temperature erosion resistance. Cheng et al. [11] reported that FeCrBSiNbW coating prepared by twin wire arc spraying process has excellent wear and corrosion resistance. In another study, Fu et al. [12] prepared

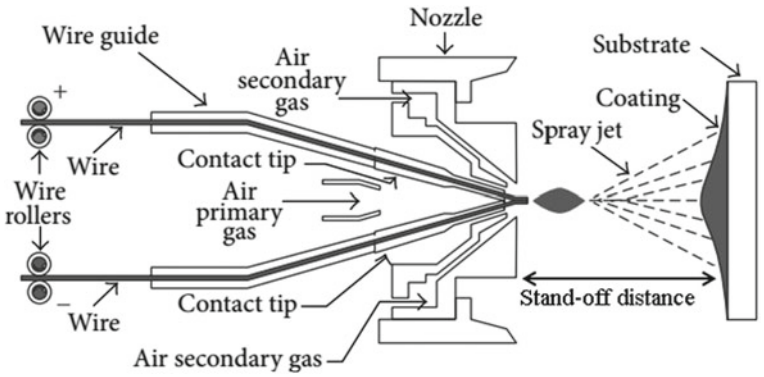

Fig. 11.1 Schematic twin wire arc spraying process

NiB-based and Fe-based amorphous coatings by TWAS on Q235 steel substrate. The coatings exhibited a better wear resistance than arc sprayed 3Cr13 coating. WC-8Co cladding coating on the surface of pump impeller from 1Cr18Ni9Ti stainless steel by electro-spark cladding was investigated by Ruizhu et al. [2]. In addition, Ref. [2] presented that the increases in hardness and wear resistance is because the cladding coating is uniform, continuous, compact, with no obvious cracks and holes, and there is no clear dividing line and a metallurgical bonding is presented between cladding coating and substrate material.

The effects of honing process on the friction and wear behaviors of Twin Wire Arc Spray (TWAS) coated aluminum cylinder liners were investigated by Kim et al. [6]. The experimental results indicate that TWAS process can be effectively utilized for engine applications in conjunction with optimum honing process for the cylinder liner [6]. Experimental study of twin wire arc sprayed Zn/Al coating on low carbon steel substrate has been undertaken by Djerourou et al. [13]. The results show that the spray distances have a effect on the coating microstructure and resistance against corrosion. The coating prepared at 100 mm (closest spray distance) present higher hardness and low porosity fraction compared to other prepared coatings [13]. As described above, twin wire arc spray coatings are used to improve friction and wear resistance. The result shows that the life span of machine parts or component is longer.

In modern industrial system, the major challenges are to produce materials with acceptable hardness level, low wear rate and high corrosive resistant and surface engineering. This is a rapid growing research area because of the high industrial demands for corrosion control and wear resistance, coupled with enabling technology that produces new kind of coatings with desirable tribological performance as well as mechanical properties. Those hard thin films has anti-abrasive characteristic under contact sliding. The contribution of this research into the material engineering field is the Fe-based amorphous coatings preparation by TWAS for pump impeller. The objective of this study is to investigate the effect of compressed air pressure and stand-off distance on the twin wire arc spray (TWAS) coating for pump impeller made of AISI 304 stainless steel.

11.2 Experimental Procedures

In this investigation, the substrate material is AISI 304 stainless steel with length, width and thickness dimension of 100 × 60 × 20 mm. Table 11.1 shows the chemical composition of AISI 304 stainless steel. Firstly, the substrate feed into sandblasting

Table 11.1 Chemical composition of AISI 304 stainless steel

Element	C	Mn	P	S	Si	Cr	Ni
Percentage (%)	0.08	2	0.045	0.30	1	18	8

process using NORBLAST machine by Norexo with type NOB35CE. The purpose of this process is to clean dirt, dust, and other attached particles and also to roughen the surface [14]. Sandblasting process uses brown aluminium oxide with mean roughness (Ra) produced of 75–100 μm. Next, the substrate undergoes spraying process with 75B (NiAl) as the bond coat material on the substrate. Bond coat material is used in order to enhance the adhesive coating because this material basically acts as the adhesive layer between the substrate and the top coat layer. Furthermore, this material is also used to mitigate coefficient of thermal expansion (CTE)-induced differential expansion between the coating and substrate [15]. The chemical composition of bond coat material is presented in Table 11.2. The next step is spraying process using 95MXC (FeCrBSiMn) material as the top coat using TAFA 9000 machine on the substrate. The chemical composition of 95MXC (FeCrBSiMn) is depicted in Table 11.3. The twin wire arc spray coating process parameters is presented in Table 11.4 and graphical working process of the experiment and material characterisation is presented in Fig. 11.2.

Material characterization were carried out to investigate the effect of various TWAS coating parameters on the coating product quality of AISI 304 stainless steel (substrate material) which furthermore will be used as pump impeller material. Characterization includes wear test using pin on disc method (ASTM G99-95A), vickers microhardness test (ASTM 92–82), Scanning Electron Microscope (SEM) and pull of bonding test to find out the adhesive coating or bond strength produced (ASTM D4541-02).

Table 11.2 Chemical composition of 75B [16]

Element	Ni	Al
Percentage (%)	95	5

Table 11.3 Chemical composition of 95 MXC [16]

Element	Si	Cr	Mn	B	Fe
Percentage (%)	1.7	28	2	3.7	64.6

Table 11.4 Twin wire arc spraying parameters

Parameter	Value
Current input	24 A
Voltage input	200 V
Current spraying	150 A
Voltage spraying	28.4 V
Wire size of NiAl	1.6 mm
Wire size of FeCrBMnSi	1.6 mm
Compressed air pressure	3, 4, 5 Bar
Stand-off distance	100, 200, 300, 400 mm

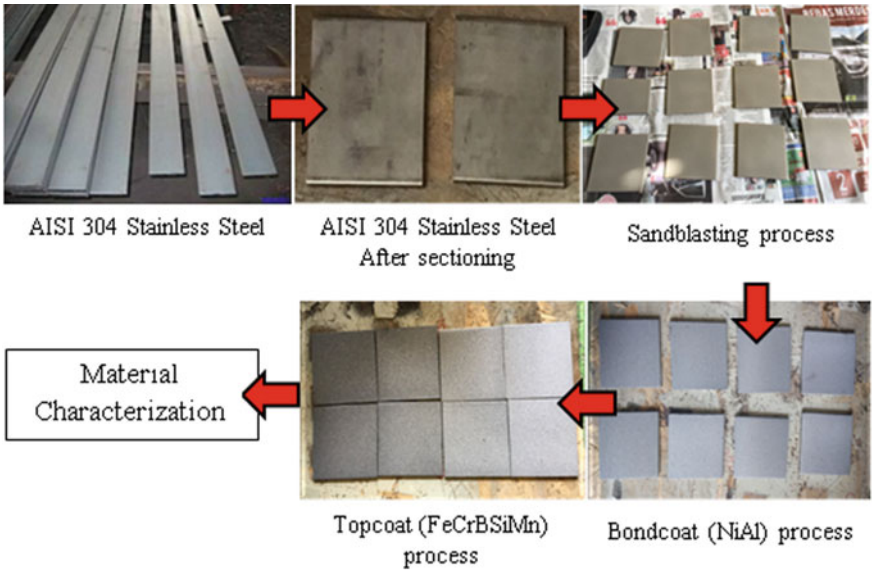

Fig. 11.2 Experimental setup and procedure

11.3 Results and Discussions

Scanning Electron Microscope (SEM) test is conducted to investigate the surface morphology of top coat on coating layers. With imageJ software, the analization result of SEM can be used to determine the value of porosity and unmelt on coating surface. Two important factors in imageJ software are contrast and brightness setting.

The determination of porosity and unmelt material percentage uses initial image grayscale and gray value (black to white) histogram on gray scale of 0–40 [17, 18].

Figure 11.3 shows an example of surface morphology of coating material by SEM with 4000 × magnification, where porosity, unmelt material, and oxide are appeared.

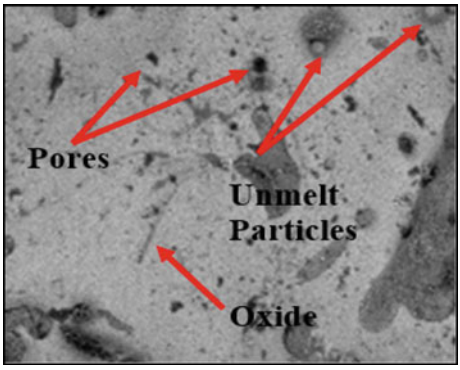

Fig. 11.3 TWAS morphology of coating surface by SEM on stand-off distance parameter and compressed air pressure of 100 mm and 3 Bar, respectively

This result has similarity with the result presented in Lin et al. [7] on page 1039, Fig. 11.6 in the article. Figure 11.4 shows an example of the application of image analysis (imageJ) for porosity and unmelt material measurement in experimental coating.

The effect of stand-off distance and compressed air pressure on the amount of porosity and unmelt material produced can be seen in Fig. 11.5. The smallest porosity and unmelt value is achieved at stand-off distance of 100 mm and compressed air pressure of 3 bar. An increasing in stand-off distance and compressed air pressure, the more porosity and unmelt produced. This occurs because an increasing of stand-off distance leads to cooling down the material along the way to the substrate, hence the bigger the porosity value. The value of porosity increases rapidly on stand-off distance of 200 mm [19, 20].

Moreover, increasing of compressed air pressure will produce large amount of porosity. This is because increasing of compressed air pressure leads to more mass rate produced by gun, which leads to particles melting imperfectly when sticking to the substrate, hence will increase the unmelt material on coating layer [21, 22].

Increasing of porosity and unmelt material amount will increase the thickness of coating layer thickness due to smaller material density [21, 23]. The effect of stand-off distance and compressed air pressure on thickness is presented in Fig. 11.6. Increasing of stand-off distance and compressed air pressure will increase the thickness of coating layer. The lowest thickness value is achieved at smallest porosity and unmelt material amounts, which is on stand-off distance and compressed air pressure of respectively 100 mm and 3 bar. The highest thickness value is found on stand-off distance and compressed air pressure of 400 mm and 5 bar, respectively, because this variation produces the highest porosity and unmelt material value.

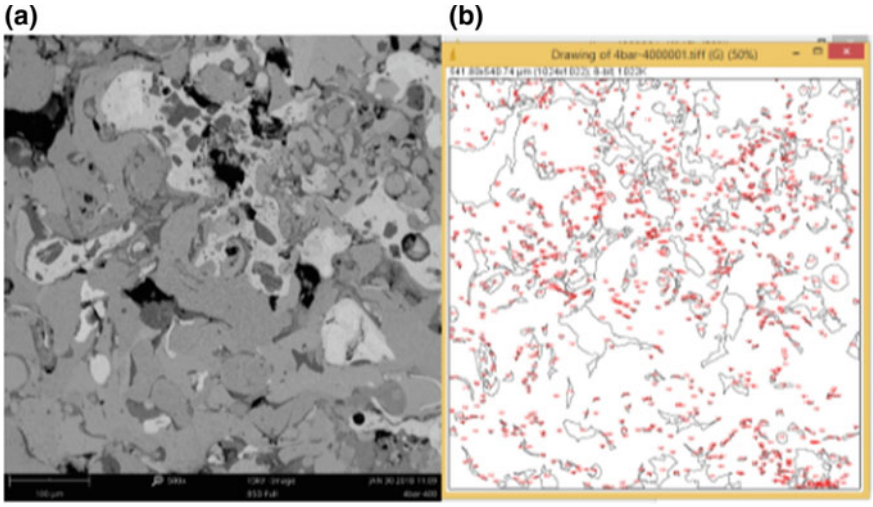

Fig. 11.4 Example technique for measuring porosity and unmelt material. **a** Before treatment, and **b** after treatment

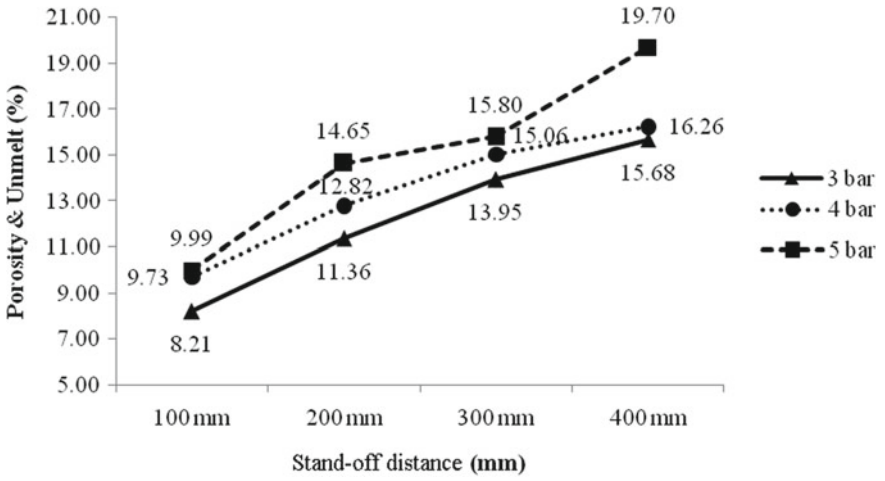

Fig. 11.5 The effect of stand-off distance and compressed air pressure on porosity and unmelt material

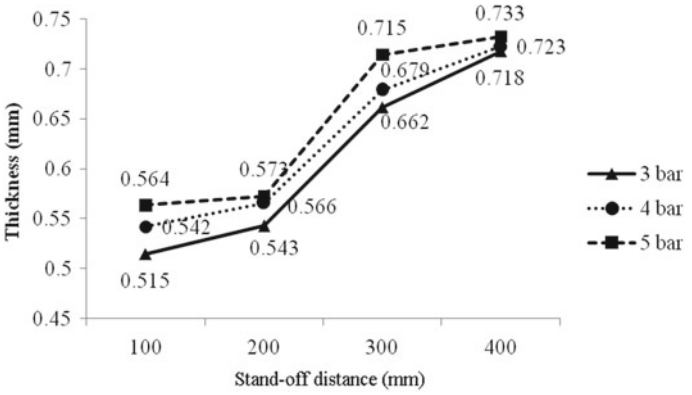

Fig. 11.6 The effect of stand-off distance and compressed air pressure on coating layer thickness

Thicker coating layer will decrease the adhesive coating or bond strength on coating layer due to higher residual stress [21, 24–27]. Figure 11.7 shows the effect of stand-off distance and compressed air pressure towards bond strength on coating. Increasing of stand-off distance and compressed air pressure value will decrease bond strength on coating because the coating layer produced will be thicker.

The highest bond strength value on coating is acquired on the experiment which produces the smallest thickness value, which is on the stand-off distance and compressed air pressure variation of 100 mm and 3 bar respectively. Moreover, the smallest bond strength value on coating is acquired on the experiment which produces the

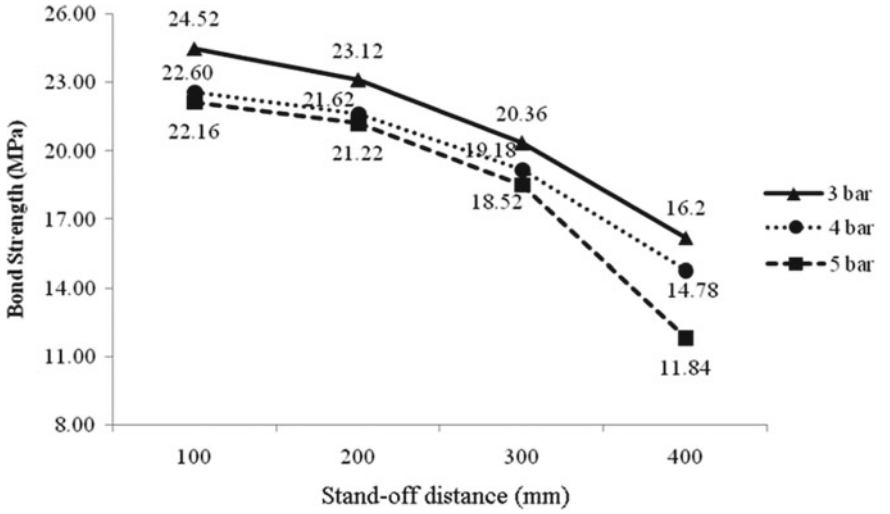

Fig. 11.7 The effect of stand-off distance and compressed air pressure on bond strength of coating

highest stand-off distance and compressed air pressure variation of 400 mm and 5 bar, respectively.

In other than affecting the bond strength on coating, coating layer thickness also has a significant effect towards the hardness of coating layer. The thicker coating layer will decrease the coating hardness [20, 21, 23]. Figure 11.8 shows the effect of stand-off distance and compressed air pressure on coating layer hardness. Uncoated substrate surface has a hardness value of 374 HV, whereas the coated surface has a hardness value of 800–1200 HV. Hardness value after coating fulfills the minimum

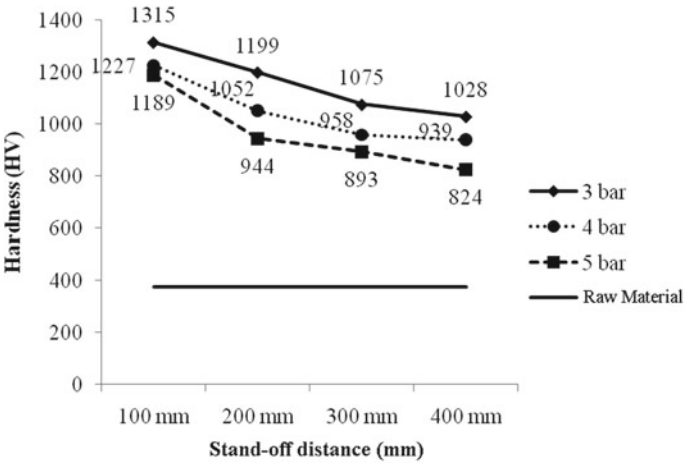

Fig. 11.8 The effect of stand-off distance and compressed air pressure on hardness of coating

hardness criteria on impeller after coating, which is 60 Rockwell C or 700 HV [28]. Increasing of stand-off distance and compressed air pressure will decrease the hardness value of coating layer.

The highest coating hardness value appeared on the experiment which produces the lowest thickness value, which is on stand-off distance and compressed air pressure of 100 mm and 3 bar, respectively. The lowest thickness value shows a small amount of porosity and unmelt material, thus the coating material density is better and the hardness value produced is higher [18, 29]. Closer stand-off distance produces smaller particle sizes thus the density of the material is higher, and leads to an increase in hardness value of coating material [22]. Moreover, increasing compressed air pressure will increases the velocity and mass sprayed to the substrate and produces imperfect melting particle with a large amount of porosity and will decrease coating hardness [21].

An increasing of stand-off distance and compressed air pressure value will decrease the hardness value on coating layer.

Lower hardness value leads to an increase in wear rate [2, 30]. In this study, a wear test uses abrasive method with pin on disk tool. A cylinder-shaped specimen is used as a pin, and silica carbide paper is used as the disk. This test is conducted on 10.000 cycles or equals to 2980 m [31]. Silica carbide paper is changed every 500 cycles with disk rotation speed of 100 rpm and applied load of 300 g. The wear rate in this study is calculated in Eq. (1) [32]:

$$\psi = \frac{V_{\text{loss}}}{t} \tag{1}$$

Figure 11.9 shows the effect of stand-off distance and compressed air pressure on wear rate. The increasing of stand-off distance and compressed air pressure value

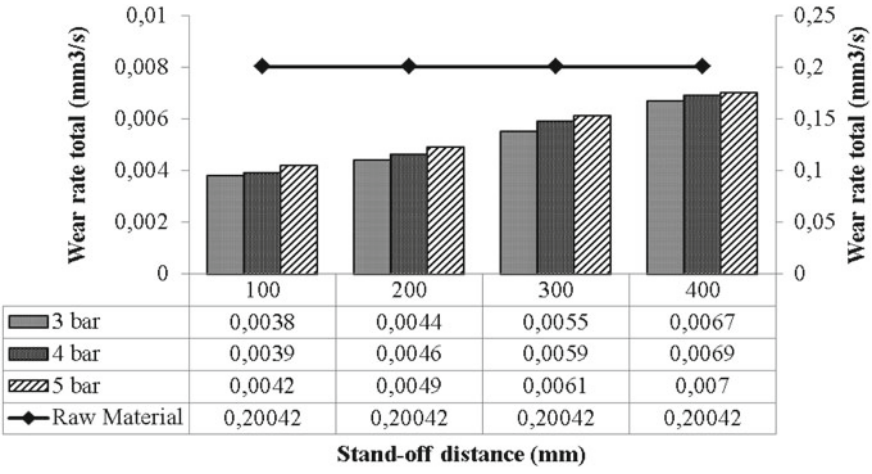

Fig. 11.9 The effect of stand-off distance and compressed air pressure on wear rate

will increase the wear rate because the hardness value produced is lower. In this study, the specimen with stand-off distance of 100 mm and compressed air pressure of 3 bar produces the lowest total wear rate value, namely 0.0038 m^3/s. The smallest total wear rate value shows high wear resistance value on the material. It is because on stand-off distance of 100 mm and compressed air pressure of 3 bar produces the highest hardness value, which is of 1315 HV. This hardness value is acquired due to its thin coating layer, as thin as 0.515 mm. Despite of affecting the value of hardness, the coating thickness value also affects the value of adhesive coating. In this study, the closer the stand-off distance and the lower the compressed gas pressure and also has the highest adhesive coating value of 24.52 MPa. The coating layer is thin due to its low porosity and unmelt material value.

11.4 Conclusions

The hardness value of AISI 304 stainless steel prior to coating process is 374 HV. After coating, the best cross sectional hardness value acquired is 1315 HV on the speciment with stand-off distance and compressed air pressure variation of 100 mm and 3 bar respectively. The total wear rate of AISI 304 stainless steel prior to coating is of 2×10^{-2} mm^3/s. An optimum wear rate is acquired on the speciment with stand-off distance and compressed air pressure variation 100 mm and 3 bar respectively, with value of 3.8×10^{-4} mm^3/s.

The decreasing of stand-off distance and compressed air pressure will increase the hardness of coating layer. It will cause decreasing of wear rate and increasing of wear resistance. Increasing hardness of coating layer due to produced is thinner as a result of the low porosity and unmelted material in the coating layer. The thinner coating layer will increase the adhesive coating value.

Acknowledgements The first Author would like to express their gratefulness to Electrical Analysis and Engineering Measurement—Reliability Analysis Laboratory of Diponegoro University for research fund in this study.

References

1. R.O.P. Serrano, L.P. Santos, E.M.F. Viana, M.A. Pinto, C.B. Martinez, Case study: effects of sediment concentration on the wear of fluvial water pump impellers on Brazil's Acre river. Wear **408**–**409**, 131–137 (2018)
2. Z. Ruizhu, L. Jingrui, Y. Dakao, Z. Yuanyuan, Mechanical properties of WC-8Co wear—resistant coating on pump impellers surface by electro—spark. Rare Met. Mater. Eng. **44**(7), 1587–1590 (2015)
3. Y. Zhong, N. Zhang, P. Zhou, H. Sun, Study on inertial separation device of the sandy flow. J. Phys: Conf. Ser. **1064**, 1–8 (2018)
4. C. McCaul, R. Kaufold, Evaluation of coating for resistance to abrasive and adhesive wear in pump components. Proceedings of the ninth international pump users symposium, 89–95 1992

5. V. Mammadov, K. Tacon, B. Davies, N.S. Ahmedov, Coatings help to improve centrifugal pump reliability. Fluid machinery congress, 67–77 2014
6. J.K. Kim, F.A. Xavier, D.E. Kim, Tribological properties of twin wire arc spray coated aluminum cylinder liner. Mater. Des. **84**, 231–237 (2015)
7. J. Lin, Z. Wang, P. Lin, J. Cheng, X. Zhang, S. Hong, Effects of post annealing on the microstructure, mechanical properties and cavitation erosion behavior of arc-sprayed FeNiCrBSiNbW coatings. Mater. Des. **65**, 1035–1040 (2015)
8. A.L. Horner, A.C. Hall, J.F. McCloskey, The effect of process parameters on twin wire arc spray pattern shape. Coatings **5**, 115–123 (2015)
9. A. Arizmendi-Morquecho, A. Campa-Castilla, C. Leyva-Porras, J.A. Aguilar Martinez, G. Vargas Gutiérrez, K.J. Moreno Bello and L. López López, Microstructural characterization and wear properties of Fe-based amorphous-crystalline coating deposited by twin wire arc spraying. Adv. Mater. Sci. Eng. 1–11 (2014)
10. J. Zhou, J.K. Walleser, B.E. Meacham, D.J. Branagan, Novel in situ transformable coating for elevated-temperature applications. J. Therm. Spray Technol. **19**(5), 950–957 (2010)
11. J.B. Cheng, Z.H. Wang, B.S. Xu, Wear and corrosion behaviors of FeCrBSiNbW amorphous/nanocrystalline coating prepared by arc spraying process. J. Therm. Spray Technol. **21**(5), 1025–1031 (2012)
12. B.Y. Fu, D.Y. He, L.D. Zhao, J.M. Jiang, X.Y. Li, Microstructure and properties of arc sprayed coatings containing Fe based amorphous phase and nanocrystallites. Surf. Eng. **25**(4), 333–337 (2009)
13. S. Djerourou, H. Lahmar, N. Bouhellal, Y. Mebdoua, Study of twin wire arc sprayed zinc/aluminum coating on low carbon steel substrate: application to corrosion protection. Adv. Mater. Res. **685**, 271–276 (2013)
14. K. Poorna Chander, M. Vashista, K. Sabiruddin, S. Paul, P.P. Bandyopadhyay, Effects of grit blasting on surface properties of steel substrates. Mater. Design 30(8), 2895–2902 (2009)
15. R.C., Tucker, Jr., Thermal Spray Technology, ASM Handbook, vol 5, pp. 76–88 (2013)
16. Material Safety Data Sheet PRAXAIR (2012). Accessed on May 2019
17. G.B. Sucharski, A.G.M. Pukasiewicz, R.F. Váz, R.S.C. Paredes, Optimization of the deposition parameters of HVOF FeMnCrSi + Ni + B thermally sprayed coatings. Soldagem Inspeção **20**(2), 238–252 (2015)
18. H. Irawan, *Analysis of Post-Annealing Effect Ni-Al and FeCrBMnSi Metallic Coating by Twin Wire Arc Spraying (TWAS) on Microstructures and Mechanical Properties, Department of Materials and Metallurgical Engineering* (Faculty of Industry Technology, Institut Teknologi Sepuluh Nopember, Surabaya, 2016)
19. A. Harju, Properties of high velocity Arc sprayed coatings. Tampere University of Technology, Master of Science Thesis (2017)
20. I. Kucukrendeci, S.H. Yetgin, Coating parameters influences on mechanical properties of coating. J. Appl. Sci. **13**, 645–649 (2013)
21. J.C. Tan, Optimisation of the HVOF thermal spray process for coating, forming and repair of components. School of Mechanical and Manufacturing Engineering, Dublin City University, Doctor of Philosophy Thesis (1997)
22. R. Daengmool, S. Wirojanupatump, S. Jiansirisomboon, A. Sopadang, Effect of spray parameters on stainless steel Arc sprayed coating. Chiang Mai University (2016)
23. O. Sarikaya, Effect of some parameters on microstructure and hardness of alumina coatings prepared by the air plasma spraying process. Surf. Coat. Technol. **190**(2–3), 388–393 (2005)
24. D.J. Greving, J.R. Shadley, E.F. Rybicki, Effects of coating thickness and residual stresses on the bond strength of ASTM C633-79 thermal spray coating test specimens. J. Therm. Spray Technol. **3**(4), 371–378 (1994)
25. P. Araujo, D. Chicot, M. Staia, J. Lesage, Residual stresses and adhesion of thermal spray coatings. Surf. Eng. 21(1), 35–40 (2005)
26. R. Singh, S. Schruefer, S. Wilson, J. Gibmeier, R. Vassen, Influence of coating thickness on residual stress and adhesion-strength of cold-sprayed Inconel 718 coatings. Surf. Coat. Technol. **350**, 64–73 (2018)

27. A.W.Y. Tan, W. Sun, A. Bhowmik, J.Y. Lek, I. Marinescu, F. Li, E. Liu, Effect of coating thickness on microstructure, mechanical properties and fracture behaviour of cold sprayed Ti6Al4V coatings on Ti6Al4V substrates. Surf. Coat. Technol. **349**, 303–317 (2018)
28. V.S. Lobanoff, R.R. Ross, *Centrifugal Pumps Design and Application*, 2nd edn. (Gulf Publishing Company, United States of America, 1992)
29. L. Pawlowski, *The Science and Engineering of Thermal Spray Coatings*, 2nd edn. (Wiley, London, 2008)
30. K. Cooke, G. Oliver, V. Buchanan, N. Palmer, Optimisation of the electric wire Arc-spraying process for improved wear resistance of sugar mill roller shells, surface and coating. Surf. Coat. Technol. 185–188 (2007)
31. http://shodhganga.inflibnet.ac.in/bitstream/10603/34533/11/11_chapter6.pdf. Accessed on May 2019
32. J.W. Kaczmar, K. Pietrzak, W. WøosinÂski, The production and application of metal matrix composite materials. J. Mater. Process. Technol. **106**, 58–67 (2000)

Chapter 12
An Application of High Temperature Gas Nitriding (HTGN) Method to Improve the Quality of Implant Materials 316L and 316LVM

A. Suprihanto, D. F. Fitriyana, Armila and Wahyu Caesarendra

Abstract This paper presents an application of high temperature gas nitriding (HTGN) method to enhance the material properties of implant materials 316L and 316LVM. The HTGN method is applied to 316L and 316LVM materials at 1050, 1100 and 1200 °C. Three different holding times for HTGN method were varied up to 15, 30 and 60 min to have different comparison results. This research observed that grain size, nitrogen content, hardness, corrosion rate and non-magnetic stability increase as increase of temperature and holding time. The lowest corrosion rate is obtained at 1050 °C and 15 min treatments.

12.1 Introduction

Austenitic stainless steel 316L is widely used as implant materials because it has sufficient mechanical properties, corrosion resistance and non-magnetic. American Society for Testing and Materials (ASTM) in the F138-04 and F139-03 standards recommends that 316L as implant materials. Although the performance of 316L fulfill the standard medical requirements, it causes sensitization due to corrosion in the last two decades [1, 2]. The product of corrosion is detrimental to the body because it causes irritations, allergy and infection to the patients. In the corrosive environments, lack of oxygen and highly stressed conditions such as at bone plates and screw application affects to decrease the corrosion resistance of 316L [3].

Various methods have been developed to enhance the corrosion resistance such as casting process, surface treatments and alloying aditions. Improvement in the

A. Suprihanto · W. Caesarendra (✉)
Department of Mechanical Engineering, Diponegoro University, Jl. Prof. Soedharto SH, Semarang 50275, Indonesia
e-mail: wahyu.caesarendra@ubd.edu.bn

D. F. Fitriyana
Department of Mechanical Engineering, Semarang State University, Semarang 50229, Indonesia

Armila
Department of Mechanical Engineering, Muhammadiyah University of West Sumatera, Jl. Pasir Kandang no.4 Koto Tangah, Padang 25172, Indonesia

R.-I. Murakami et al. (eds.), *NAC 2019*, Springer Proceedings in Physics 242,
https://doi.org/10.1007/978-981-15-2294-9_12

casting process by means vacuum casting produce austenitic stainless steel 316LVM [4]. The developments of alloying additions are done by increasing the chromium, molybdenum and nitrogen contents. The addition of nitrogen is also done by surface treatments such as nitriding. Nitriding process produce thin layer of hard nitride. AISI 316L Stainless Steel may be nitrided to improve corrosion resistance [5, 6]. Otherwise, corrosion resistance decreased by Chromium Nitride (CrN) formation in layer, whereas increased surface hardness and wear resistance [6, 7].

Implant materials should be stable for non-magnetic properties however nitride is ferro-magnetic [8, 9]. Ferromagnetic properties on 316L produced low magnetic properties that elevated risk of magnetic resonance imaging (MRI) evaluation [10]. Impant material will save at MRI 1.5T but unsafe for MRI 3T or above [10, 11]. The Increasing of temperature on high temperature gas nitriding (HTGN) able to diffuses nitrogen into stainless steel and minimize formation of nitride. The treatment based on expose stainless steel in nitrogen atmosphere at 1050–1200 °C for special timing and followed by quenching [7, 12]. HTGN produced coarse grain where will reduce tensile and fatigue strength [12].

HTGN treatments promises the increasing of corrosion resistance of materials 316L and 316LVM without reduce the non-magnetic properties. In order to overcome the grain coarsening, the longer holding time can be avoided. The research studies the effects of short holding time on the microstructure, corrosion rate, hardness and magnetic properties of 316L and 316LVM.

12.2 Experimental Procedures

The chemical composition of 316L and 316LVM is presented in Table 12.1. The dimension of specimens is 200 mm in length, 50 mm in width and 2 mm in thickness. The HTGN treatments is conducted at 1 atm pressure of nitrogen gas, treatments temperature at 1050, 1100 and 1200 °C and holding time for 15, 30 and 60 min prior quenching in the water.

HTGN treatments conducted at modified vertical furnace, which equipped with pressure controller as depicted in Fig. 12.1. Specimens were cleaned using ultrasonic cleaner in the acetone medium. Specimens were inserted to furnace tube. Before the heating process, the furnace tube is vacuumed to 10 Pa and flushing with nitrogen gas at 100 mL/min. The heating rate was selected at 10 °C/min.

Table 12.1 Chemical composition of specimens

	C	Cr	Ni	Mo	Mn	Si	Fe
316L	0.01	15.5	11.8	1.24	1.23	0.47	69.75
316LVM	0.01	17.3	15.5	1.73	1.67	0.42	63.37

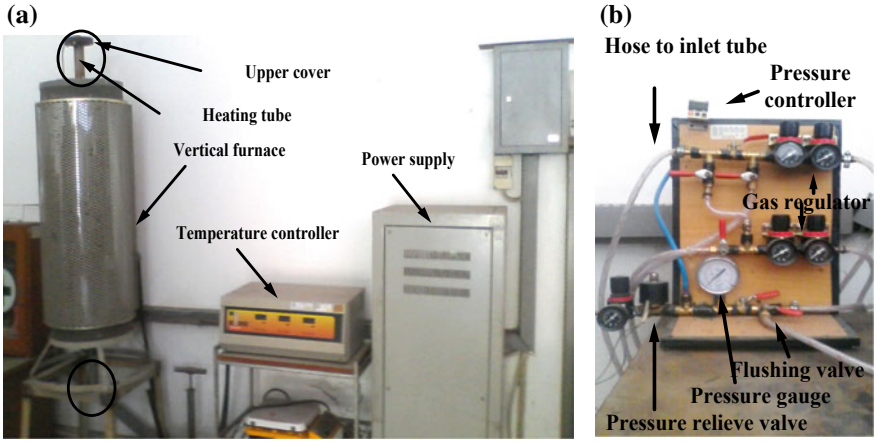

Fig. 12.1 HTGN treatment equipment: **a** vertical furnace; **b** gas pressure controller

Raw material and treated specimens were characterized by metallographic evaluation, hardness, chemical composition, corrosion and magnetism testing. The evaluation of microstructure was conducted at light optical microscope. The identification of phase will be presents on the specimens used the Shimadzu 7000s XRD systems. The spectrum of XRD was compared to crystallography open database (COD) v.64680 using Match v.1.1 software. The measurements of grain size used ImageJ v. 1.47 software. Hardness test conducted using Buehler Vickers microhardness tester. The distribution of chemical composition was conducted using SEM/EDS JEOL type 6500(LA).

Corrosion resistance was conducted using galvanostat type 273 manufactured by Princeton Applied Research. Corrosion test used ringer solutions as simulated body fluids at temperature 37 °C. Magnetism properties were evaluated using Oxford *vibrating sample magnetometer* (VSM) type 1.2H.

12.3 Results and Discussions

The grains grow in size with increasing temperature and holding time (Figs. 12.2 and 12.3). The XRD spectrum of specimens at the surface after HTGN treatments are shown in Fig. 12.4. The strongest peak obtained closed to 44°, 50°, and 75° indicate the austenite phase. HTGN treatments materials 316L and 316LVM not changed initial phase. Figure 12.4 shows that austenite is the only phase on microstructure at the surface. It indicates that nitrogen atoms are interstitially solid solution in austenite phase.

The influence of temperature and holding time on the grain size is presented in Fig. 12.5. Figure 12.5 shows that the slope of regression line for treatments at

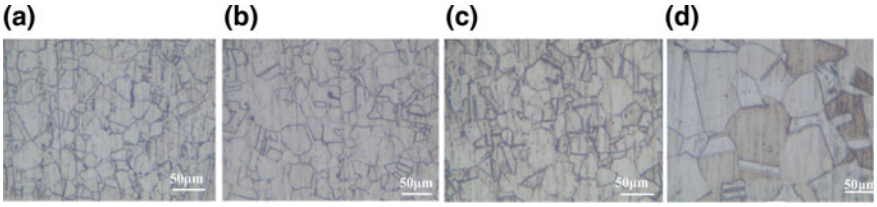

Fig. 12.2 Microstructure of 316L: **a** raw material; **b** temperature of 1050 °C for 15 min holding time; **c** temperature of 1100 °C for 15 min holding time; **d** temperature of 1200 °C for 15 min holding time

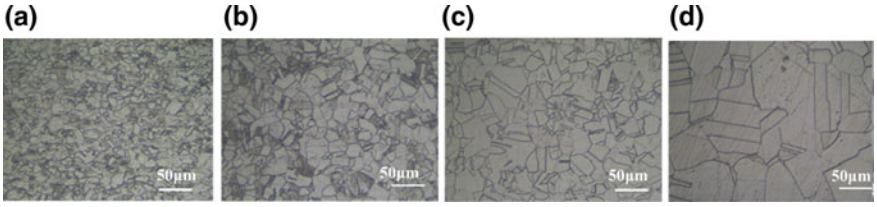

Fig. 12.3 Microstructure of 316LVM: **a** raw material; **b** temperature of 1050 °C for 15 min holding time; **c** temperature of 1100 °C for 15 min holding time; **d** Temperature of 1200 °C for 15 min holding time

Fig. 12.4 XRD spectrum treated specimens for 316L and 316LVM

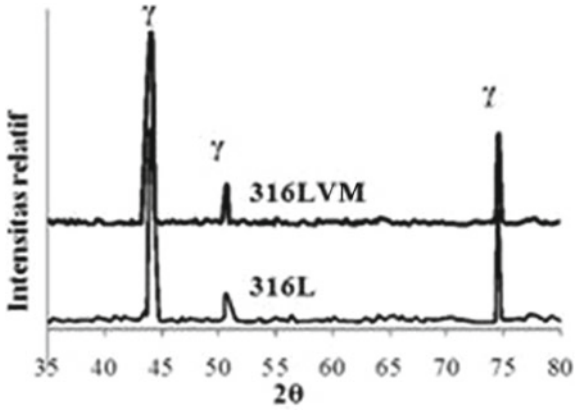

1200 °C with holding time 60 min is highest than other treatments. It indicates that the increasing of grain size growth is obtained at 1200 °C and 60 min treatments. Increasing the process temperature cause grain more easily to growth and the final size of grain is determined by holding time [13].

In the classical phenomenological expression for isothermal grain growth, there are three important coefficients that indicate the grain growth in most alloy [14]. The

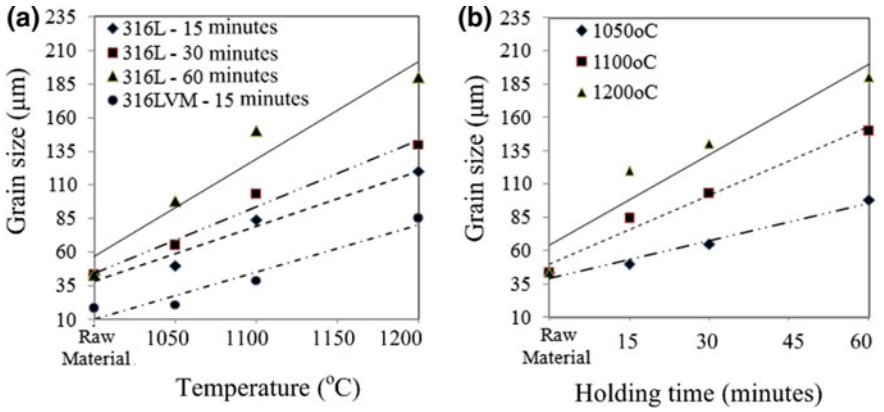

Fig. 12.5 **a** The effect of temperature on grain size; **b** the effect of holding time on grain size

final grain size depends on (1) grain growth exponent (n), (2) grain growth rate (K), and (3) activation energy (Q) as shown in Eq. (12.1).

The magnitude of activation energy at 900–1200 °C is 52 kJ/mol [15]. The magnitude of grain growth exponent (n) is between 2.5 and 3.5 [14].

$$d^n - d_o^n = K.t.exp(-Q/RT) \tag{12.1}$$

The magnitude of three coefficients obtained from curve fitting technique are 1.61; 83 μm/s and 55.717 kJ/mol for n, K and Q respectively. This result is close to the activation energy studied [15]. However, the magnitude of grain growth exponential is lower. The accuracy of calculations $\left(d^n - d_o^n\right)$ and measurement $K.t.exp(-Q/RT)$ of grain size based on three calculated coefficients is presented in Fig. 12.6. As shown at Fig. 12.6, the magnitude of grain size from calculation and measurements is similar/identical to each other.

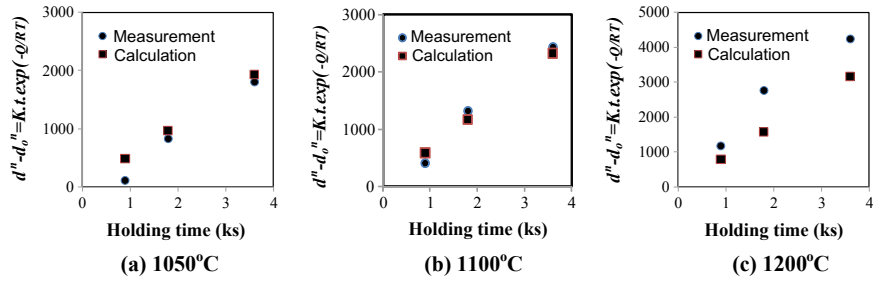

Fig. 12.6 Calculations and measurements of grain size

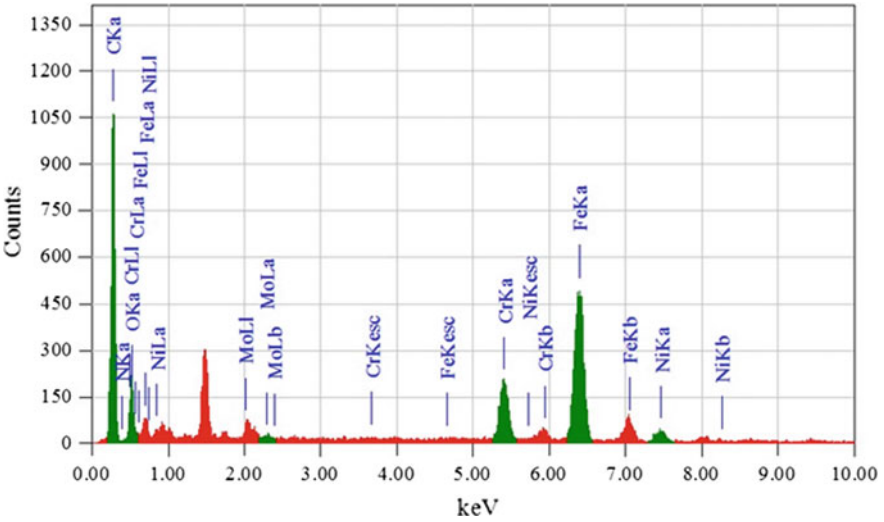

Fig. 12.7 EDS spectrum at the surface of treated specimens

Figure 12.7 shows the EDS spectrum at the surface of treated specimens. The presents of nitrogen is detected from the spectrum. It indicates that HTGN treatments are able to the nitrogen diffuses on the specimens.

The distribution of nitrogen concentration *C(x,t)* can be calculated by Ficks II law as shown in Eq. (12.2). C_S and C_O are the nitrogen concentration at the surface and initial concentration respectively.

The increasing of nitrogen contents causes the increasing of the hardness of specimens [16, 17]. The distribution of hardness over cross sectional is also calculated using Ficks II law. The develops the diffusion formula from the hardness measurements as shown in Eq. (12.3) [18]. The hardness distribution *H(x,t)* depends on the magnitude of hardness at the surface H_S, the initial harness H_O, distance from the surface x, diffusion time t and diffusion coefficients D_N.

$$C(x,t) - C_o = (C_S - C_o)(1 - erf\left(x/2\sqrt{Dt}\right) \tag{12.2}$$

$$(x,t) - H_o = (H_S - H_o)(1 - erf\left(x/2\sqrt{Dt}\right) \tag{12.3}$$

The magnitude of DN obtained from curve fitting are 9.96×10^{-12}, 2.66×10^{-11} and 2.72×10^{-11} m^2/s at temperature 1050, 1100 and 1200 °C respectively. The distribution pattern from calculation and measurements of nitrogen contents near the surface of specimens are shown at Fig. 12.8. Increasing holding time and treatments temperature increase the concentration of nitrogen in the material. The increasing of nitrogen contents after treatment causes the increasing of its hardness. This mechanism is similar to the role of carbon in strengthening mechanism in the

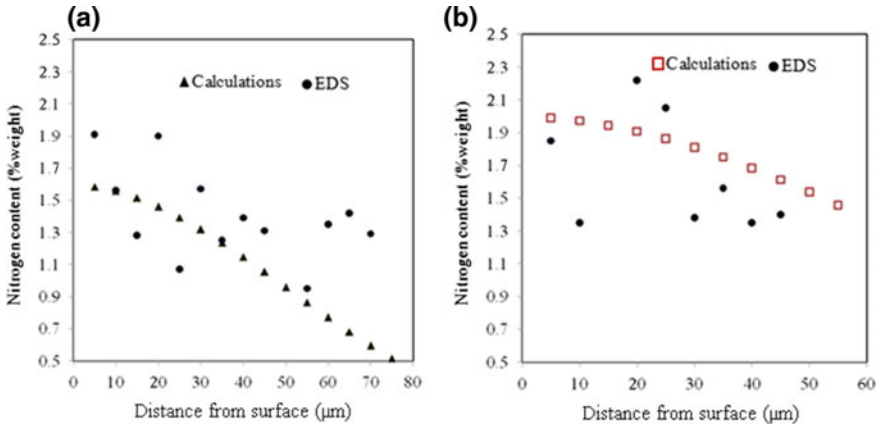

Fig. 12.8 Distribution pattern for treated 316L at the near surface region **a** temperature 1050 °C and holding time 15 min; **b** temperature 1200 °C and holding time 60 min

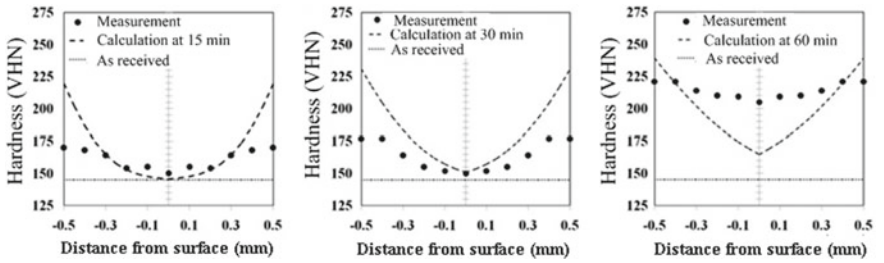

Fig. 12.9 Hardness distribution pattern for material 316L at 1050 °C

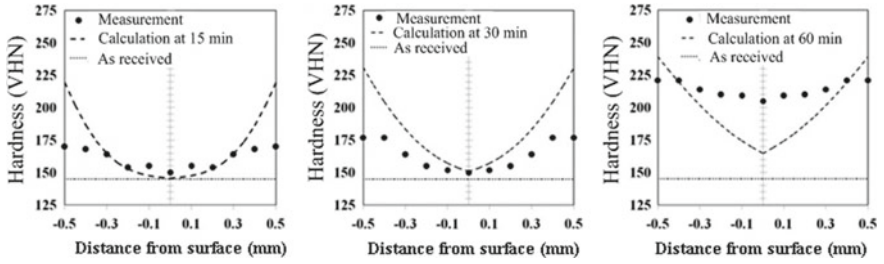

Fig. 12.10 Hardness distribution pattern for material 316L at 1100 °C

steel [13]. The distribution pattern for hardness as shows in Figs. 12.9, 12.10 and 12.11. The distribution pattern from calculation and measurements is similar to each other. It indicates where the accuracy of the calculation of hardness and nitrogen concentration are high.

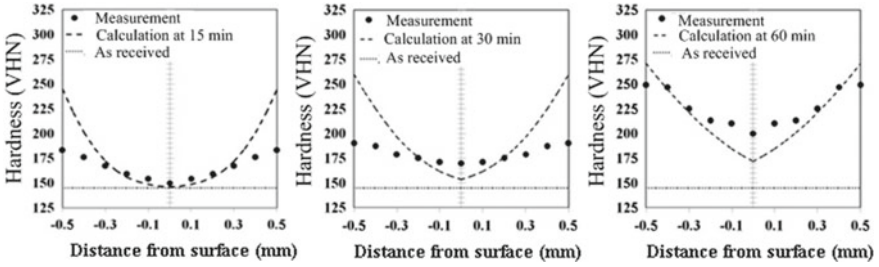

Fig. 12.11 Hardness distribution pattern for material 316L at 1200 °C

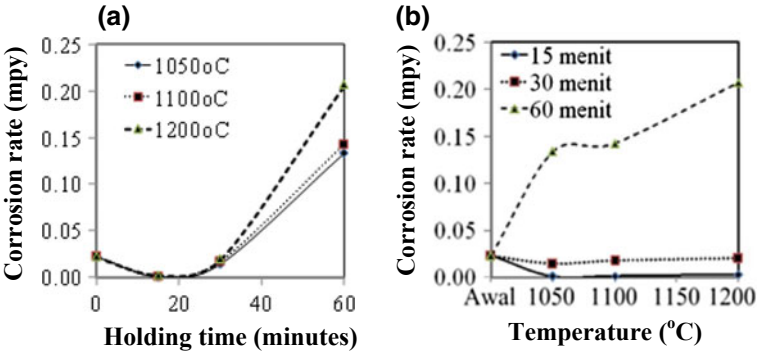

Fig. 12.12 The effect of treatments on the corrosion resistance of material 316L: **a** holding time versus Corrosion rate; **b** temperature versus corrosion rate

Fig. 12.13 The effect of treatments on the corrosion resistance of material 316LVM

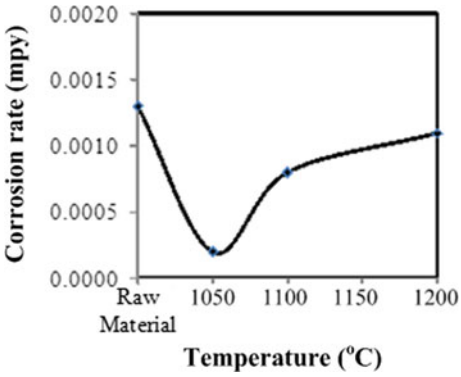

The increasing of nitrogen contents influences the corrosion rate of the materials. Figures 12.12 and 12.13 show the influence of temperature and holding time treatments to the corrosion rate in the ringer solution. The increasing nitrogen contents

due to increasing temperature and holding time result to the decreasing on the corrosion rate. However, corrosion rate increases with temperature and holding time. The influence of nitrogen on the corrosion resistance of stainless steel has two effects: (1) Nitrogen addition improve the corrosion resistance of stainless steel [19–24]. (2) The effectiveness of nitrogen on the improvements of corrosion resistance only if the nitrogen does not form of nitride [7, 25]. In contrast, corrosion resistance enhanced by nitride formation [5, 6].

Based on the calculation of corrosion rate at Fig. 12.12 that the corrosion rate of the implanted sample with lowest temperature and shortest holding time is lower than the implanted sample with highest temperature and longest holding time. This case indicates that the nitride phase formed in the modified layer plays a very important role in increasing the corrosion resistance of the planted sample. The nitrogen ion implanted in the sample changes the surface topography by inducing defects in the sample to increase the corrosion resistance of the material. The optimum corrosion resistance occurs at a temperature 1050 °C with 15 min holding time. This case happens because nitrogen ions which are implanted in the target material lead to the arrangement of the atomic surface of a denser material. The dense arrangement of atoms makes the strength of the protective layer increase so that the corrosion rate decreases. However, if the implantation process is continuously carried out with the addition of a dose exceeding the requirement, there will be a deposit of nitrogen ions on the surface to form a thin amorphous layer. The continuous addition of dosage will cause the ionic ion accumulated on the surface forming an amorphous layer thus the corrosion rate will increase [26].

Chemical composition is not the main factors which influences to corrosion resistance of stainless steel. The corrosion resistance also depends on the homogeneity and cleanliness such as in the case material 316L and 316LVM [4]. Another factor that influences the corrosion resistance is grain size [27]. The fine grain size produces higher corrosion resistance than coarse grain. The fine grain size enhances the passivation process because the fine grain has higher corrosion resistance than coarse grain [28]. Corrosion is the chemical process on the surface of specimen. The corrosion behaviour is solely determined by the condition on specimen surface. During HTGN treatments, diffusion and grain growth occur simultaneously. Diffusion is more easily to diffuse at the grain boundary than in the grain itself. The diffusion is also diffused from grain boundary into grain. When the grain is small, the diffusion rate at the grain and grain boundary will diffused in the at the same rate. Therefore it will produces the homogeneity of nitrogen concentration on the surface. As the grain become coarse, the diffusion rate at grain boundary is more dominants than at the grain. As a result, it produces the inhomogeneous nitrogen concentration and lead to the decreasing of corrosion resistance. Figure 12.14 shows the mechanism diffusion process during HTGN treatments.

The solubility limits of nitrogen at the surface immediately achieve as HTGN treatments process [16]. The longer holding time, the more diffusion depth occurred. The lowest temperature and longer holding time produce the finer grain size. The increasing of nitrogen contents combined with fine grain size produces the highest corrosion resistance.

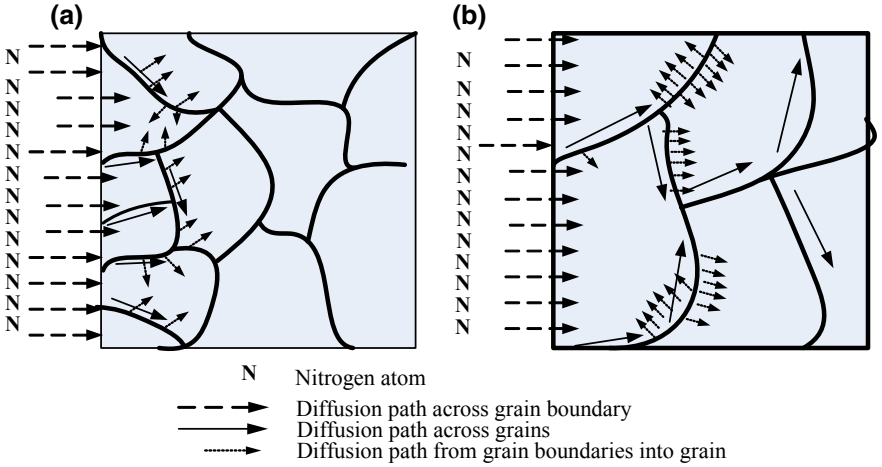

Fig. 12.14 Diffusion process during HTGN treatments: **a** fine grain; **b** coarse grain

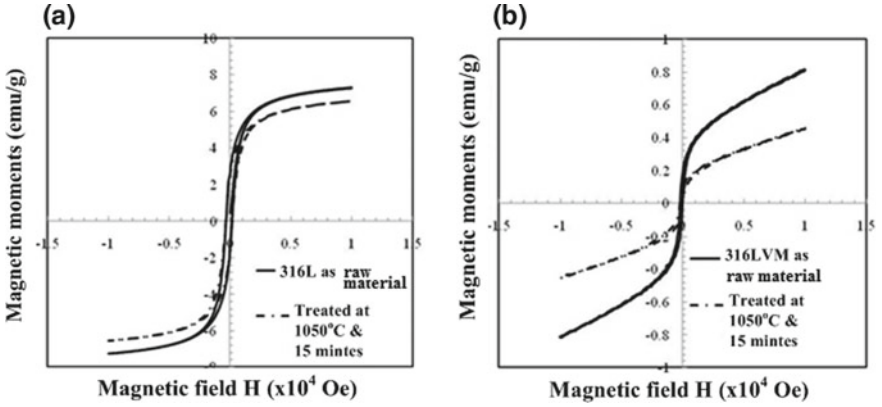

Fig. 12.15 Hysteresis curve of VSM test: **a** 316L; **b** 316LVM

Figure 12.15 shows the hysteresis curve obtained from treated materials 316L and 316LVM. The hysteresis curve from treated specimens at 1050 °C and 15 min is smaller than raw material. 316LVM before treatment has magnetization curve is lower one per-tenth compared to the 316L before treatment. It indicates that vacuums melting not only enhance the corrosion resistance but also improve the non-magnetic properties of 316LVM. Figure 12.15 shows that after HTGN treatments, the magnetization curve both 316L and 316LVM is lower than raw material specimens. It indicates that HTGN not only increase the corrosion resistance but also improve the stable non-magnetic phase [29]. Table 12.2 shows that the saturation magnetization (M_s), the remanent magnetization (M_r) and coercive field or coercivity (H_c) decrease

Table 12.2 Magnitude of M_s, M_r, H_c, κ and μ_r

	316L		316LVM	
	Raw material	T = 1050 °C, t = 15 min	Raw material	T = 1050 °C, t = 15 min
M_s (emu/g)	7.29	6.54	0.78	0.431
M_r (emu/g)	2.52	2.33	0.16	0.079
H_c (Oe)	2.11×10^6	1.41×10^6	9.92×10^{-2}	8.17×10^{-2}
K	0.0042	0.0039	0.0006	0.0002
μ_r	1.0042	1.0039	1.0006	1.0002

significantly. Magnetic susceptibility (κ) which is the slope of linier portion of hysteresis curve is also decrease. The magnetic permeability (μ_r) which the parameter of non-magnetic stability is also increases. Nitrogen is strong austenite stabilizer. The increasing nitrogen contents enhance the stability of non-magnetic properties of treated specimens.

12.4 Conclusions

The HTGN treatments is adequate diffusion the nitrogen in the materials 316L and 316LVM. Nitrogen concentration, hardness, corrosion rate and non-magnetic stability increase by temperature and holding time. The optimum treatments temperature and holding time that produce highest corrosion resistance, increasing non-magnetic stability and avoid produce coarse grain size at 1050 °C and 15 min.

References

1. P.J. Uggowitzer, R. Magdowski, M.O. Spidel, Nickel free high nitrogen austenitic stainless steel. ISIJ Int. **36**(7), 901–908 (1996)
2. K. Yang, Y. Ren, Nickel free austenitic stainless steel for medical application. Sci. Technol. Adv. Mater. **11**, 1–13 (2010)
3. S. Desai, B. Biandda, P. Bartalo, Metallic and ceramic biomaterial: current and future developments, in *Bio-Materials and Prototyping Applications in Medicine*, ed. by B. Bartolo, B. Biandda (Springer Science, 2008)
4. S. Ahmadi, H. Arabi, A. Shokuhfar, A. Rezer, Evaluation of the electroslag remelting process in medical grade of 316LC stainless steel. J. Mater. Sci. Technol. **25**(5), 592–596 (2009)
5. M.O. Dionisyo, M. Campos, O.Z. Higa, T.E. Cunha, S.D. de Souza, Investigating the correlation between some of the properties of plasma nitrided AISI 316L stainless steel. Mater. Res. **16**(5), 1052–1057 (2013)
6. M. Martinesi, S. Bruni, M. Stio, C. Treves, T. Bacciand, F. Borgioli, Biocompatibility evaluation of surface treated AISI 316L austenitic stainless steel in human cell cultures. J. Biomed. Mater. Res. **80**, 131–145 (2007)

7. H. Berns, Advantages in solution nitriding of stainless steel. Mater. Sci. Heat Treat. **49**(11–12), 578–580 (2007)
8. R.L.O. Basso, V.L. Pimentel, S. Weber, G. Marcos, T. Czewiec, Magnetic and structural properties of ion nitrided stainless steel. J. Appl. Phys. **105**, 124914-1–124914-5 (2009)
9. O. Ozturk, S. Okurand, J.P. Riviere, Structural and magnetic characterization of plasma ion nitrided layer on 316L stainless steel aloy. Nucl. Instrum. Methods Phys. Res. B **67**, 1540–1545 (2009)
10. A. Holton, E. Walsh, A. Anayiotos, G. Pohostand, R. Venugopalan, Comparative MRI compatibility of 316L stainless steel alloy and nickel-titanium alloy stent. Cardiovas. Magn. Reson. **4**(4), 423–430 (2002)
11. F.G. Shellock, Biomedical implants and devices: assessment of magnetic field interaction with a 3.0-Tesla MR system. J. Magn. Reson. Imaging **16**, 721–732 (2002)
12. D. Kuroda, T. Hanawa, T. Hibaru, S. Kuroda, M. Kobayashi, New manufacturing process of nickel free austenitic stainless steel with nitrogen absorption treatment. Mater. Trans. **44**(3), 414–420 (2003)
13. A. Suprihanto, S. Suyitno, R. Dharmastiti, Corrosion resistance of AISI 316L after short holding time of high temperature gas nitriding (HTGN). Chem. Mater. Res. **3**(2), 1–7 (2013)
14. N. Hirota, F. Yin, T. Inoue, T. Azuma, Recrystalization and grain growth behavior in severe cold rolling deformed SUS316L under an isothermal annealing condition. ISIJ Int. **48**(4), 475–482 (2008)
15. B.P. Kasyap, K. Tangri, Grain growth behaviour of type 316L stainless steel. Mater. Sci. Eng., A **A149**, L13–L16 (1992)
16. T. Tsuchiyama, T. Fukumaru, M. Egashira, S. Endo, Calculation of nitrogen absorption into austenitic stainless steel plate and wire. ISIJ Int. **44**(6), 1121–1123 (2004)
17. Y. Turan, A. Koursaris, The effect of nitrogen additions on the structure and properties of AISI 310S stainless steel. J. South Afr. Inst. Min. Metal. 347–353 (1995)
18. Y.Z. Shen, K.H. Oh, D.N. Lee, Nitrogen strengthening of interstitial-free steel by nitriding in potassium nitrate salt bath. Mater. Sci. Eng. A **A343**, 314–318 (2006)
19. S. Azuma, H. Miyuki, T. Udo, Effect of alloying nitrogen on crevice corrosion of austenitic stainless steels. ISIJ Int. **36**(7), 793–798 (1996)
20. F.M. Bayoumi, W.A. Ghanem, Effect of nitrogen on the corrosion behavior of austenitic stainless steel in chloride soluions. Mater. Lett. **59**, 3311–3314 (2005)
21. K. Endo, Y. Abiko, M. Suzuki, H. Ohno, T. Kaku, Corrosion resistance and biocompatibility of high nitrogen-bearing stainless steels. Zairyo-toKankyo **47**, 570–576 (1998)
22. G. Lothongkum, P. Wongpaya, S. Morito, T. Furuhara, T. Maki, Effect of nitrogen on corrosion behavior of 28Cr-7Ni and microduplex stainless steels in air-saturated 3.5% NaCl solution. Corros. Sci. **48**, 137–153 (2006)
23. M. Sagara, Y. Katada, T. Kodama, Localized corrosion behavior of high nitrogen-bearing austenitic stainless steels in sea water. ISIJ Int. **43**(5), 714–719 (2003)
24. H. Yashiro, D. Hirayasu, N. Kumagai, Effect of nitrogen alloying on the pitting of type stainless steel. ISIJ Int. **42**(12), 1477–1482 (2002)
25. L. Nosey, S. Farina, M. Avalos, L. Nachez, B.J. Gomez, J. Feugeas, Corrosion behavior of ion nitrided AISI 316L stainless steel. Thin Solid Film **516**, 1044–1050 (2008)
26. A. Nikmah, D. Izak Rudyardjo, J. Ady, A. Taufiq, Studies on density, corrosion rate and hardness characteristics of stainless steel implanted by nitrogen ion. IOP Conf. Ser. Mater. Sci. Eng. **515**, 012018 (2019)
27. D.A. Schino, J.M. Kenny, Effect of the grain size on the corrosion behavior of refined AISI 304 austenitic stainless steel. J. Mater. Sci. Lett. **21**, 1631–1634 (2002)
28. C.T. Kwok, F.T. Cheng, H.C. Man, W.H. Ding, Corrosion characteristic of nanostructured layer on 316L Stainless steel fabricated by cavitation annealing. Mater. Lett. **60**, 2419–2422 (2006)
29. S. Suyitno, R. Dharmastiti, A. Suprihanto, J. Chem. Pharm. Res. **7**(10), 1034–1038 (2015)

Chapter 13
Effect of Variable Loading on Very High Cycle Fretting Fatigue of Chromium-Molybdenum Steel

Kyosuke Nomura, Naoki Tonooka, Yoshinobu Shimamura, Hitoshi Ishii, Tomoyuki Fujii and Keiichiro Tohgo

Abstract In order to investigate the effect of variable loading on fretting fatigue in the very high cycle region for chromium-molybdenum steel, very high cycle fretting fatigue tests under variable loading were conducted by using an ultrasonic torsional fatigue testing machine. The variable amplitude condition was composed of two stress amplitudes which were higher and lower than the fretting fatigue strength at 10^8 cycles under constant loading. The experimental results revealed that an applied stress amplitude in variable loading lower than the fretting fatigue strength at 10^8 cycles under constant loading was detrimental if the amplitude was higher than 80% of the fretting fatigue strength at 10^8 cycles under constant loading.

13.1 Introduction

Fretting is a phenomenon that microscopic relative slips are repeated at a contact part. When cyclic stress is applied to a fretting part, the fatigue strength considerably decreases and the fatigue limit disappears. The phenomenon is called fretting fatigue. Small fatigue cracks of a few tens μm in length were observed at the fretting areas for run-out specimens [1, 2]. The small cracks were thought to be non-propagating cracks under constant loading. An amplitude such that it causes the non-propagating cracks may be detrimental under variable loading, but it is uncertain how the amplitude in variable loading affects the fatigue life. In this study, very high cycle fretting fatigue tests under variable loading were conducted by using ultrasonic torsional fatigue testing machine. The variable loading was composed of two stress amplitudes which were higher and lower than the fretting fatigue strength at 10^8 cycles under constant

K. Nomura · N. Tonooka
Graduate School of Integrated Science and Technology, Shizuoka University, Hamamatsu, Japan

Y. Shimamura (✉) · T. Fujii · K. Tohgo
Department of Mechanical Engineering, Shizuoka University, Hamamatsu, Japan
e-mail: shimamura.yoshinobu@shizuoka.ac.jp

H. Ishii
Shizuoka University, Hamamatsu, Japan

R.-I. Murakami et al. (eds.), *NAC 2019*, Springer Proceedings in Physics 242,
https://doi.org/10.1007/978-981-15-2294-9_13

Table 13.1 Chemical composition of SCM420H (in weight %)

C	Si	Mn	P	S	Cu	Cr	Ni	Mo
0.21	0.21	0.77	0.02	0.02	0.11	1.02	0.06	0.18

loading. The effect was evaluated by using linear damage accumulation rules, which is widely used for predicting fatigue life under variable loading.

13.2 Material, Experimental Procedures and Fatigue Life Prediction

13.2.1 Material

Material used in this study was quenched and tempered SCM420H. Table 13.1 shows the chemical composition. The Vickers hardness of specimen surface was 500 HV.

13.2.2 Ultrasonic Torsional Fretting Fatigue Testing

Authors have developed an ultrasonic torsional fatigue testing machine and investigated fatigue properties of carburized steels without internal fracture [3]. A fatigue crack initiated from the surface of a specimen during a torsional fatigue test because the maximum shear stress was applied to the surface. Thus, torsional loading is more suitable than axial loading for investigating fatigue properties of case hardening materials such as carburized steels. In this study, we used an ultrasonic torsional fatigue testing machine to accelerate fretting fatigue testing because of the future application of the proposed technique to case hardening materials.

A schematic of an ultrasonic torsional fatigue testing machine is presented in Fig. 13.1. Torsional vibration was generated by applying voltage to a piezoelectric oscillator. The resonance frequency was 20 kHz and the torsional displacement amplitude was only a few μm. The generated torsional amplitude of the oscillator was amplified using an amplifying horn. Further amplification of stress was achieved in a specimen. In this study, dumbbell shape specimens were used. The shape and shear stress/torsional angle distributions of a specimen is presented in Fig. 13.2. The stress ratio R was −1. The torsional displacement at the end of a specimen into FEA solution. Intermittent loading and compressed air cooling were simultaneously used to keep the temperature below 100 °C. Fatigue test was stopped when the resonance frequency decreased by 50 Hz, or when the number of cycles exceeded 10^8 cycles for constant loading.

Figure 13.3 shows a fretting fatigue specimen with a clamping fretting pad. Bridge-shaped contactors made of SKH51 were used. The Vickers hardness of the contactor

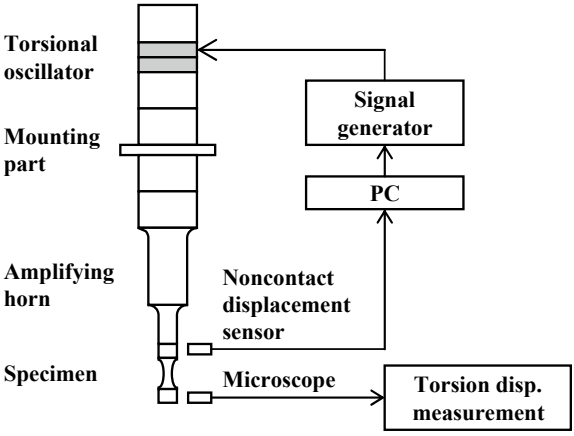

Fig. 13.1 Ultrasonic torsional fatigue testing machine

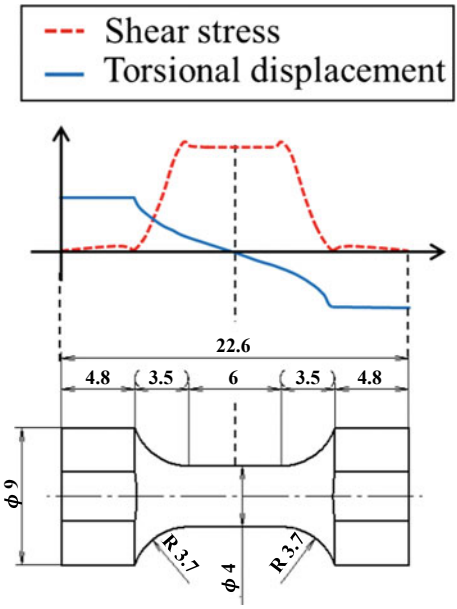

Fig. 13.2 Specimen shape and shear stress/torsional angle distributions

was 730 HV. A contact load can be measured by using a strain gauge attached to one fretting pad. The initial contact load was set to be 800 N in this study. The temperature of the specimen was monitored during fatigue testing by a radiation thermometer, and an increase in temperature was moderate; less than 10 °C. The fretting displacement can be controlled by changing the distance between two contact areas of a contactor. In this study, the fretting displacements ranges 100–200 μm at the fatigue crack initiation positions. The tangential force was not measured because it was difficult to determine the tangential force in this contact situation.

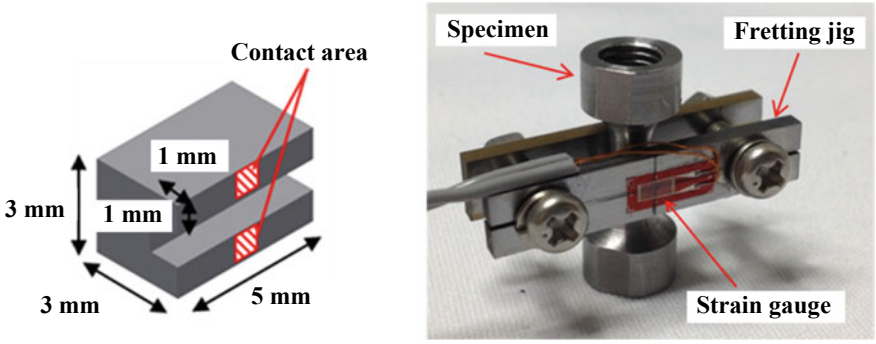

Fig. 13.3 Contactor and a specimen with a clamping fretting pad

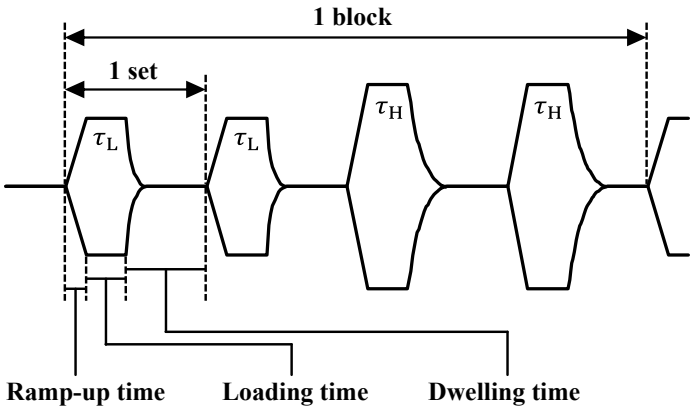

Fig. 13.4 Stress amplitude profile for variable amplitude loading

Figure 13.4 shows an example of a stress amplitude profile for variable loading. A set in the figure is a combination of loading and dwelling in order to prevent excess heating of a specimen. A block in the figure is a combination of two or more amplitudes. Variable loading conditions can be controlled by changing the number of sets in a block for both stress amplitudes.

13.2.3 Linear Damage Accumulation Rule

Miner's rule and modified Miner's rule are methods for predicting a fatigue life under variable loading according to linear damage accumulation. Figure 13.5 shows a conceptual figure of fatigue life prediction for variable loading. If the fatigue life for a stress amplitude τ_i is N_i cycle and the number of cycles applied is n_i, a damage D_i due to τ_i may be evaluated in Eq. 1.

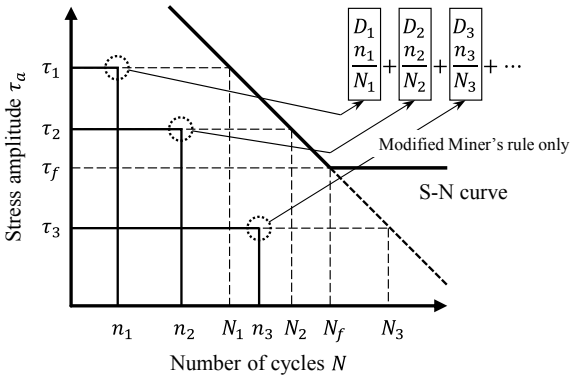

Fig. 13.5 Concept of fatigue life prediction based on linear damage accumulation rule

$$D_i = \frac{n_i}{N_i} \tag{1}$$

In linear damage accumulation rules, the total damage under variable loading is the sum of the damage D_i for every stress amplitude. When the sum of the damage D_i reaches 1, a material is considered to fail.

$$\sum D_i = 1 \tag{2}$$

However, it is well known that stress amplitudes below the fatigue limit may have a detrimental effect to the fatigue life under variable loading. Thus, the finite life curve in a S-N diagram is extrapolated and the fatigue damage due to the stress amplitudes below the fatigue limit was often included in Eq. 2. The improved rule is called modified Miner's rule.

13.3 Results and Discussion

Fretting fatigue tests under constant loading were conducted to obtain the S-N diagram and find the fretting fatigue strength at 10^8 cycles. The S-N diagram is shown in Fig. 13.6. In the figure, circles represent failure, where a specimen have a fatigue crack long enough to decrease the natural frequency by 50 Hz, while a diamond with an arrow indicates run-outs. The fatigue strength at 10^8 cycles was about 220 MPa.

Then, fretting fatigue tests under variable loading were conducted with stress amplitude conditions as listed in Table 13.2. The number of cycles for each stress amplitude n_H and n_L were controlled so as to D_L/D_H equaled to 8, where D_L/D_H is the ratio of the cumulative fatigue damage for lower stress amplitude D_L to higher one D_H.

Figure 13.7 shows linear cumulative damages for every test condition calculated from linear damage accumulation rules. In the calculation, Miner's rule considered

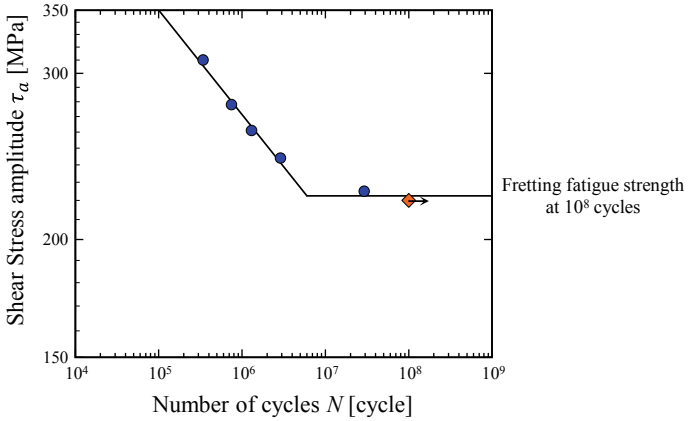

Fig. 13.6 S-N diagram for fretting fatigue under constant loading

Table 13.2 Variable loading test conditions

	No. 1	No. 2	No. 3
τ_H (MPa)	270	270	270
τ_L (MPa)	160	180	200

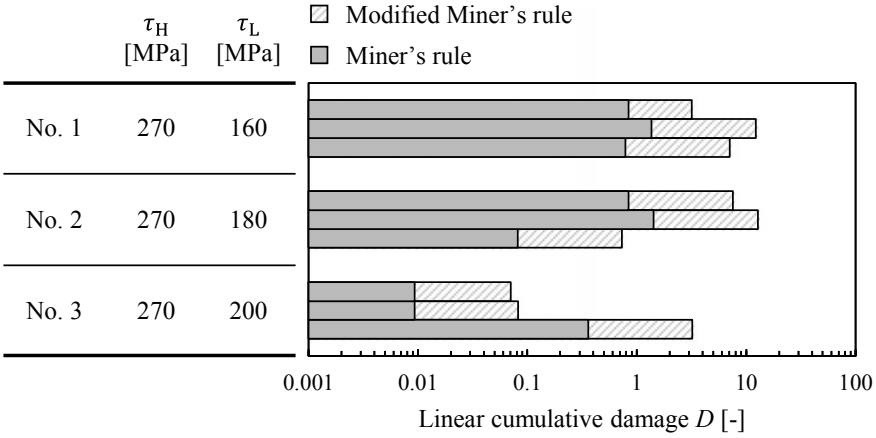

Fig. 13.7 Linear cumulative damage calculated from linear damage accumulation rules

only D_H, but modified Miner's rule considered both D_H and D_L. Prediction close to $D = 1$ is reasonable, but $D < 1$ means nonconservative prediction and $D > 1$ means conservative prediction.

When τ_L is low enough, e.g. No. 1, τ_L did not affect the fatigue life, and Miner's rule resulted in reasonable predictions. On the other hand, when τ_L is close to the

fretting fatigue strength at 10^8 cycles under constant loading, e.g. No. 3, τ_L fairly affected the fatigue life, and modified Miner's rule is a good option for predicting fatigue life under variable loading.

13.4 Conclusions

Very high cycle fretting fatigue tests under variable loading were conducted in order to investigate the effect of stress amplitudes lower than the fretting fatigue strength at 10^8 cycles under constant loading. Test results revealed that stress amplitudes higher than 80% of fretting fatigue strength at 10^8 cycles under constant loading brought fatigue damage, so modified Miner's rule was a good option for predicting fatigue life. On the other hand, if the stress amplitudes are enough low, they do not affect fatigue life, and thus Miner's rule is applicable.

Acknowledgements This research program is financially supported by Chubu Electric Power Co., Inc.

References

1. Y. Kondo, C. Sakae, M. Kubota, K. Yanagihara, Non-propagation crack at giga-cycle fretting fatigue limit. J. Jpn. Soc. Mech. Eng. A **70**, 1066–1071 (2004). https://doi.org/10.1299/kikaia.70.1066
2. J.Q. Xu, S. Shirai, W.M. Tao, Y. Mutoh, Initiation and propagation of fretting fatigue crack in the very long fatigue life. J. Soc. Mat. Sci. Jpn. **51**, 808–813 (2002). https://doi.org/10.2472/jsms.51.808
3. Y. Shimamura, K. Narita, H. Ishii, K. Tohgo, T. Fujii, T. Yagasaki, M. Harada, Fatigue properties of carburized alloy steel in very high cycle regime under torsional loading. Int. J. Fatigue **60**, 57–62 (2014). https://doi.org/10.1016/j.ijfatigue.2013.06.016

Author Index

R.-I. Murakami et al. (eds.), *NAC 2019*, Springer Proceedings in Physics 242,
https://doi.org/10.1007/978-981-15-2294-9

Subject Index

R.-I. Murakami et al. (eds.), *NAC 2019*, Springer Proceedings in Physics 242,
https://doi.org/10.1007/978-981-15-2294-9